PROFILING THE ATMOSPHERE WITH THE AIRBORNE RADIO OCCULTATION TECHNIQUE

A Dissertation

Submitted to the Faculty

of

Purdue University

by

Paytsar Muradyan

In Partial Fulfillment of the

Requirements for the Degree

of

Doctor of Philosophy

August 2012

Purdue University

West Lafayette, Indiana

ACKNOWLEDGMENTS

First and foremost I am immensely thankful to my supervisor Dr. Jennifer Haase for guiding me with her unlimited knowledge and wisdom. You have encouraged and supported me during my studies while allowing and promoting independence. Thank you for being such an understanding and patient supervisor especially with me being a "virtual"/off campus advisee during the past three years. One could not wish for a more inspirational, friendly and caring advisor, and I feel extremely privileged to have had the chance to learn from such a brilliant and meticulous scientist.

I would like to extend my gratitude to my graduate advisory committee members - professors Eric Calais, James Garrison, Harshvardhan, and Feiqin Xie, who have always been ready to answer my questions, and whose suggestions have helped to greatly improve my work.

I am thankful to Feiqin Xie, who, except being a member of the advisory committee, has had a crucial impact on this work with his clarity of vision and depth of understanding, and who has been a Skype call away to answer any questions. I am thankful to James Garrison for his insightful weekly comments and advice during our group meetings, and to his students Ulvi Acikoz, Tyler Lulich, and Brian Ventre: my work heavily relies on the foundations you have laid out.

I am grateful to Schlumberger Foundation for funding my PhD studies through Faculty for the Future fellowship. I especially would like acknowledge Johana Dunlop for her support, kindness and for being such an inspirational person.

I would like to thank my friends both in the US and in France, who have reached out with a helping hand anytime I needed it knowing how much the completion of this project meant to me. I would especially like to thank Liana Mheryan, Karen Hayrapetyan and their two beautiful children for being my family away from home. I will miss the evenings of solving brainteasers Karen would force onto my tired brain

after a long day of work! Thanks to Arshak Petrosyan and Gayane Poghotanyan for completing my feeling of home, and being there for me in any situation. Thank you Valeriia Starovoitova for changing my views on many things, and for being an exemplary character for me as a strong woman. I am grateful to Hovsep Khachatryan and Armine Eghiazaryan who have taken care of my daughter on several occasions while I was away.

I would like to extend my gratitude to my parents for instilling in me deep appreciation towards science and education, my sisters Arevik and Lusine and brother Hayk for believing in me. And finally, I would like to thank my husband and beautiful and smart daughter: you are my purpose and motivation in life...

TABLE OF CONTENTS

LIST OF TABLES

LIST OF FIGURES

Figure Page

Figure Page

Figure Page

ABBREVIATIONS

CHAMP	Challenging Minisatellite Payload
CL	closed-loop
COSMIC	Constellation Observing System for Meteorology
DIAL	Differential Absorption Lidar
DLL	delay lock loop
ECMFW	European Centre for Medium-Range Weather Forecasts
FLL	frequency lock loop
GISMOS	GNSS Instrument System for Multistatic and Occultation Sensing
GNSS	Global Navigation Satellite System
GPS	Global Positioning System
GRS	GPS Recording System
HEFT	HIAPER Experimental Flight Test
HIAPER	High-performance Instrumented Airborne Platform for Environmental Research
IGS	International GNSS Service
INS	Inertial Navigation System
IR	Infrared
LEO	Low Earth Orbit
MCC	master control computer
NSF	National Science Foundation
NWP	Numerical Weather Prediction
OL	open-loop
PLL	phase lock loop
PRN	pseudorandom noise
PSR	Purdue Software Receiver

RO	radio occultation
SAC-C	Satellite de Aplicaciones Cientificas-C
SNR	signal-to-noise ratio
SV	space vehicle
YOTC	Year of Tropical Convection

ABSTRACT

Muradyan, Paytsar. Ph.D., Purdue University, August 2012. Profiling the Atmosphere with the Airborne Radio Occultation Technique . Major Professor: Jennifer Haase.

The GNSS Instrument System for Multistatic and Occultation Sensing (GISMOS) was designed for dense sampling of meteorological targets using the airborne radio occultation (RO) technique. Airborne RO refers to an atmospheric limb sounding technique in which Global Positioning System (GPS) signals are recorded at a receiver onboard an aircraft as the satellites descend beyond the limb of the Earth. The GPS signals, that are unaffected by clouds and precipitation, experience refractive bending as well as a delay in the travel time through the atmosphere. Bending can be used to retrieve information about atmospheric refractivity, which depends on atmospheric moisture and temperature. The new system has the potential for improving numerical weather prediction (NWP) forecasts through assimilation of many high-resolution atmospheric profiles in an area of interest, compared to spaceborne RO, which samples sparsely around the globe.

In February 2008, GISMOS was deployed on the National Science Foundation Gulfstream-V aircraft to make atmospheric observations in the Gulf of Mexico coastal region with an objective to test the performance of the profiling system. Recordings from this flight campaign made with the conventional phase lock loop GPS receivers descend from flight level to 5 km altitude. However, below that level strong refractivity gradients, especially those associated with the boundary layer, cause rapid phase accelerations resulting in loss of lock in the receiver. To extend the RO profiles deeper in the atmosphere, the GISMOS system was also equipped with a GPS Recording System (GRS) that records the raw RF signals. Post-processing this dataset in open-loop (OL) tracking mode enables reliable atmospheric profiling at lower altitudes.

We present a comprehensive analysis of the performance of the airborne system OL tracking algorithm during a 5 hour flight on 15 February 2008. Excess phase and amplitude profiles for 5 setting and 5 rising occultations were successfully retrieved out of the 19 possible cases. Profiles from rising occultations were retrieved with comparable quality to setting occultations. The only missed occultations were due to missing or poor quality ancillary navigation data from the global tracking network and the aircraft turns. We demonstrate that the OL tracking receiver performs much better than the conventional receivers, consistently tracking as low as 0.5 to 3.4 km. Based on this success rate and the improved global network coverage since 2008 providing navigation data bits, the airborne RO system on a straight flight path today would achieve 3 occultations per hour of flight time.

The refractivity profiles retrieved with a geometric optics method show a bias with respect to the European Center for Medium Range Weather Forecasting (ECMWF) analysis profiles. The data were compared with a co-located spaceborne RO profile, and although the airborne data shows a larger bias with respect to ECMWF profiles, there is a correlation of the vertical variations observed with both datasets. The standard deviation of the difference with the ECMWF profile refractivity is less than 1 % in terms of refractivity, which corresponds to 2 K temperature variation. The comparison of the retrieved refractivity and a co-located radiosonde station profile shows a bias as well, with a standard deviation of 2.3 % from 5-12 km altitude. Future efforts should be directed at resolving the source of the bias, in which case the data will be quite useful for assimilation. The differences are within the range of the observation errors typically assigned to RO data below 10 km during assimilation.

Signal tracking and retrieval in the lower troposphere continues to be a major challenge for spaceborne RO, and has limited the impact of all RO data in NWP in the lower troposphere. Full bandwidth signals from airborne measurements could provide a testbed for improving the quality of future spaceborne RO measurements. The airborne RO technique could potentially be implemented on commercial aircraft to provide dense measurements to improve weather forecasting in busy flight corridors.

1. INTRODUCTION

High-impact weather as defined by its influence on society, the economy and the environment, has a significant effect on everyday life. Extreme weather events cause numerous deaths and injuries each year and have high recovery costs [Ebi and Schmier, 2000; Greenough et al., 2001]. Although characterized as low probability, the occurrence of extreme weather events, such as tropical cyclones and severe thunderstorms, has the potential to be catastrophic [Ebi and Schmier, 2000]. As a consequence of global climate change, there is considerable uncertainty as to whether the frequency of high impact weather events is likely to increase over the coming decades [Easterling et al., 2000], therefore, it is imperative to have improved weather forecasting and early warning system to minimize the damage to vulnerable regions. However, data scarcity in remote regions and over the oceans poses a challenge since it affects the uncertainties in the global weather prediction models: the lack of observations near storms and in the surrounding environment sometimes results in poor analysis with ill-defined location and intensity of storm centers in Numerical Weather Prediction (NWP) [Osuri et al., 2010].

Research has been carried out to tackle the challenge of improved forecasting of high-impact weather in NWP. The Observing System Research and Predictability Experiment (THORPEX), which is a ten-year international research and development program, has been designed to promote this through collaboration among academic institutions, operational forecast centers, and users of forecast products [Rabier et al., 2008]. THORPEX observing-system research addresses the influences on the evolution and predictability of weather systems by targeting and assimilating observations into NWP models. In addition, it explores effectiveness of the existing global observing system and the potential for new observing technologies [Shapiro and Thorpe, 2004].

The North Pacific Experiment (NORPEX) directly addresses the lack of observations over the North Pacific basin [Langland et al., 1999]. The data sparsity in this region is a major factor in forecast failures for Pacific winter season storms affecting North America. The NORPEX dataset is being used to study the optimal combination of in situ and space-based observations, and to understand the rapidly growing errors that prevent accurate forecasts of Pacific winter storms. The in situ and spaceborne observations are provided through numerous instruments and observational systems, some of which are described below. New initiatives to evaluate the relative contribution of different components of the global observing systems have shown that radio occultation (RO) is quickly becoming important in reducing forecast errors [Cardinali and Prates, 2011; Gelaro, 2009]. Therefore we expect that airborne RO could make a similar contribution to NWP forecast improvements, with the additional value of denser measurements of targeted systems.

Radiosondes are currently the most reliable source of upper-air in situ measurements. These are balloon-borne meteorological instruments that are launched from over 1,000 worldwide sites usually once every 12 hours, providing high vertical resolution (approximately 10 m (Meteorological Resource Center)) measurements of atmospheric pressure, temperature, humidity, and winds. The radiosonde measurements have proved to be a valuable constituent of long-term global upper-air datasets in studies of large-scale climate variability and change [Seidel et al., 2004]. However, they not only require considerable cost and human resources to launch, but the spatial and temporal radiosonde coverage is limited and concentrated only over land areas. Therefore, radiosondes are insufficient in providing high-resolution information on the horizontal and temporal distribution of water vapor.

Other ground based atmospheric profile measurements of water vapor include water vapor radiometers and optical probing of the atmosphere. The water vapor radiometer is a ground-based remote sensing tool, which can estimate the humidity profile by detecting the radiation intensity at several frequencies. However, the measurement error in this case is affected by precipitation. Optical probing of the at-

mosphere can be accomplished either by differential absorption lidar (DIAL) or using Raman lidar techniques with high vertical resolution (less than 1 km) [Turner et al., 2000]. The principle of DIAL is based on the fact that the absorption characteristics of the water vapor are highly dependent on the wavelength of laser light. The intensities of scattered light on two different frequencies, with and without significant absorption, are measured and compared. Raman lidar uses the scattering of laser light by molecules in the atmosphere to estimate the water vapor profile. However, observations with both these techniques are expensive, and they are limited to clear sky conditions. The distribution of operational ground based profiling systems such as radiometers is quite sparse, which limits their use for detailed studies of large-scale, and to some extent even small-scale weather phenomenon [Ware et al., 1996]. As a result they do not contribute significantly to operational NWP forecasting.

Significant advances have been made in remote sensing of the atmosphere from space with infrared and microwave radiometry enabling global atmospheric observations of temperature and humidity profiles. This includes observations from, for example, the Atmospheric Infrared Sounder (AIRS) and the Advanced Microwave Sounding Unit (AMSU) that were launched together on NASAs Earth Observing System (EOS) Aqua satellite in 1992 [Aumann et al., 2003]. The Infrared Atmospheric Sounding Interferometer (IASI) [Simeoni and Singer, 1999] was launched on the MetOp-A satellite in 2006 as part of an operational meteorological payload. The assimilation studies of the IASI, AMSU, and AIRS radiance and profile observations have been demonstrated to have a significant positive impact at all forecast lengths ([Baker et al., 2005; Hilton et al., 2009; McNally et al., 2006] respectively). Currently, more than 90 % of observational data used in global NWP is provided by these satellites (www.eumetsat.int) contributing to the short and medium range forecasts as well as assessing weather development at synoptic and sub-synoptic scale.

The Global Positioning System (GPS) RO technique is another valuable tool for remote sensing of the atmosphere. Although the largest contribution to decreasing the forecast error in assimilation experiments is provided by AMSU, IASI, AIRS and

radiosonde observations, it is followed by GPS RO [Cardinali and Prates, 2011]. The system has been shown [Gelaro, 2011; Rabier et al., 2008] to have a comparable impact in forecast error reduction per observation to the dense swaths of lower vertical resolution profiles provided by the AMSU, AIRS, and IASI sounders. GPS RO is an active microwave limb sounding technique [Kursinski et al., 1996; Ware et al., 1996], which has the ability to provide high vertical resolution atmospheric soundings with global coverage and all-weather sounding capability. This makes the RO measurements a great contribution to global weather analysis and prediction, and to climate studies in general. This technique uses signals transmitted by occulting GPS satellites that are delayed and bent by gradients in the atmospheric refractivity field, and recorded at a moving receiver [Hajj et al., 2002]. The accumulated bending of the ray path is extracted from the phase delay of the GPS signal as it travels inside the atmosphere. From the bending angle, a refractivity profile can be retrieved, which, in the neutral atmosphere, can be used to determine profiles of temperature and moisture.

The number of RO satellites has significantly increased since the original proof-of-concept GPS/MET mission in 1992. The current constellation of LEO satellites includes the six-satellite Constellation Observing System for Meteorology Ionosphere and Climate (COSMIC) [Anthes et al., 2000; Schreiner et al., 2007], SAC-C [Hajj et al., 2004], the RO instrument GRAS on board Metop-A [GRAS-SAG, 1998], Gravity Recovery And Climate Experiment (GRACE) [Wickert et al., 2005], and the TerraSAR-X satellite mission [Werninghaus et al., 2004]. The Communications/Navigation Outage Forecasting System (C/NOFS) [de La Beaujardiere et al., 2004] also provides RO profiles from its Occultation Receiver for Ionospheric Sensing and Specification (CORISS) instrument. The Radio Occultation Sounder of the Atmosphere (ROSA) is operational on board the OCEANSAT-2 satellite [Perona et al., 2007].

Many authors and operational weather centers have studied the impact of the RO measurements provided by these missions. Healy and Thepaut [2006] demon-

strated that CHAMP GPS RO measurements provide very reliable information on the temperature in the upper troposphere and the lower stratosphere. Assimilation experiments at the UK Met office show reduction of model temperature biases over Antarctica, as well as significant improvements in the root mean square forecast fit to radiosonde temperatures between 300 and 50 hPa in the Southern Hemisphere. Assimilating GPS RO profiles from the COSMIC mission through the Global Data Assimilation System [Kleist et al., 2009] at the National Center for Environmental Prediction (NCEP) demonstrates a significant increase in the model skill providing additional information on the thermodynamic state of the atmosphere [Cucurull, 2010]. Forecast impact experiments with the spaceborne RO refractivity and bending angle measurements show that RO data provides a large positive impact with the greatest improvements in the Southern Hemisphere extratropics [Rennie, 2010]. It was found that bending angle assimilation in general provides a greater positive impact on forecast accuracy compared to refractivity. Simulation studies have also demonstrated higher resolution and accuracy temperature information near the tropopause and more accurate temperature information in the lower stratosphere from the GPS RO measurements compared to that derived from advanced infrared sounder measurements [Collard and Healy, 2003].

Concerning the impact on NWP forecasting of individual tropical storms, an impact study of hurricane genesis using RO refractivity observations suggest that the root mean square errors of water vapor and wind forecasts are reduced compared to observations from dropsondes and radiosondes [Liu et al., 2012]. Assimilating RO data into higher resolution regional or nested NWP models in this case led to stronger initial conditions of the storm and, therefore, to improved forecast of the storms intensification. However, the results of this and other case studies to date are inconclusive as there are usually only limited observations within the area of interest. For this particular study, there were only approximately 30 daily RO soundings available during the study period, which were spread throughout the very large spatial domain.

As Poli et al. [2008] have demonstrated, the NWP forecast impact of GPS RO data depends on the number of GPS RO profiles being assimilated, and has been shown to continuously increase as the number of profiles increases. Although a number of RO missions are being planned for the future (METOP-B, EQUARS, PAZ, SAC-D, CICERO, COSMIC-2), the current total number of spaceborne occultations has decreased to about 2000 per day compared to that of 3000 per day in 2009. This is due to the fact that, for example, the COSMIC currently has only four fully functional satellites as their batteries experience aging problems. In addition, CHAMP and SAC-C are no longer operational. In spite of the advances in spaceborne RO since GPS/MET mission, the spatial sampling of the spaceborne RO remains at a level of approximately 1 daily occultation per $250,000\ km^2$ at mid-latitudes and even fewer in the tropics. Therefore, it is difficult to sample a region of interest through a series of sequential spaceborne RO profiles, which limits this technique's ability to impact the studies of individual storm systems. Also, the large uncertainty in the lower tropospheric spaceborne RO measurements due to reduction of the signal to noise level (in terms of amplitude) reduces the accuracy of the RO measurements in these regions [Sokolovskiy et al., 2010]. Moreover, the impact of spaceborne RO retrievals in NWP at lower altitudes is limited in that $3D$ atmospheric structure is not handled well.

A radio occultation system with a GPS receiver on board an airplane can potentially address these problems currently limiting the spaceborne RO capabilities through targeted observations. It has been demonstrated by Szunyogh et al. [2001], that targeted observations in sensitive regions of the numerical forecasts that were assimilated in the 2000 Winter Storm Reconnaissance (WSR00) program improved the overall quality of the forecasts in 62.5 % cases. Zuffada et al. [1999] first proposed the idea of using atmospheric soundings from an aircraft and analyzed recordings from a mountaintop receiver as a first step in that direction, as the geometry also allows recordings of signals at elevation angles beneath the horizon. Lesne et al. [2002] performed a sensitivity analysis of simulated realistic airborne occultation observa-

tions. Healy et al. [2002] modified the Abel inversion from spaceborne RO method adjusting it to airborne geometry using a partial bending angle, which is the difference between the negative and positive elevation bending angles. An airborne RO experiment using a receiver on board an airplane was attempted by Yoshihara et al. [2004] but a comparison with other data sets was not published. Xie et al. [2008] published the first simulations and retrievals for airborne RO that demonstrated the end to end process and expected accuracy. Muradyan et al. [2010] used actual airborne RO recordings to study the impact of different types of navigation system noise on the airborne RO retrieval accuracy. This thesis publishes the first quantitative analysis of the quality and characteristics of actual airborne RO measurements from a comprehensive dataset.

A schematic representation of the airborne RO geometry is given in Figure 1.1, where $\vec{V}_T$ and $\vec{V}_R$ are the transmitter and the receiver velocity vectors, $\vec{r}_T$ and $\vec{r}_R$ are the position vectors of the transmitter and the receiver respectively calculated from the Earth's center (assuming spherical symmetry), $\hat{e}_T$ and $\hat{e}_R$ are the unit vectors tangential to the ray path at the transmitter and the receiver, and α is the bending angle due to travel through the refractive atmosphere.

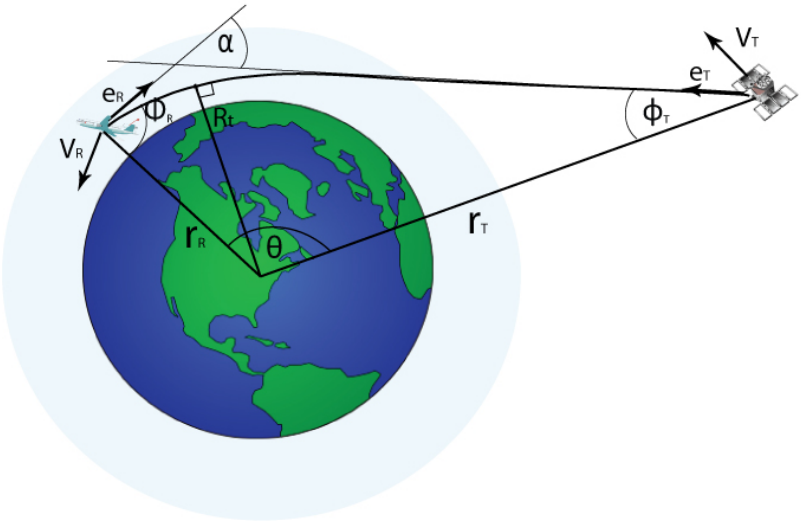

Figure 1.1.: The occultation geometry for a GPS satellite and an airborne receiver.

The airborne RO technique, having a relatively slow-moving receiver inside the atmosphere, provides measurements of atmospheric parameters extending from the aircraft height to the surface that are sequential in time and concentrated in a region of interest [Lesne et al., 2000]. These targeted observations can contribute to studies of individual storm systems and their development. The airborne RO can also serve as a valuable source of lower tropospheric measurements with which current $3D$ retrieval and receiver tracking problems can be investigated that are also relevant to spaceborne RO. As such, the airborne RO measurements can be a valuable addition to existing data sets used in NWP models impacting studies of regional weather.

1.1 The radio occultation technique

The RO technique is based on measuring how the transmitted signals are refracted while passing through the atmosphere. In geometric optics, the propagation path of the electromagnetic waves can be assumed to be dimensionless rays connecting the transmitter and the receiver. When traveling through a spherically symmetric atmosphere the ray paths are described by Bouger's law [Born and Wolf, 1964].

The Doppler shift of a signal traveling through the atmosphere is different from that in a vacuum, which is illustrated in Figure 1.2. In a vacuum, to calculate the Doppler shift, the velocities are projected onto the straight line connecting the source and receiver, resulting in the projected velocity V_S for the transmitter velocity $\vec{V}_T$. However, in the presence of the atmosphere, the signal is Doppler shifted due to the propagation in a varying atmospheric refractivity field. This additional Doppler shift in the transmitted signal is due to the difference between the velocity V_A projected along the ray path through the real atmosphere and the straight line projected velocity V_S. The bending angle α illustrated in Figure 1.3 is a function of the atmospheric refractive index, and it can be derived from the excess Doppler shift in the transmitted signal [Vorobev and Krasilnikova, 1994].

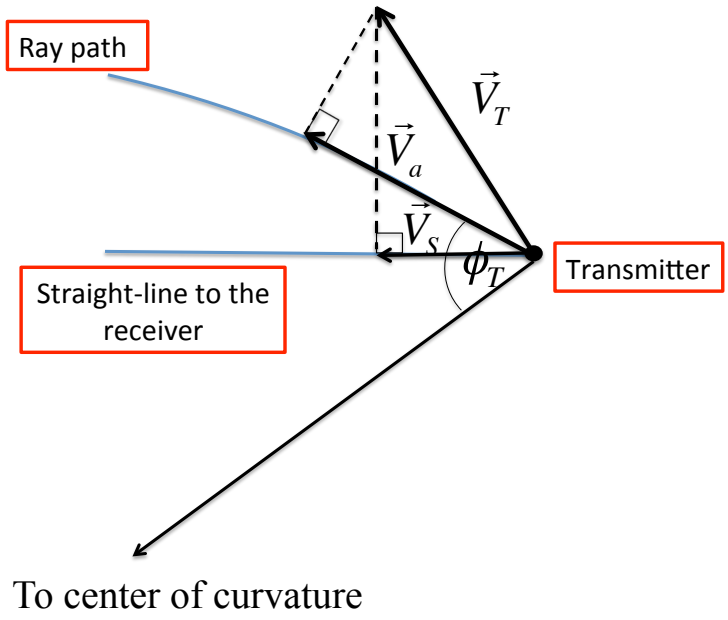

Figure 1.2.: The excess Doppler shift in the transmitted signal is due to the fact that for a signal passing through the atmosphere, the velocities are projected onto a ray path different than the straight line for the vacuum case.

To calculate the bending angle from the Doppler shift, we consider the geometry and the notation in Figure 1.3, where $\vec{V_T}$ and $\vec{V_R}$ are the transmitter and the receiver velocities relative to a reference system in which the atmosphere is stationary. The relationship of receiver frequency f_R and the transmitter frequency f_T is determined through the following equation [Vorobev and Krasilnikova, 1994]:

$$f_R = f_T \frac{c - V_R n_R cos(\phi_R - \beta_R)}{c - V_T n_T cos(\phi_T - \beta_T)} \sqrt{\frac{1 - (\frac{V_T n_T}{c})^2}{1 - (\frac{V_R n_R}{c})^2}} \tag{1.1}$$

where c is the speed of light in a vacuum, n_R and n_T are the refractive indices of the atmosphere at the receiver and the transmitter, and $(\phi_R - \beta_R)$ and $(\phi_T - \beta_T)$ are the angles between the ray paths and $\vec{V_R}$ and $\vec{V_T}$ velocities respectively.

Let f_v be the frequency in a vacuum, and in the absence of refraction, the ray path will be a straight line, thus $\phi_T = \Phi_T$, $\phi_R = \Phi_R$, and $n_T = n_R = 1$, therefore:

$$f_v = f_T \frac{c - V_R cos(\Phi_R - \beta_R)}{c - V_T cos(\Phi_T - \beta_T)} \sqrt{\frac{1 - (\frac{V_T}{c})^2}{1 - (\frac{V_R}{c})^2}} \tag{1.2}$$

The frequency shift, which is the difference of f_R and the frequency in a vacuum ($\Delta f = f_R - f_v$) can be calculated by expanding it into series of $\frac{V}{c}$ taking into account the fact that these ratios are small. Using this and also the fact that $\phi_T = \Phi_T - \gamma_T$ and $\phi_R = \Phi_R - \gamma_R$, we can arrive at the following expression for the excess Doppler:

$$\begin{aligned} D = c\frac{\Delta f}{f_R} = & \\ &= V_T \Big[n_T sin(\Phi_T - \beta_T) sin\gamma_T + (n_T cos\gamma_T - 1) cos(\Phi_T - \beta_a) \Big] - \\ &- V_R \Big[cos(\Phi_R - \beta_R)(n_R cos\gamma_R - 1) + n_R sin(\Phi_R - \beta_R) sin\gamma_R \Big] \end{aligned} \tag{1.3}$$

A ray passing through the atmosphere is refracted by the vertical gradients in the refractive index, which for a spherically symmetric atmosphere is expressed as Bouger's law [Born and Wolf, 1964] :

$$nrsin\phi = \text{const} = n_t r_t = a \tag{1.4}$$

Here a is called the impact parameter, n is the refractive index at a distance r, n_t is the refractive index at the tangent point r_t which is the perigee point of the ray path, and ϕ is the angle between the ray path vector and the radial direction at that point. From Bouger's law, the geometry in Figure 1.3 and the assumption that $n_T = 1$ at the satellite altitude, the relationship between the refractive angles γ_T and γ_R is:

$$R_T sin(\Phi_T - \gamma_T) = n_R R_R sin(\Phi_R + \gamma_R) \tag{1.5}$$

where R_R and R_T are the distances of the receiver and the transmitter from the center of the Earth in this spherical geometry. Thus, considering equations 1.3 and 1.5 as a system of equations for γ_T and γ_R, we can determine the bending angle:

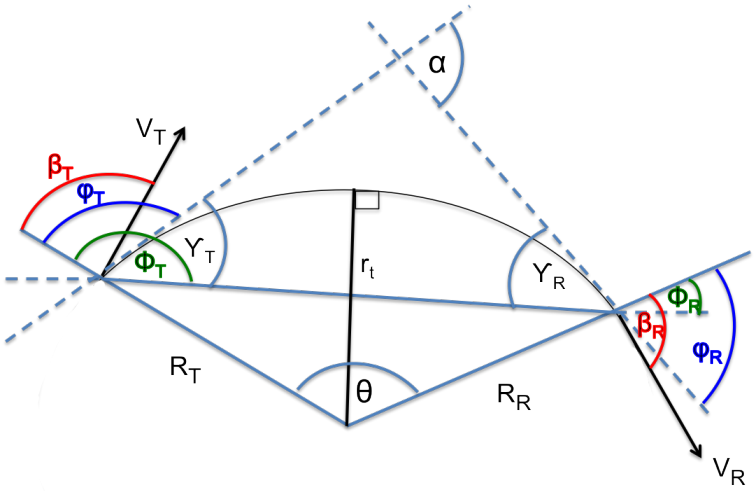

Figure 1.3.: The occultation geometry for a GPS satellite and an airborne receiver defining variables for the derivation of bending angle.

$$\alpha = \gamma_T + \gamma_R \tag{1.6}$$

For spaceborne RO, the bending angle as a function of impact parameter is represented by the following integral [Fjeldbo et al., 1971]:

$$\alpha(a) = -2a \cdot \int_{n_t r_t}^{\infty} \frac{1}{n}\frac{dn}{dr}\frac{dr}{\sqrt{(nr)^2 - a^2}} \tag{1.7}$$

The refractive index in the ionosphere is also a function of electron density. A method for eliminating the ionospheric contribution has been proposed by Vorobev and Krasilnikova [1994] especially for occultation geometry. In spaceborne RO this is done by using the linear combination of bending angles at a common impact parameter a:

$$\alpha_C(a) = \frac{f_{L1}^2 \alpha_1(a) - f_{L2}^2 \alpha_2(a)}{f_{L1}^2 - f_{L2}^2} \tag{1.8}$$

where $f_L1 = 1575.42\ MHz$ and $f_L2 = 1227.6\ MHz$.

From the bending angle measurements, the atmospheric refractive index profile can be retrieved by an integral transformation referred to as the Abel inversion:

$$n(a) = exp\left[\frac{1}{\pi}\int_{x=a}^{\infty} \frac{\alpha(x)dx}{\sqrt{x^2 - a^2}}\right] \tag{1.9}$$

In the neutral atmosphere, refractivity defined as $N = (n-1)\cdot 10^6$ is related to atmospheric temperature T (in K) and the partial pressures of dry air P_d and water vapor P_w (in hPa) through the following equation:

$$N = k_1 \frac{P_d}{T} Z_d^{-1} + k_2 \frac{P_w}{T} Z_w^{-1} + k_3 \frac{P_w}{T^2} Z_w^{-1} \tag{1.10}$$

where the constants $k_1 = 77.6\ K/\text{hPa}$, $k_2 = 70.4\ K/\text{hPa}$ and $k_3 = 3.739\cdot 10^5\ K^2/\text{hPa}$ have been evaluated experimentally [Bevis et al., 1994], and Z_d^{-1} and Z_w^{-1} are the compressibility factors that take into account small departures from behavior of an ideal gas. We use a simplified expression for the refractivity ignoring the non ideal behavior of the air:

$$N = k_1 \frac{P_d}{T} + k_2 \frac{P_w}{T} + k_3 \frac{P_w}{T^2} \tag{1.11}$$

The refractivity profile derived for the neutral atmosphere contains information about both temperature and humidity. Using an *a priori* temperature profile, water vapor can be derived from refractivity [Kursinski and Hajj, 2001], or the temperature profile in the upper parts of the atmosphere can be derived neglecting the effect of moisture in these dry regions. Otherwise, the humidity and temperature profiles can be derived simultaneously using one-dimensional variational analysis using an *a priori* model of the atmosphere with known errors [Poli et al., 2002; Steiner et al., 1999].

1.2 The airborne RO technique

Similar to the spaceborne RO technique, a refractive index profile can be derived from the airborne observations for heights below the flight altitude through a modified Abel transform procedure [Fjeldbo et al., 1971; Healy et al., 2002]. In the case of airborne RO, the bending is not symmetric with respect to the tangent point. Rays reaching the receiver from above the local horizon, referred to as positive elevation angle rays, and those reaching the receiver from below the local horizon, negative elevation angle rays, are both affected by the atmospheric refractivity. However, the positive elevation rays cannot provide unambiguous information on atmospheric refractivity. Similarly, the part of the ray path above the aircraft altitude for a negative elevation angle ray also cannot provide unambiguous information on refractivity, therefore its contribution must be removed. For a spherically symmetric atmosphere, each negative elevation ray with bending angle α_N has a corresponding positive elevation ray with bending angle α_P with the same impact parameter a (Figure 1.4).

These negative and positive elevation bending angles are given by Eq. 1.12 and Eq. 1.13.

$$\alpha_P(a) = -a \int_{n_R r_R}^{n_T r_T} \frac{1}{n}\frac{dn}{dr}\frac{dr}{\sqrt{(nr)^2 - a^2}} \tag{1.12}$$

$$\alpha_N(a) = -2a \int_{n_t r_t}^{n_R r_R} \frac{1}{n}\frac{dn}{dr}\frac{dr}{\sqrt{(nr)^2 - a^2}} - a \int_{n_R r_R}^{n_T r_T} \frac{1}{n}\frac{dn}{dr}\frac{dr}{\sqrt{(nr)^2 - a^2}} \tag{1.13}$$

In these equations r_t is the radius at the tangent altitude, and r_T and r_R are the radii at the transmitter and the receiver respectively. The negative elevation bending angle is twice the integral along the ray path from the tangent point altitude to the receiver, and then the integral from that altitude to the altitude of the GPS satellite, and the positive elevation bending angle is equal to the second term in Equation 1.13. The difference between these two bending angles will result in $\alpha'(a)$ the "partial bending" angle, which is the bending occurring along the section of path below the receiver altitude.

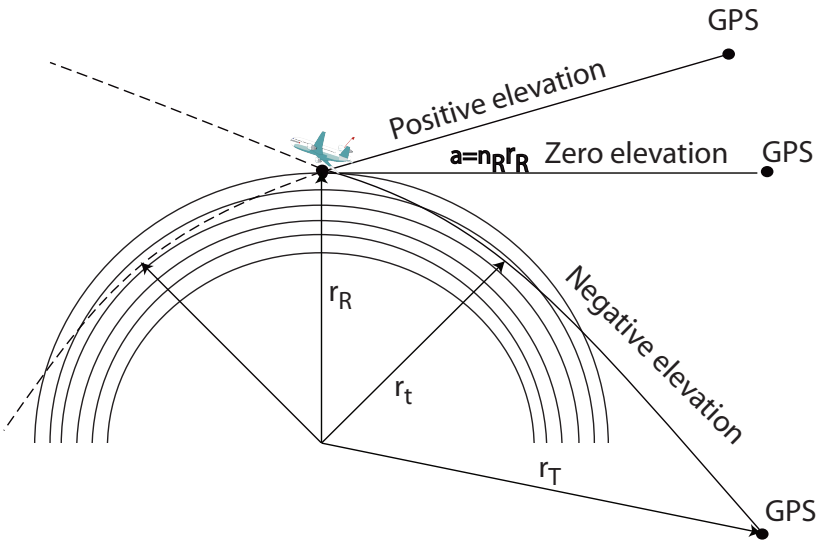

Figure 1.4.: Illustration of positive and negative elevation ray paths relative to the local horizon. The positive elevation ray has been extrapolated to demonstrate that both negative and positive ray paths have the same impact parameter

$$\alpha'(a) = \alpha_N(a) - \alpha_P(a) = -2a \int_{n_t r_t}^{n_R r_R} \frac{1}{n}\frac{dn}{dr}\frac{dr}{\sqrt{(nr)^2 - a^2}} \tag{1.14}$$

Thus, the Abel inversion in the airborne RO case will result in a refractive index profile below the receiver altitude, which depends on n_R, the refractive index value at the location of the receiver:

$$n(a) = n_R \cdot exp\left[\frac{1}{\pi}\int_{x=a}^{n_R r_R} \frac{\alpha'(x)dx}{\sqrt{x^2 - a^2}}\right] \tag{1.15}$$

Current challenges in RO technique for both spaceborne and airborne measurements arise in the lower troposphere, where the signal can experience rapid phase changes and amplitude variations due to the complicated signal propagation through strong gradients. Routine tracking of RO signals in the moist tropospheric regions by means of generic phase-locked loop (PLL) receivers may result in signal

loss [Sokolovskiy, 2001]. If multipath propagation is not taken into account, space-borne RO measurement inversions near the surface have been shown to result in significant errors that include biases [Rocken et al., 1997; Sokolovskiy, 2001]. Alternatively, an open loop tracking technique can be used that does not require smoothly varying phase and amplitude as a function of time. This method is not limited by assumptions about the signal structure, but rather uses an algorithm for tracking the signal using a pre-defined estimate of the Doppler frequency. Therefore, to overcome the difficulties of signal tracking in the lower troposphere, the airborne RO system includes a GPS Recording System (GRS) providing 10 MHz measurements of raw RF signals for post-processing in open-loop (OL) mode as well as geodetic quality PLL receivers.

The post-processing of GRS data is performed in a software receiver [Heckler and Garrison, 2004], for which OL tracking was developed by Ventre [2006], and implemented for rising occultations by Acikoz [2011]. To use OL tracking, first the presence of signals and the rough estimates of Doppler frequency are determined using closed-loop (CL) tracking with a locally generated replica of the incoming signal. The initial estimates of code delay and Doppler are refined, and the OL tracking is then initialized based on the code delay obtained from CL, using a Doppler model to steer the phase and frequency of the replica signal. OL tracking provides an estimate of the difference of actual and model Doppler shift that is robust in the presence of atmospheric multipath.

This thesis shows the first retrieval results from applying the OL tracking method to airborne RO data. Chapter 2 describes the Global Navigation Satellite System (GNSS) Instrument System for Multistatic and Occultation Sensing developed for RO measurements, as well as details of the flight campaign for the data used in this work. In Chapter 3 we describe the CL and OL tracking methods of GPS signals. Chapter 4 provides details about the method we use to effectively evaluate the airborne RO system performance, and presents sensitivity studies of the retrieval. Chapter 5 concentrates on the study of the performance of airborne RO using OL

tracking. Chapter 6 addresses the accuracy of the airborne RO profiles in comparison to independent measurements. Chapter 7 provides an example of the synoptic scale variations that are measured by the new RO system. The conclusions section summarizes the airborne RO retrieval results from this campaign and includes recommendations on improvements to the method, that will be necessary for practical application of the method to a future operational airborne RO system.

2. MEASUREMENT CAMPAIGN AND THE GISMOS SYSTEM

GISMOS is designed to use occulted and reflected GPS signals to retrieve tropospheric water vapor, soil moisture and ocean surface roughness from long duration and high altitude flight measurements [Garrison et al., 2007]. It was developed for the National Science Foundation (NSF) HIAPER aircraft, which is a Gulfstream V (GV) business jet modified for atmospheric research by the University Corporation for Atmospheric Research (UCAR). In February 2008, GISMOS was deployed for a set of research flights in the Gulf of Mexico coastal region as part of the HIAPER Experimental Flight Tests (HEFT08). The main objective of the flight campaign was to test the performance of the GISMOS system in comparison to radiosonde and dropsonde profiles that were also collected during the field campaign.

2.1 The GISMOS measurement campaign

The flights took place between February 8 and February 23, for a total of 46.5 research flight hours. Four of the research flights were dedicated to occultation measurements, for which the flight trajectory was planned so that the occultation tangent point locations were near the radiosonde launch sites close to the launch time. In addition to regular daily radiosonde launches at 00Z and 12Z, 28 extra soundings were acquired from SHV, JAX and TLE radiosonde stations at 18Z and 21Z during the week of February 18-24, 2008. Additionally, three of these RO flights (February 14, 15, and 22) were planned over the open ocean where dropsondes could be released without a concern of causing a safety hazard on the ground. The remaining two research flights were dedicated to overflights of buoys at different distances from the coastline for the ocean reflection measurements, to compare independent observations

of ocean roughness and wind speed retrievals at a range of wind speeds. Figure 2.1 shows the map of the research flight on February 15 along with the predicted occultation times and locations, as well as the locations of released dropsondes. This thesis analyzes data for this specific flight, because the long straight legs in the flight path (dot-dashed black line) allow us to evaluate the performance of the GISMOS system with minimum effect from aircraft turns. It also enables a large scale synoptic comparison with the Numerical Weather Prediction (NWP) model profiles over the continental US where we have confidence in their accuracy.

2.2 The GISMOS instrument system

Because of the challenges of recording low amplitude signals from occulting satellites, special attention was paid to the antenna design. The GISMOS instrument system consists of seven antennas. The zenith antenna is placed on the top of the aircraft fuselage for the direct signal for navigation purposes. Two high-gain, narrow field of view dual frequency antennas with a gain pattern focused toward the horizon are specifically designed for low elevation RO measurements (Figure 2.2). These antennas are mounted inside the windows on both sides of the aircraft. Two low gain, wide field of view avionics antennas are mounted on window blanks in the next pair of side windows as a backup for the high-gain RO antennas. Two antennas are mounted on the underside of the fuselage for reflection measurements, receiving both left-hand and right-hand circularly polarized signals.

In this work we will use signals from high gain antennas that are split and routed to both conventional receivers and the high frequency GPS recording system. We will also consider signals from the top antenna recorded by the GRS that are used as reference recordings to remove receiver clock errors.

The RO technique requires high sample rate carrier phase measurements made on two frequencies. The GISMOS measurement system includes four dual-frequency Trimble NetRS receivers sampling at 5 Hz from the four side-looking antennas. It also

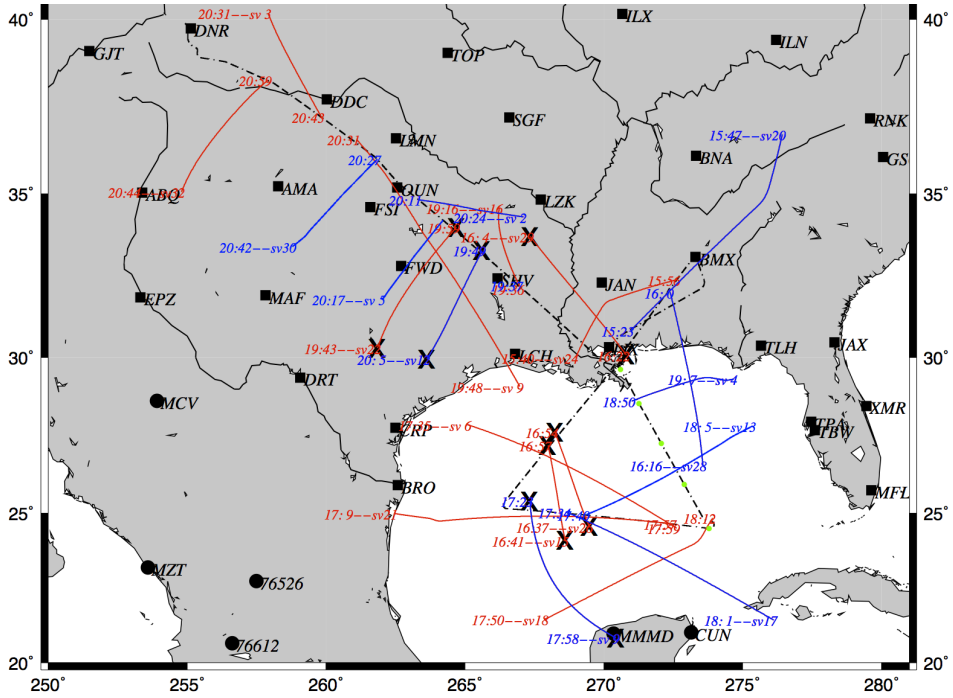

Figure 2.1.: Research flight on 15 February 2008. Black dot-dash line represents the flight trajectory. The blue and red lines show the occultation tangent point locations for setting and rising occultations respectively. The numbers in the beginning and at the end of these lines indicate the start and the end time of each occultation. Squares show US radiosonde locations, and black circles show the radiosonde sites in Mexico. The green circles show the locations of released dropsondes. The crosses denote the ECMWF analysis profile locations.

includes an Applanix GPS POS/AV 510 system with an integrated inertial measurement unit. The POS/AV contains an internal Trimble BD950 dual frequency OEM GPS receiver board sampling at 10 Hz and an Inertial Science AIMU inertial measurement unit sampling at 200 Hz. This system is the key instrument for acquiring accurate airplane velocity measurements with a velocity accuracy of 5 mm/sec, roll and pitch accuracy of 0.005 degrees and heading accuracy of 0.008 degrees.

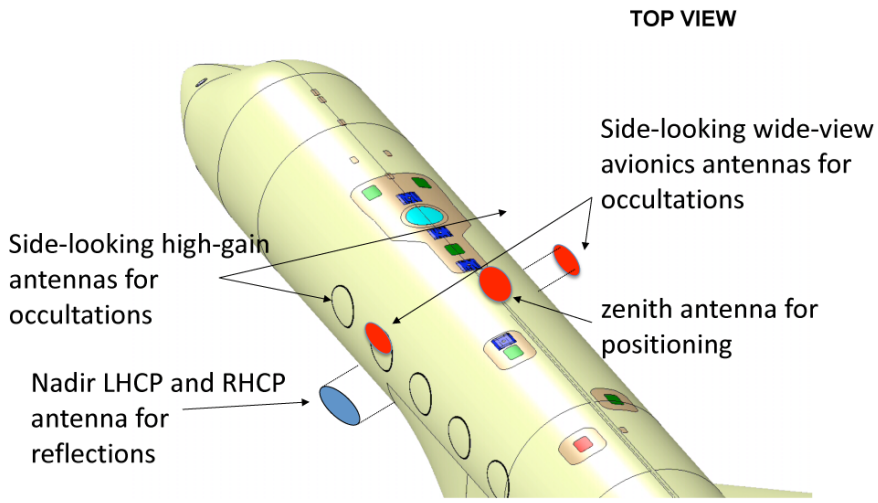

Figure 2.2.: Antenna placement on the airplane.

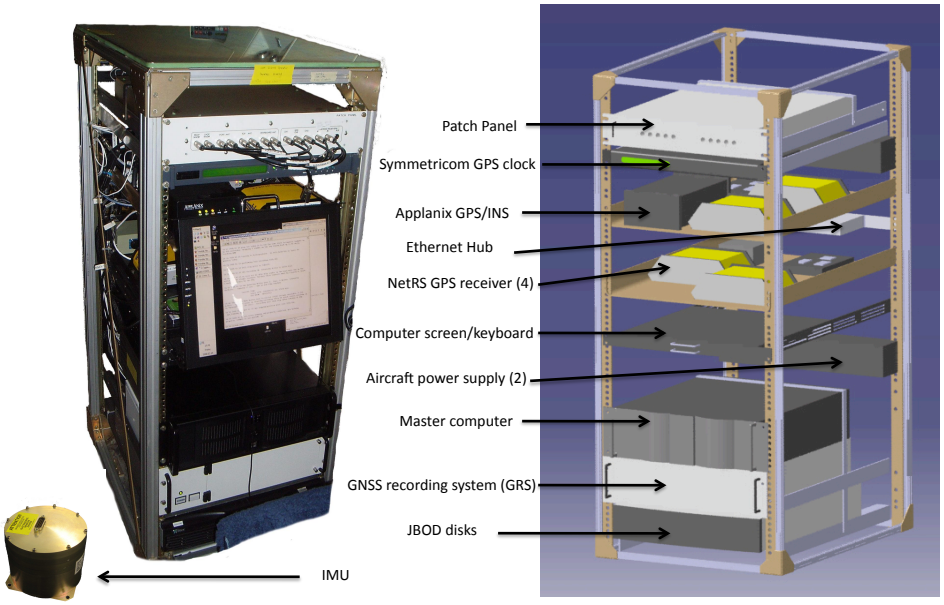

Figure 2.3.: The GISMOS instrumentation rack.

In order to record the RF signal for later use in the OL tracking, the GISMOS measurement system includes a GNSS Recording System (GRS) capable of continuously sampling both L1 (1575.42 MHz) and L2 (1227.40 MHz) frequencies at 10 MHz which can be switched between the side-looking and reflection antennas depending on the experiment mode. It contains a Symmetricom GPS timing receiver providing a common standard timing signal for all the receivers at 10 MHz frequency; a patch panel which distributes the signals from the antennas to their appropriate receivers and to the GRS; and, finally, a master control computer for configuration and monitoring the recording of all receivers, and for providing Ethernet communications to the network onboard HIAPER (Figure 2.3).

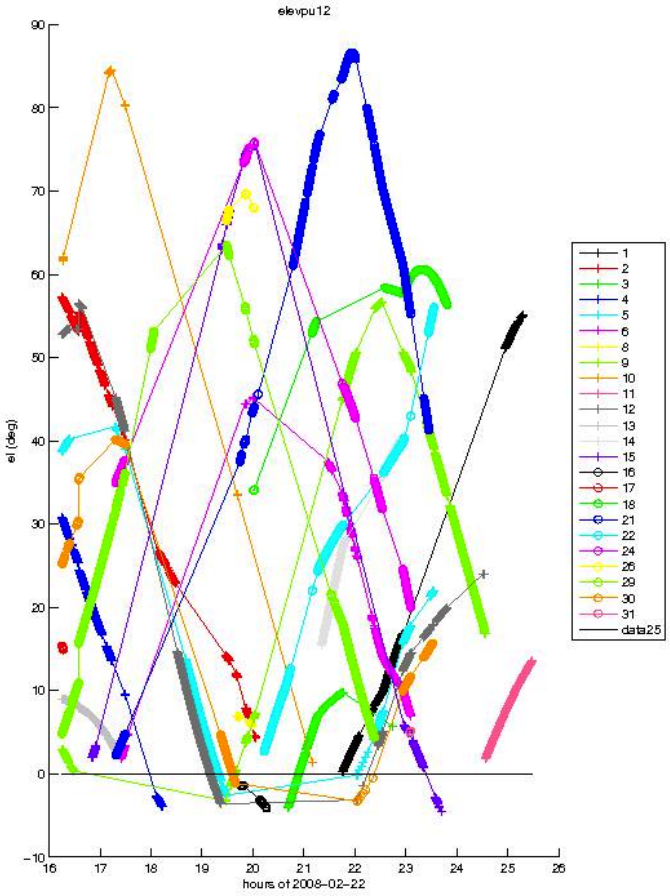

Figure 2.4.: Elevation angle coverage and duration of recording for a NetRS receiver recording through starboard RO antenna on day 2008-02-22.

The receivers in this measurement system are independent, i.e. if the science objective of a mission requires only RO and precise navigation measurements, then only the appropriate receivers for such a mission can be used. Since this work is concerned with the analysis of RO measurements, we will address only the RO component of GISMOS using data from NetRS receivers and the GRS recorder and side looking RO antennas. Due to a programming error, during the February 2008 flight campaign the NetRS receivers were by default configured to record when the satellite elevation was above 0°. Despite that, RO measurements were still recorded below the local horizon for a few satellites, as can be seen in Figure 2.4, which shows satellite elevation angles from NetRS measurements made with the starboard antenna. In this work we consider two airborne RO cases from NetRS data, however, due to the large gaps in the NetRS measurements, for the main part of this work we analyze the raw RF data from the GRS using the side looking RO antennas.

3. CLOSED-LOOP AND OPEN-LOOP TRACKING OF THE GPS SIGNAL

A major challenge for RO technique in the troposphere is obtaining continuous time series of amplitude and phase when sharp refractivity gradients cause premature signal tracking loss [Sokolovskiy, 2001]. GISMOS was designed to include measurements from both closed-loop receivers and a raw GPS signal recorder (GRS) from the same antenna, so that when the signal is lost in the CL receiver, more advanced techniques for signal tracking to deeper atmospheric layers can be used [Heckler and Garrison, 2004; Ventre, 2006]. The following sections present a description of CL and OL tracking methods.

3.1 Received signal

The GPS signals received at the user's antenna consist of the sum of signals from all satellites in view with some noise (which includes contributions from background radio frequency and thermal noise in the hardware, and is modeled as being *white*), and can be expressed as follows [Ventre, 2006]:

$$r(t) = \sum_{k=1}^{K} s_R^{(k)}(t) + n(t) \tag{3.1}$$

where K is the number of satellites in view and $n(t)$ is the noise.

During the transit process to the receiver, the GPS signal experiences some changes: the amplitude of the signal decreases because of attenuation, and the signal is delayed by its time of travel. Also, because of the motion of the transmitter and the receiver, the signal frequency will change, resulting in a Doppler shifted signal. Therefore, the signal received from the k^{th} satellite can be expressed as:

$$s^k(t) = A^{(k)}(t)p^{(k)}(t-\tau^{(k)})D^{(k)}(t-\tau^{(k)})e^{j(2\pi(f_{L1}+f_D^{(k)})t+\Phi^k(t))} + n^k(t) \tag{3.2}$$

where $A^{(k)}$ is the received signal amplitude, $p^{(k)}(t-\tau^{(k)})$ is the delayed PRN code, $\tau^{(k)}$ and $f_D^{(k)}$ are the signal time of travel and the Doppler frequency respectively for the k^{th} satellite, $\Phi^{(k)}$ is the phase delay, $n(t)$ is the additive white noise, and $f_{L1} = 1575.42\,MHz$. The low cross-correlation between the Gold PRN codes allows to separate the signals from individual satellites [Braasch, 1999]. The RO measurement is required for a single satellite, therefore the received signal in Equation 3.2 can be expressed as the signal from only the satellite under consideration with additive noise from the remaining visible satellites.

The high frequency of the received signal is downconverted to near base band: the signal is first multiplied by a sinusoid centered at $f_{L1} - f_{IF}$, where f_{IF} is the intermediate frequency. The resulting complex signal near f_{IF} can be written as:

$$u_{IF}(t) = A(t)p(t-\tau)D(t-\tau)e^{j(2\pi(f_{IF}+f_D)t+\Phi(t))} + n(t) \tag{3.3}$$

This down sampled signal is what is sampled at 10 MHz by the GPS recording system. The further processing steps are carried out in post-processing by the software implementation of a GPS receiver [Heckler and Garrison, 2004].

3.2 Signal acquisition

The first step in signal tracking is the acquisition of available satellites, during which the GPS signal is detected through a search within a region of delays and Doppler frequencies, with an objective to provide an estimated $\hat{f}_D$ Doppler frequency value and code delay $\hat{\tau}$ for each satellite. A search over the entire Doppler and delay space is necessary when there is no available information on the user's position, velocity and time. The received signal is cross-correlated with a locally generated signal for each satellite (reference signal) which, ignoring the noise, can be written as:

$$\overline{u}(t-\overline{\tau}) = p(t-\overline{\tau})e^{j(2\pi f_{IF}+\overline{\phi}(t))} \tag{3.4}$$

where $\overline{\tau}$ is the test delay, $\overline{f}_D = \frac{d\overline{\phi}(t)}{2\pi dt}$ is the test Doppler frequency, and $\overline{\Phi}(t)$ is the test phase of the reference signal. The correlation over T_I in blocks of time t_n is:

$$\overline{S}(t_n) = \frac{1}{T_I}\int_{t_n}^{t_n+T_I} u(t)\ \ \overline{u}^*(t-\overline{\tau})dt \tag{3.5}$$

$$\overline{S}(\Delta\tau, \Delta f_D, \Delta\Phi) = ADe^{j\Delta\Phi}\overline{R}(\Delta\tau, \Delta f_D) \tag{3.6}$$

where $\Delta\Phi = \Phi - \overline{\Phi}$ is the carrier phase offset, and $\overline{R}(\Delta\tau, \Delta f_D)$ is the ambiguity function, which is defined (as expressed in continuous time):

$$\overline{R}(\Delta\tau, \Delta f_D) = \frac{1}{T_I}\int_0^{T_I} p(t-\tau)p(t-\overline{\tau})e^{j2\pi\Delta f_D t}dt \tag{3.7}$$

$\Delta\tau = \tau - \overline{\tau}$ is the delay error, $\Delta f_D = f_D - \overline{f}_D$ is the Doppler error, and D is the navigation data bit in that time interval. The location of the maximum power (or amplitude) of the ambiguity function over the delay-Doppler space is the best initial estimate of the received signal's parameters, and this main peak is only one chip wide. For effective correlation, the maximum allowed code misalignment is half a chip.

The increment in the test Doppler is set by the Doppler bin width $f_{D,bin}$, which is a function of the integration time, $T_I = 1/2f_{D,bin}$. The shortest integration time is one code period ($1\ ms$), therefore $f_{D,bin} = 500\ Hz$. Increasing the integration time makes the Doppler steps smaller, thus decreasing the Doppler uncertainty. Although this will lead to a longer search time due to the larger number of test Dopplers, it will also result in increased SNR with increased integration time.

3.3 Signal tracking

After the signal is acquired, the rough estimates of Doppler and code delay from the acquisition process must be refined. The traditional method for doing this is the

CL tracking method (Figure 3.1), where multiple feedback control loops steer the frequency until the error between the estimates and the actual values is a minimum [Ventre, 2006]. The tracking loops executing this process are known as delay lock loop (DLL), frequency lock loop (FLL), and phase lock loop (PLL). The DLL employed in the receiver refines the code delay $\hat{\tau}$, and the FLL and/or phase-lock PLL updates the frequency estimate f_D as well as the estimate of phase $\hat{\Phi}$. However, during an occultation when the GPS signal travels through the lower part of the atmosphere, random phase accelerations of the signal can be significantly larger than allowed for stable operation of PLL in generic GPS receivers [Sokolovskiy, 2001]. In this case, the PLL, which steers a local oscillator to match the phase of the received signal, is unable to compensate for the high signal dynamics, and the receiver lock is lost. In terms of signal-to-noise ratio (SNR), the adjustment of the frequency of the reference signal on the basis of previous measurements in CL tracking is reliable when there is sufficient signal-to-noise ratio and the signal dynamics are not high [Ao et al., 2009]. In order to acquire an occulted signal in general, the SNR at the receiver must exceed a critical value of ≈ 10 [Kursinski et al., 1996]. If the SNR falls below this value, the above mentioned phase lock and signal loss take place. The schematic representation of the CL tracking is illustrated in Figure 3.1 ([Misra and Enge, 2001]).

3.4 OL tracking

As described in Section 3.3, the CL tracking provides reliable measurements when the SNR is sufficient, and below some critical value in the region of rapid phase accelerations during an occultation, the traditional CL receivers lose lock. When the PLL method is not capable of tracking the signal during the descent of the satellite, the OL tracking method, which does not rely on feedback loops, is used to continue tracking the GPS signal deeper in the atmosphere. OL tracking uses *an a priori* estimate of the Doppler frequency, which is calculated from accurate measurements of positions and velocities of the transmitter and the receiver.

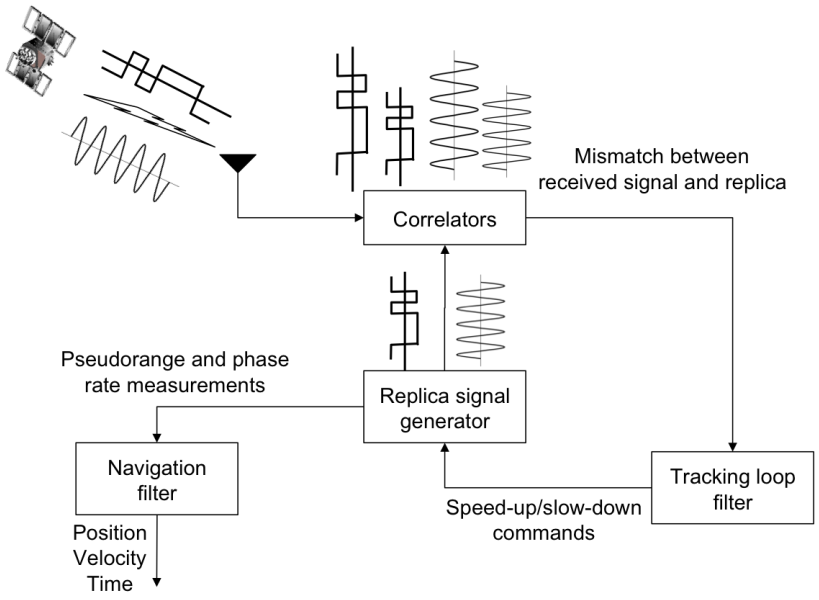

Figure 3.1.: Closed-loop tracking method (Misra and Enge [2001]).

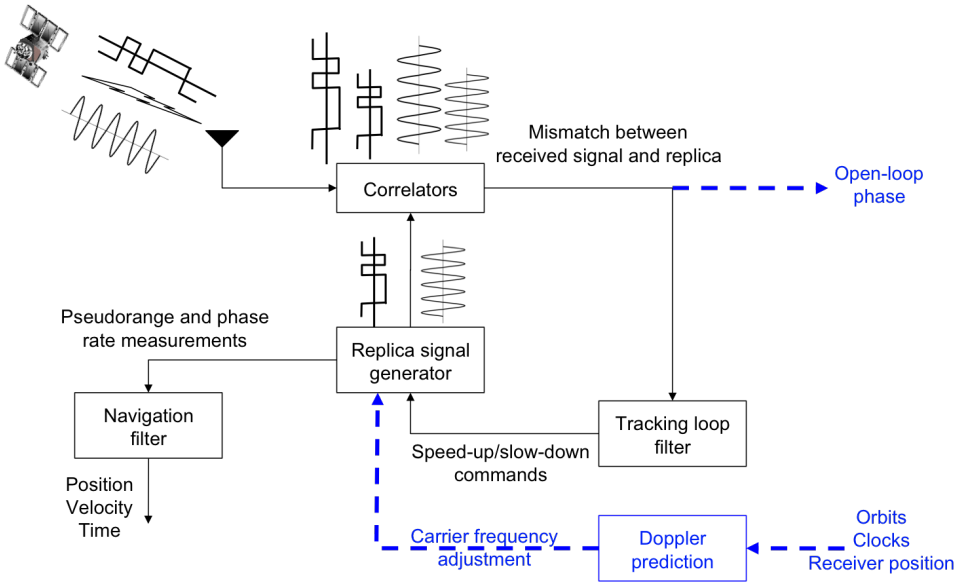

Figure 3.2.: Open-loop tracking method (modified from Misra and Enge [2001]).

The high accuracy navigation solution for the airplane is acquired through post-processing the GISMOS navigation data, and the satellite velocity/position is acquired using the International GNSS Service (IGS) precise obits. As we described in

Chapter 1, the excess Doppler profiles are used to calculate the bending the occulting ray path experiences, which is inverted to obtain refractivity profiles. The excess Doppler is the derivative of the excess phase defined as the difference of measured phase and the straight-line geometric phase between the transmitter and the receiver. Thus, the objective of OL tracking is to extract these excess phase profiles from the GPS signals. The structure of the OL tracking method is depicted in Figure 3.2 (Modified from [Misra and Enge, 2001] by J. Haase).

The OL tracking algorithm is explained in Beyerle et al. [2006], and implemented for airborne RO by Ventre [2006]. Its goal is to extract time varying phase information $\Phi(t)$ from the received and down-converted GPS signal u_{IF}:

$$u_{IF}(t) = A(t)p(t-\tau)D(t-\tau)e^{j(2\pi f_{IF}t+\Phi(t)+\Phi_0)} + n_{IF}(t) \tag{3.8}$$

where $\Phi(t)$ is the time varying phase, and its time derivative will account for the Doppler frequency, Φ_0 is the initial phase at $t = 0$, $A(t)$ is the amplitude at the time of reception, $p(t)$ and $D(t)$ are the ranging code and the navigation data message respectively that are delayed by τ, the time varying path-length delay. f_{IF} is the carrier wave at the intermediate frequency, and the signal is modeled as received in the presence of additive, white Gaussian noise n_{IF}.

First, code wipeoff is performed to remove the code from the received signal. This is done by multiplying the received signal by the replica of the ranging code computed at an initial estimate of the delay obtained from the CL tracking.

$$u_s(t) = u_{IF}\ \ p(t-\hat{\tau}) \tag{3.9}$$

It is assumed that the accuracy of the predicted code delay is sufficient so that the estimated ranging codes align to within a small fraction of a code chip.

$$p(t-\tau)p(t-\hat{\tau}) \approx 1 \tag{3.10}$$

Therefore, the signal following this code wipeoff process will be:

$$u_s(t) \cong A(t)D(t-\tau)e^{j(2\pi f_{IF}t+\Phi(t)+\Phi_0)} + n_s(t) \tag{3.11}$$

where $n_s(t) = p(t - \hat{\tau})\, n_{IF}(t)$, and it has the same statistics as $n_{IF}(t)$ because $p(t)$ is independent and $|p(t)|^2 = 1$. The subsequent evolution of the code delay over the tracking period is updated based on the pre-defined Doppler model, assuming the Doppler model is sufficiently close to the actual Doppler frequency.

After the code wipe-off, the result is multiplied by a complex exponential replica signal $v(t)$.

$$v(t) = e^{-j(2\pi f_{IF} t + \Phi^{model}(t))} \tag{3.12}$$

Here $\Phi^{model}(t)$ is the time varying predicted phase determined from the predicted Doppler from the following relationship:

$$f_D^{model}(t) = \frac{1}{2\pi} \frac{d\Phi^{model}(t)}{dt} \tag{3.13}$$

The model phase at the time t_n is the accumulated Doppler from $n-1$ previous integration times:

$$\Phi_n^{model} = 2\pi T_I \sum_{j=1}^{n-1} f_{D,j}^{model} \tag{3.14}$$

where $\Phi_n^{model} \equiv \Phi^{model}(t_n)$ and $f_{D,j}^{model} \equiv f_D^{model}(t_j)$. The product of u_s and v is integrated over the period of T_I to form the complex correlator sum Ψ_n:

$$\Psi_n = \frac{1}{T_I} \int_{t_n}^{t_n + T_I} u_s(t)\, v(t) dt + N_n \tag{3.15}$$

where the integration time T_I is set to one code period, which varies with time due to the Doppler frequency. If we assume that the frequency and amplitude are piecewise constant and can be approximated as $A_n \equiv A(t_n)$ and $f_{D,n} \equiv f_D(t_n)$, and that the data bit is constant over the period of integration and its transitions are aligned with integration times, the result can be written as:

$$\Psi_n = \frac{A_n D_n}{T_I} \int_{t_n}^{t_n + T_I} e^{j(\Phi(t) - \Phi^{model}(t))} dt + N_n \tag{3.16}$$

$$\Psi_n = A_n D_n sinc(\pi \delta f_{D,n} T_I) e^{\frac{\delta\Phi_n + \delta\Phi_{n+1}}{2}} + N_n \tag{3.17}$$

where $\delta f_{D,n} = f_{D,n} - f_{D,n}^{model}$ and $\delta\Phi_n = \Phi_n - \Phi_n^{model}$ are the differences of true and predicted Doppler and phase respectively [Lulich et al., 2010].

3.5 OL residual phase

The OL tracking result, the complex correlator Ψ_n, consists of real and imaginary components referred to as inphase, i_n, and quadrature, q_n. To increase the SNR and reduce the probability of cycle slips, these components are coherently integrated over a single data bit, also lowering the measurement rate from 1 kHz to 50 Hz.

$$I_k = \sum_{n=20(k-1)+1}^{20k} i_n \tag{3.18}$$

$$Q_k = \sum_{n=20(k-1)+1}^{20k} q_n \tag{3.19}$$

The residual phase Φ^R is then calculated as the angle between the in phase and quadrature correlation sums through the use of four-quadrant arctangent function:

$$\Phi_{k+1}^R = atan2(\frac{Q_k}{D_k}, \frac{I_k}{D_k}) + C_k \tag{3.20}$$

Thus, the calculation of the residual phase requires information on the navigation data bit D_k, which in this work is acquired from the COSMIC data bit archive. C_k in Equation 3.20 is a constant term which is added to eliminate the cycle slips:

$$C_k = \begin{cases} C_{k-1} + 2\pi & \text{if } \Phi_k < -\pi \\ C_{k-1} - 2\pi & \text{if } \Phi_k > +\pi \\ C_{k-1} & \text{else} \end{cases} \tag{3.21}$$

The received total phase Φ^{total} is the sum of the geometric phase Φ^G and the excess phase Φ^E:

$$\Phi^{total}(t) = \Phi^G(t) + \Phi^E(t) \tag{3.22}$$

The residual phase Φ^R, which is the difference of the total phase Φ^{total} and the predicted phase $\tilde{\Phi}$:

$$\Phi^R(t) = \Phi(t) - \Phi^{model}(t) \tag{3.23}$$

Substituting the total phase Φ from Equation 3.23 to Equation 3.22, we get the following for the excess phase:

$$\Phi^E(t) = \Phi^R(t) + \Phi^{model}(t) - \Phi^G(t) \tag{3.24}$$

Because our Doppler model currently only accounts for the geometry, $\Phi^{model} - \Phi^G$ is the prediction error due to the receiver noise, and as it is small, we can approximate the residual phase as excess phase. Throughout the following chapters of this work, the excess phase will refer to the OL residual phase expressed in meters.

3.6 OL signal threshold

As there is no feedback in the OL tracking process, a residual phase profile is continually being produced even after the satellite SNR is very low. However, the calculated phase, after the satellite signal disappears, is just a uniformly distributed random variable that does not contain any information [Acikoz, 2011]. The SNR is given by:

$$SNR = \frac{\sqrt{I^2 + Q^2}}{P_n} \tag{3.25}$$

where I_n and Q_n are the sums of the inphase and quadrature parts of the replica signal integrated over an integration time T_I [Ventre, 2006] as shown in the previous section, and P_n is the noise power after the satellite is lost.

For spaceborne RO signals acquired in OL mode, the truncation of the signal is based on the deviation of smoothed SNR from the background value at the end of the occultation [Sokolovskiy et al., 2010]. Acikoz [2011] determined that the OL phase in airborne RO becomes statistically randomly distributed when the 60 s moving

average of the SNR is equal to 1. We apply this criterion as a threshold to determine the end of reliable estimates of the OL residual phase. In the case of rising occltations this threshold is used to mark the start of the occultation.

3.7 Accuracy of OL tracking and filtering of the excess Doppler profiles

The 1 kHz OL residual phase profiles have a high level of noise compared to the 5 Hz conventional GPS receiver data. Noise present in the spaceborne RO profiles has been shown to induce biases in the retrievals [Sokolovskiy, 2001]. Therefore, after differentiating excess phase to get excess Doppler, we apply a Savitzky-Golay filter [Schafer, 2011] to filter out the random noise. To determine the cutoff frequency for doing this, we compare two independent measurements of the $L1$ phase from the Applanix and OL tracking receivers recording high elevation satellites on the top antenna for a one minute time series. The 1000 Hz OL data for PRN12 and PRN10 high elevation satellites are much noisier than the 10 Hz Applanix receiver data (Figure 3.3). There is a correlated noise in the PRN12 and PRN10 phase profiles which is attributed to the receiver clock error because the Applanix and GRS do not have a common clock. Since both PRN10 and PRN12 satellites are tracked using the same receiver, we use the single difference of the two profiles to remove this common receiver clock error, which is done as follows: The carrier phase observable measured at the receiver i at initial epoch t_0 is a function of the distance between the satellite k and the receiver i. In practice, it also contains various noise terms, such as the atmospheric effects expressed with tropospheric and ionospheric delay terms, as well as the clock errors in the satellite and the receiver, and carrier measurement noise including that due to local transmitter and receiver multipath. Therefore, the phase is usually modeled to include the following terms:

$$\lambda \cdot \phi_i^k(t_0) = \rho_i^k(t_0) + (h^k(t_0) - h_i(t_0)) \cdot c + \lambda \cdot N_i^k - \delta_{\text{ion}}^k + \delta_{\text{trop}}^k + n_i^k \tag{3.26}$$

where λ is the carrier wavelength, $\rho_i^k(t_0)$ is the geometric distance between the satellite and the receiver, $h^k(t_0)$ and $h_i(t_0)$ are the satellite and the receiver clock errors respectively, c is the speed of light, n_i^k includes the receiver noise and the noise due to the multipath, N_i^k is the phase ambiguity, which is the initial integer number of cycles between the satellite and the receiver, δ_{ion} and δ_{trop} are the propagation delays in units of meters due to the ionosphere and the troposphere.

For satellite m, this equation will be in the form of:

$$\lambda \cdot \phi_i^m(t_0) = \rho_i^m(t_0) + (h^m(t_0) - h_i(t_0)) \cdot c + \lambda \cdot N_i^m - \delta_{\text{ion}}^m + \delta_{\text{trop}}^m + n_i^m \qquad (3.27)$$

Since the receiver clock error term $h_i(t_0)$ is common in Equations 3.26 and 3.27 for the two satellites, taking the difference of these two equations will eliminate the $h_i(t_0)$ term.

Thus, the single difference of the PRN12 and PRN10 profiles discussed previously, will be free of receiver clock error, which is shown in Figure 3.4.

The 1000 Hz OL profile and the Applanix phase time series are each filtered using a Savitzky-Golay filter with a smoothing window size ranging from 0.2 s to 20 s. These smoothed OL and Applanix profiles are then differenced. At the optimal window size, the filtered time series for the Applanix and OL data will match the best. Figure 3.6 shows the standard deviation (SD) for Applanix and OL differences for different window sizes: the blue dashed line shows the SD for the non-smoothed difference profile, while the red dots correspond to the SD values for each window size being applied. The $SD = 0.0062$ m value for the non-smoothed difference decreases to 0.0013 m for a 5 s window size. In the airborne RO, the first Fresnel zone size is estimated to be $200 - 240$ m [Xie et al., 2008]. A 5 s smoothing window size leads to a vertical sampling of $100 - 200$ m below 8 km, which is smaller than the size of the Fresnel zone. Thus, we apply a 2^{nd} degree polynomial Savitzky-Golay filter with a 5 s smoothing window to reduce the random noise present in the airborne RO observations, while preserving the vertical resolution of the measurements. These filtered excess Doppler profiles will be used in this work to calculate bending angle profiles according to the method described in Chapter 1 (equations 1.3 through 1.6).

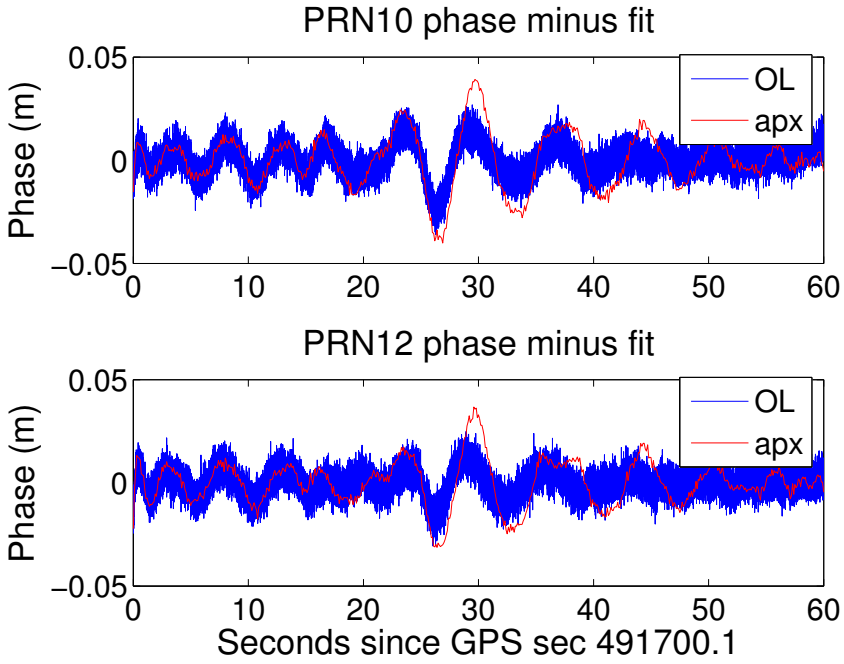

Figure 3.3.: L1 phase for high elevation PRN10 and PRN12 recorded on top antenna using GRS receiver (blue) and the Applanix receiver (red). The smooth long period change due to the range has been removed using a fit to the phase data for each satellite.

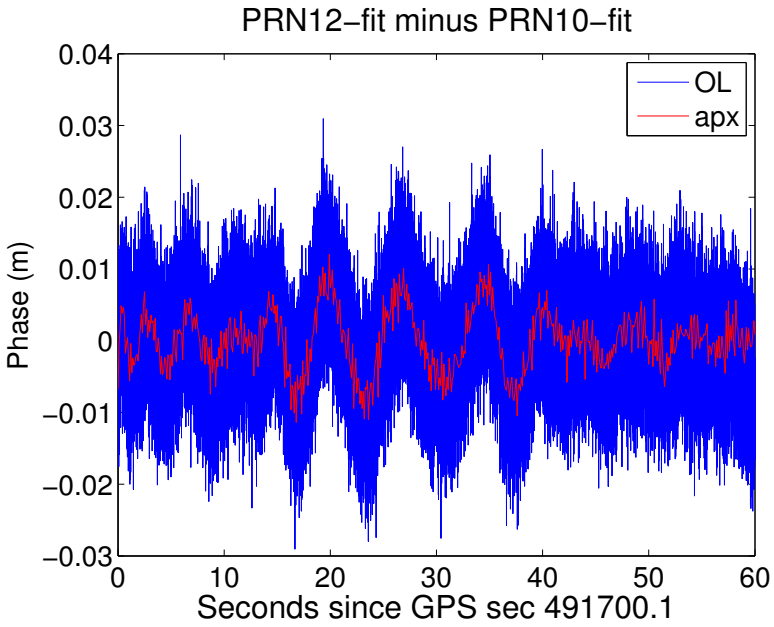

Figure 3.4.: The difference of PRN12 and PRN10 L1 phase for GRS receiver (blue) and the Applanix receiver (red) data.

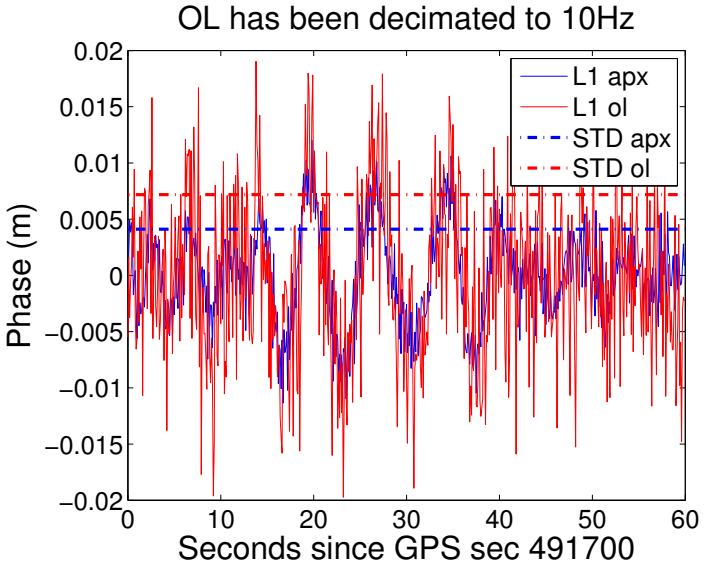

Figure 3.5.: The OL profile of PRN12 and PRN10 difference is filtered to 10 Hz for comparison with the 10 Hz Applanix data. The blue and red dashed lines show the standard deviation of 10 Hz OL and Applanix phase before smoothing.

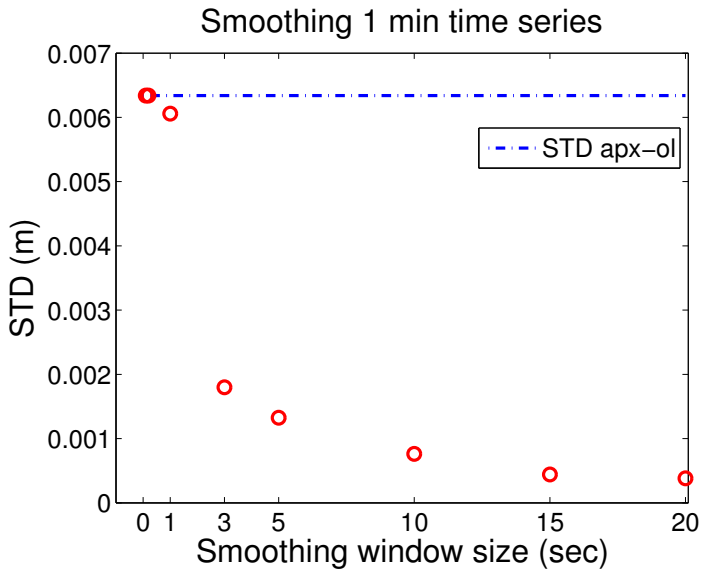

Figure 3.6.: Standard deviation of the difference of Applanix and OL phase profiles applying different smoothing window sizes. The blue dashed line shows the standard deviation of the applanix and OL phase difference before smoothing.

4. RETRIEVAL METHOD

The implementation of the retrieval of atmospheric refractivity profiles from the observations of the excess phase derived in Chapter 3 is based on the theory described in Chapter 1. This chapter describes the method used to make those calculations. It also describes the sensitivity of the retrieval to several assumptions about the atmosphere above flight level that are required for the retrieval, and the sensitivity to several sources of error.

4.1 Refractivity retrieval from RO measurements

The location and velocity of the airborne receiver are required for the geometric calculation of bending angle. Precise navigation measurements are critical in airborne RO retrieval as any errors associated with the airplane motion will map into the excess Doppler, thus affecting the quality of the retrieved refractivity profile [Muradyan et al., 2010]. For this reason, we use measurements from the high accuracy Applanix POS/AV GPS aided inertial navigation system (INS) to compute accurate navigation solutions for the aircraft. The POSPac post-processing software (POSPac MMS) allows computation of different types of GPS and GPS/INS solutions that have different approaches for removing clock and ionospheric errors.

In this work we calculate the navigation solution with Precise Point Positioning (PPP) [Hofmann-Wellenhof and Collins, 2001], which is an effective kinematic GPS processing technique for long flights that removes the requirement for reference stations that are necessary for differential processing. It uses precise clock and ephemeris information and insures decimeter level position accuracy. In the conventional PPP technique, the accuracy degrades if there is a data gap, requiring a long time for the

navigation solution to re-converge. However, the POSPac MMS uses inertial data to improve the precision and provide continuity over any outages [Hutton et al., 2008].

The precise airplane navigation solution containing the airplane position and velocity (in the file *geom_apx_gps_prnXX* in Figure 4.2) along with the precise positions for the occulting satellite from the IGS orbit file are used to compute the model Doppler time series (*Olpredict_dynamic.m* subroutine) used in the OL tracking method described in Chapter 3 (OLtrack in Figure 4.2). Since this Doppler model contains only the effects of source-receiver geometry in a vacuum, the OL tracking residual phase is the equivalent of the excess phase between the observations and the straight-line path (*OL_t_exphs_prnXX*).

Different approaches to filtering the excess phase and excess Doppler might result in a bias in the profile (F. Zus, C. Marquardt personal communication, 2012). GRAS processing uses a Savitzky-Golay filter [Luntama et al., 2008; von Engeln et al., 2009], while COSMIC uses a Gaussian filter [Kuo et al., 2004]. TerraSar-X RO excess Doppler profiles are smoothed using a Savitzky-Golay filter of 3^{rd} polynomial degree and a window size of 71 points (1.4 s). In this work the excess Doppler is 5 second smoothed using a second degree of polynomial Savitzky-Golay filter. A detailed discussion on filtering of excess Doppler profiles was presented in Chapter 3.

OLtrack is also run for the same time period for a high elevation satellite and an excess phase profile is derived for that satellite. Assuming the tropospheric delay for the high elevation satellite is negligible, which is reasonable for a receiver at 14 km altitude, the remaining excess phase contains the receiver clock error. The same filter is applied to the high elevation satellite data. The excess phase and Doppler profiles are differenced for the occulting and high elevation satellites to remove any correlated receiver clock errors ($phase.gXX - YY$ file in Figure 4.2, where X X is the occulting satellite number, and Y Y is the PRN number of high elevation satellite).

We define the occultation period as the time period when the excess Doppler is greater than 0.1 m/s. We calculate the mean airplane height during the occultation time period for the purpose of ellipticity corrections and estimating the refractivity

at the receiver. The ellipticity correction to the airplane-satellite geometry (*oblate* subroutine in Figure 4.2) is applied by shifting the center of the coordinate system from the center of the ellipsoidal Earth to the center of local curvature ($phase.gXX-YY\_shift$ in Figure 4.2). This procedure is explained in detail in Section 4.3. In this shifted coordinate system, atmospheric layers parallel to the Earth surface would be closer to satisfying the assumption of spherical symmetry.

The bending angle is calculated from the excess Doppler according to equations 1.3 through 1.6 (*dop2alp* subroutine). Because the aircraft is inside the atmosphere, we require the refractive index at the receiver height n_R. We extract this information from the in-situ measurements of atmospheric parameters measured at flight level. The refractivity at the receiver during the occultation period is calculated using an approach explained in Section 4.2. Because there were no in-situ measurements of water vapor at flight level in this campaign, we assume refractivity depends only on temperature. However, we would like to assure that the value of n_R at the receiver height is consistent with the atmospheric model that is assumed for the atmosphere above flight level. For this, we use the climatological monthly mean refractivity profiles from the Climate Impact on Regional Air Quality (CIRA-Q) model [Kirchengast et al., 1999] at the latitude of the aircraft at the time when the impact height is at a maximum. The difference of refractivity at the receiver values from the CIRAQ profiles and in-situ measurements for the February 15 2008 occultation cases has proved to be small, generally varying from 0.3 to 1 N-units.

We also simulate a bending angle profile using a 1-D atmospheric refractivity model for comparison with the bending profiles calculated from the airborne RO measurements. The CIRA-Q profiles extending to 20 km altitude are used in a forward integrator to generate the positive and negative elevation bending angles as well as the partial bending angle profile through Equations 1.12, 1.13 and 1.14 respectively.

To remove the effect of the random noise in the observed bending angle profiles at the height of the greatest impact parameter, we replace bending angle profile with the simulated one from the highest elevation angle extending down to 13.5 km

in impact height in the negative elevation bending region. The positive elevation bending section is also replaced with the simulated profile since we cannot retrieve unambiguous information for atmospheric heights above the aircraft. We have found that the retrieved bending angle is not a single-valued function of impact parameter, probably because of multipath propagation, below approximately 5 km in impact height. This introduces a problem in the numerical integration of Equation 1.15 and an inversion technique based on geometrical optics can no longer be used. However, in order to provide preliminary estimates of refractivity, we modify the bending angle profile, keeping in mind that the results below this height will have to be interpreted with caution. We implement an interpolation method for the bending angle that reduces the size of the change in bending with impact height until the values are single-valued. The partial bending angle from RO measurements is then calculated as the difference of these modified negative and positive elevation bending angles (Equation 1.14). As final step in the retrieval, the partial bending angle profiles are inverted via Abel inversion expressed with Equation 1.15 to yield for refractivity profiles as a function of geometric height.

Figure 4.1 is a schematic representation of the refractivity retrieval described above.

4.2 Calculation of refractivity from model analysis and radiosonde profiles

After retrieving refractivity profiles from airborne RO measurements that have been post-processed in OL mode, we would like to compare the profiles with values derived from independent measurements as well as NWP model profiles. This comparison is best done with the fewest assumptions in terms of refractivity as a function of height. However, this requires conversion of meteorological variables to refractivity and conversion of the vertical pressure coordinates to geometric height. Radiosonde profiles include geopotential height, atmospheric temperature, relative

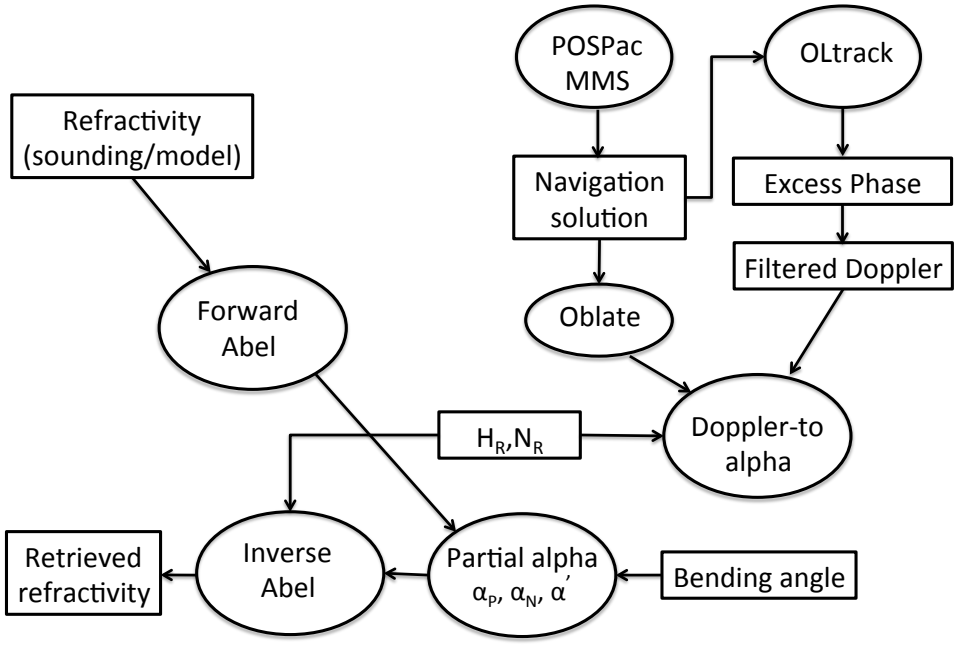

Figure 4.1.: Schematic representation of geometric optics retrieval processing system.

humidity and the total pressure. These same parameters are also included in the European Centre for Medium-Range Weather Forecasts (ECMWF) Year of Tropical Convection (YOTC) analysis. The ECMWF profiles provide an excellent source for retrieval validation because they are the result of a multi-year effort for coordinated observing, modeling and forecasting of organized tropical convection (`http://www.ucar.edu/yotc/`) that includes our study region. We calculate refractivity through equation 1.11 using the atmospheric parameters provided in the radiosonde and ECMWF profiles. Recent research has demonstrated that there is some sensitivity of the ECMWF NWP analysis to the variation of atmospheric compressibility in the empirical refractivity coefficients [Aparicio et al., 2009; Healy, 2011]. This is detectable in the high precision spacebore GPS RO measurements at high levels. However, for the airborne profiles, Equation 1.11 is sufficiently accurate for the current comparisons. Pressure is the sum of partial pressures of dry air P_d and water

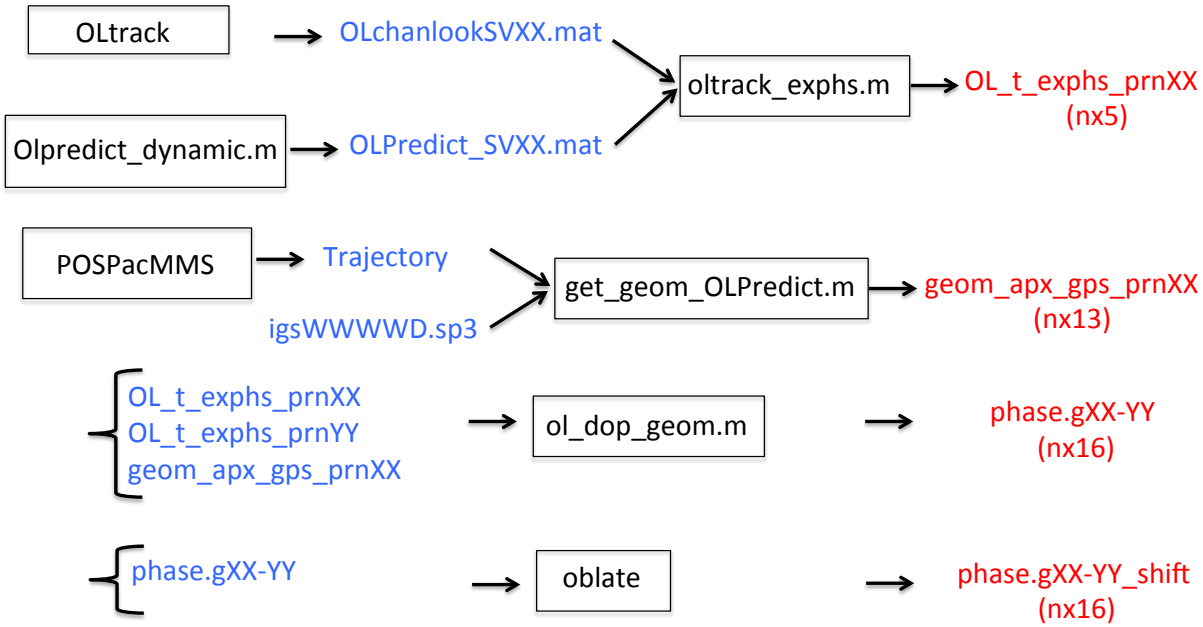

Figure 4.2.: Inputs and outputs of subroutines for preparing files necessary for the retrieval.

vapor P_w. Partial pressure of water vapor, P_w, can be calculated from the radiosonde humidity measurements using the definition of relative humidity as the ratio (in percent) of P_w and the water vapor pressure at saturation (e_{sat}) at a given temperature T :

$$RH = \frac{P_w}{e_{sat}(T)} \tag{4.1}$$

Dry air pressure is then calculated as $P_d = P - P_w$.

Several authors have addressed the calculation of the saturation vapor pressure [Buck, 1981; Murphy and Koop, 2005; Murray, 1966; Vedel et al., 2001]. In our calculations

we use a method for calculating e_{sat} that takes into account a region of sub-zero temperatures, where three phases of water can be present simultaneously [Vedel et al., 2001].

$$e_{sat}(T) = a_1 exp\left(a_2 \frac{T - T_{melt}}{T - a_3}\right) \tag{4.2}$$

where $T_{melt} = 273.16\ K$, $a_1 = 610.78\ Pa$, and the constants a_2 and a_3 linearly vary between the values in the $[T_{melt} - 15; T_{melt}]$ temperature interval as follows:

$$a_2 = \begin{cases} 17.269\ K & \text{for } T \geq T_{melt} \\ 21.875\ K & \text{for } T \leq T_{melt} - 15 \end{cases} \tag{4.3}$$

$$a_3 = \begin{cases} 35.86\ K & \text{for } T \geq T_{melt} \\ 7.66\ K & \text{for } T \leq T_{melt} - 15 \end{cases} \tag{4.4}$$

The two sets of constants correspond to the water vapor saturation pressure over a surface of liquid water and ice respectively. The use of a combination in the 15 degree window below the freezing temperature accounts for the effect of three phases of water in that temperature interval. In our calculations, the a_2 and a_3 values have been interpolated for the $T_{melt} - 15 < T < T_{melt}$ temperature region.

The radiosondes do not directly measure height, therefore the profiles provide calculated values of the geopotential height, which was introduced so that the pressure, temperature and relative humidity measured at different radiosonde sites could be compared on the same altitude scale. However, the RO measurements (and simulations) are carried out with respect to geometric height from the center of the Earth, therefore we use geometric height instead of the geopotential height. The standard calculation for the geometric height for a given latitude and longitude, taking into consideration the variation of gravity and the geoid is provided in M. J. Mahoney [A discussion of various measures of altitude, available at `http://mtp.jpl.nasa.gov/notes/altitude/altitude.html`].

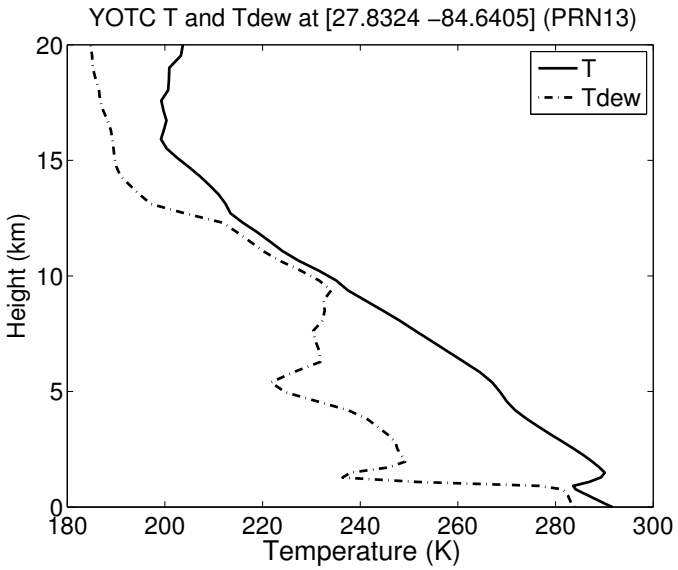

Figure 4.3.: Temperature (solid line) and dew point temperature (dashed line) profiles from ECMWF analysis profile at 18Z on February 15, 2008 retrieved for comparison with PRN13 setting occultation profile. Location for ECMWF analysis profile is [Lat lon] = [27.75 -84.750].

The comparisons can now be made directly among retrieved refractivity, independent data and models without concern for the effect of any further assumptions made in the retrieval of moisture and temperature from the RO observations. This is also the most useful error to characterize for future data assimilation of the RO profiles into NWP models, because the assimilation operators are based on refractivity or bending angle.

4.3 Accounting for the Earth's ellipticity

When calculating bending angles and impact parameters from the phase delay data in both spaceborne and airborne RO techniques, it is important to take into account the elliptical shape of the earth. Syndergaard [1998] has demonstrated that failing to take into account the Earth's oblateness in the geometric conversion from

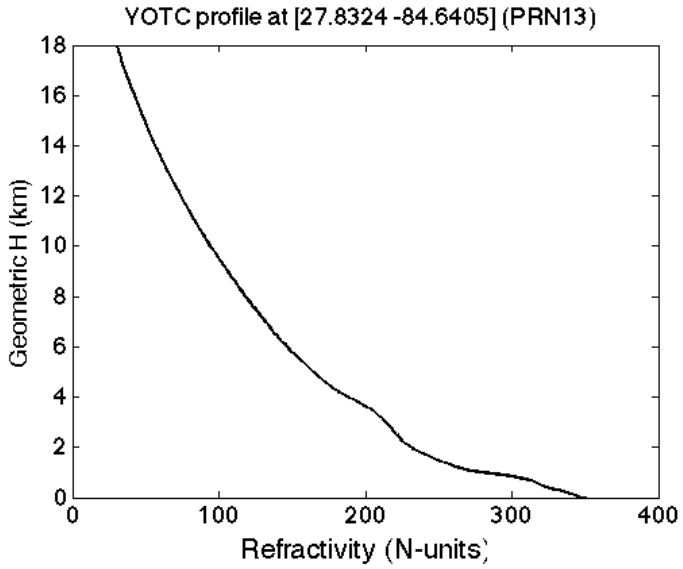

Figure 4.4.: Refractivity calculated from ECMWF analysis profile at 18Z on February 15.

Doppler to bending angle causes as large as 6 K temperature bias close to the surface and 3 K bias at 10 km altitude. If the Earth's center is used as the center of refraction in the retrieval, it will result in an incorrect bending angle α^* and impact parameter a^* (Figure 4.5) since the estimates of the ray angles will not be relative to the local horizontal, and thus, not perpendicular to the local refractivity gradients. Errors associated with the incorrect bending angle will propagate through the Abel transform inversion and affect the refractivity retrieval. Therefore, we use a center and a radius of curvature appropriate to the latitude and orientation of the RO measurement [Syndergaard, 1998].

The Abel transform procedure [Healy et al., 2002] assumes a fixed center of refraction, and it can be approximated by the center of a sphere tangential to the ellipsoid at the profile location, which has a radius equal to the radius of curvature in the occultation plane.

From Syndergaard [1998] we have the following derivation. To find the local normal to the ellipsoid, an equation for the ellipsoidal surface is defined (in cartesian

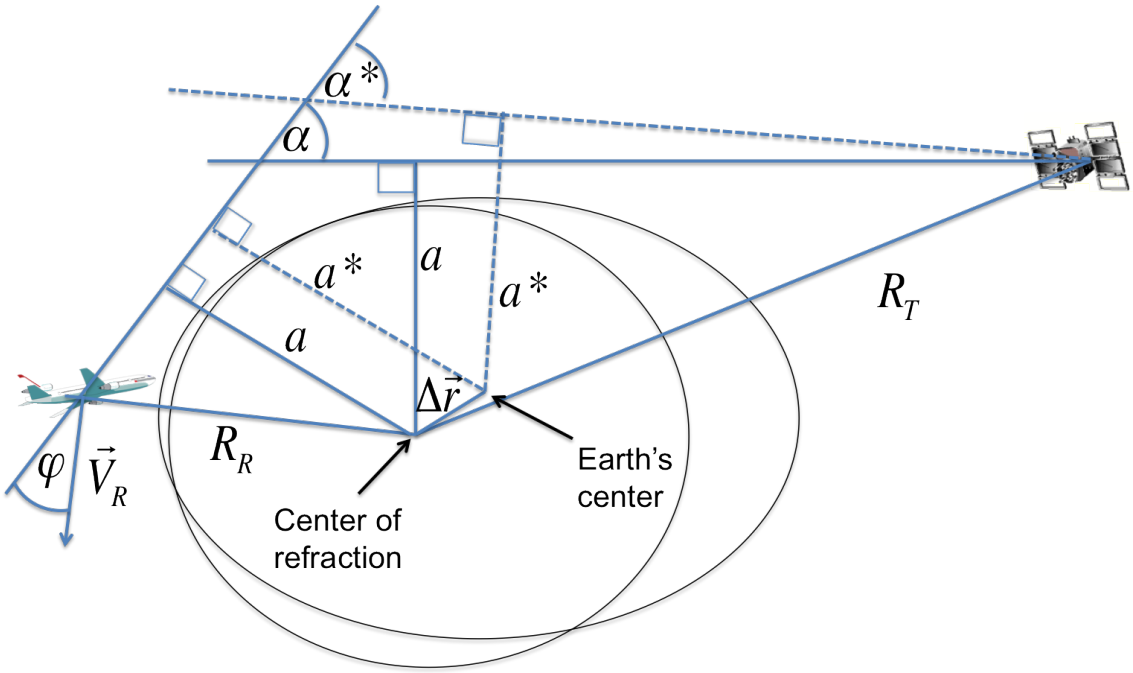

Figure 4.5.: Cross section of the oblate Earth and a sphere tangent to the surface of the Earth at the lowest tangent point of the occultation.

coordinates) as $S(x, y, z) = const.$ Thus, if $R(x, y, z)$ is the geocentric radius through co-latitude θ, the following will hold true:

$$S(x, y, z) = \sqrt{x^2 + y^2 + z^2} - R(x, y, z) = 0 \tag{4.5}$$

The geocentric radius can be expressed by the following equation:

$$R = R_{eq}(1 - f cos^2\theta) \tag{4.6}$$

where R_{eq} is the Earth's semi-major axis, f is the flattening, and $cos\theta = \frac{z}{\sqrt{x^2+y^2+z^2}}$. For a given vector $\vec{r} = (x, y, z)$ and a corresponding value of co-latitude, we search for the values of x, y, z for which $S = 0$, and thus lies on the ellipsoidal surface.

If $\hat{r} = (\tilde{x}, \tilde{y}, \tilde{z})$ is a unit vector in the direction of the local geocentric radius, the vector $\bar{n_s}$ in the direction of the normal to the surface is expressed as:

$$\bar{n}_s = \hat{r} - 2f\tilde{z}\begin{pmatrix} \tilde{x}\tilde{z} \\ \tilde{y}\tilde{z} \\ \tilde{z}^2 - 1 \end{pmatrix} \tag{4.7}$$

The vector radius of curvature in the occultation has the properties that:

$$\bar{R}_c = \frac{\tilde{n}_s}{|\frac{d\hat{n}_s}{ds}|} \tag{4.8}$$

where $\frac{d}{ds}$ is the derivative along the surface in the occultation plane, and $\hat{n}_s$ is the unit vector in the direction of $\bar{n}_s$. Taking into account that $\bar{n}_s$ is a unit vector to first order in f, it can be shown that $\bar{R}_c = \frac{\bar{n}_s}{|\frac{d\bar{n}_s}{ds}|}$. The derivative $\frac{d\bar{n}_s}{ds} = \frac{d(\nabla S)}{ds}$ can be calculated as:

$$\frac{d\bar{n}_s}{ds} = [(\hat{n}_p \cdot \nabla)\nabla S]_{S=0} = \boldsymbol{J}_s \hat{n}_p \tag{4.9}$$

Here $\boldsymbol{J}_s$ is the matrix giving the second derivatives of S at the surface.

$$\boldsymbol{J}_s = \begin{bmatrix} \frac{\partial^2 S}{\partial x^2} & \frac{\partial^2 S}{\partial x \partial y} & \frac{\partial^2 S}{\partial x \partial z} \\ \frac{\partial^2 S}{\partial y \partial x} & \frac{\partial^2 S}{\partial y^2} & \frac{\partial^2 S}{\partial y \partial z} \\ \frac{\partial^2 S}{\partial z \partial x} & \frac{\partial^2 S}{\partial z \partial y} & \frac{\partial^2 S}{\partial z^2} \end{bmatrix}_{S=0} \tag{4.10}$$

The approximate center of refraction with respect to the Earth centered system, having $\bar{R}_c$, is:

$$\Delta\bar{r} = R\hat{r} - \bar{R}_c \tag{4.11}$$

The coordinates of the transmitter and the receiver are then shifted from the center of the ECEF reference system by offset $\Delta\bar{r}$, so that they are now relative to the local center of curvature, and the impact parameter and bending angle are found as in the case of spherical symmetry.

5. PROFILING THE ATMOSPHERE WITH THE AIRBORNE GPS RADIO OCCULTATION TECHNIQUE USING OPEN-LOOP TRACKING

(An article to be submitted to the Journal of Geophysical Research)

Paytsar Muradyan[1], Jennifer S. Haase[1], Ulvi Acikoz[2], James L. Garrison[2], Feiqin Xie[3], Tyler Lulich[2], Brian Ventre[2]

1 *Purdue University, Department of Earth & Atmospheric Sciences, West Lafayette, IN 47907*

2 *Purdue University, Department of Aeronautics and Astronautics Engineering, West Lafayette, IN, 47907*

3 *Joint Institute for Regional Earth System Science & Engineering, University of California, Los Angeles, CA, 90095*

Corresponding author:

Paytsar Muradyan

Purdue University

Department of Earth & Atmospheric Sciences

550 Stadium Mall Dr.

West Lafayette, IN, 47907-2051

email: pmuradya@purdue.edu

Phone: (765)494-6787

Fax: (765)496-1210

Abstract

The GNSS Instrument System for Multistatic and Occultation Sensing (GISMOS) was designed for dense sampling of meteorological targets using the airborne radio occultation (RO) technique. The limb-sounding technique measures the Doppler shift in the carrier wave due to refraction of the Global Positioning System (GPS) signals and retrieves refractivity profiles that are directly related to pressure, temperature and moisture. This new technique has the potential for improving numerical weather prediction (NWP) forecasts by providing many more high vertical resolution atmospheric profiles in an area of interest, compared to other currently available techniques such as spaceborne radio occultation. The GISMOS system includes conventional dual frequency geodetic quality receivers for closed-loop (CL) signal tracking from side-looking antennas. In the lower troposphere, CL fails to track the GPS signal due to rapid phase accelerations, presumably due to strong gradients in atmospheric moisture and temperature. Therefore the system was designed to also include a GPS radio frequency (RF) signal recorder to provide data for post-processing using open-loop (OL) tracking in a software receiver. Radio occultation signals processed in OL mode enable reliable atmospheric profiling at these lower altitudes.

We present a comprehensive analysis of the performance of the airborne OL tracking algorithm for rising and setting occultations during a flight from the Gulf of Mexico to Colorado. We demonstrate that the OL tracking consistently reaches as low as 0.5 to 3.4 km in the atmosphere, for both rising and setting occultations. The only missed occultations were due to missing or erroneous ancillary navigation data from the global tracking network and aircraft turns. Based on this success rate, the system on a straight flight path would achieve three occultations per hour of flight time. The refractivity profiles found using a geometric optics retrieval technique agree reasonably well with the European Center for Medium Range Weather Forecasting (ECMWF) analysis profiles at upper and mid-tropospheric levels. This dataset shows a larger bias than similar datasets from airborne measurements at lower latitudes, but

is within the range of the observation errors typically assigned to RO data below 10 km during assimilation. Potential causes for the current biases in the retrieval as well as the prospects for reducing them are discussed.

Signal tracking and retrieval in the lower troposphere continues to be a major challenge for spaceborne RO, and has limited its impact in NWP below 10 km altitude. The airborne system represents a relatively cost-efficient means for investigating and testing new signal analysis techniques that may ultimately provide a significant improvement in the quality of future spaceborne RO datasets, a result of the full-bandwidth signal recording, OL tracking configurations and deployment flexibility.

Keywords: GNSS, Airborne Radio Occultation, Open-loop Tracking, Retrieval Accuracy

5.1 Introduction

Airborne RO refers to an atmospheric limb sounding technique in which GPS signals are recorded at a receiver onboard an aircraft as the satellites descend beyond the limb of the Earth. The GPS signal experiences refractive bending as well as a delay in the travel time through the atmosphere. From this bending, it is possible to retrieve information about atmospheric refractivity, which in turn depends on partial pressures of water vapor and dry air, and atmospheric temperature. GPS L-band signals are unaffected by clouds and precipitation making it possible to use airborne RO to probe storm systems with deep convection, and the derived profiles have high vertical resolution compared to atmospheric sounders.

The RO technique has been used in exploring the atmospheres of other planets since the 1960s [Fjeldbo et al., 1971], however it was not until the late 1980s that this technique was suggested for studying the Earth's atmosphere [Yunck et al., 1988]. The capabilities of GPS RO were demonstrated with the proof-of-concept Global Positioning System/Meteorology (GPS/MET) mission in 1992. The number of low Earth orbiting (LEO) satellites has increased significantly since then, to include the six-satellite Constellation Observing System for Meteorology Ionosphere and Climate (COSMIC) [Anthes et al., 2000; Schreiner et al., 2007], SAC-C [Hajj et al., 2004], Challenging Minisatellite Payload (CHAMP) [Wickert et al., 2005], the RO instrument GRAS on board Metop-A [GRAS-SAG, 1998], Gravity Recovery And Climate Experiment (GRACE) [Wickert et al., 2005], and the TerraSAR-X satellite mission [Werninghaus et al., 2004]. The Communications/Navigation Outage Forecasting System (C/NOFS) [de La Beaujardiere et al., 2004] provides RO profiles concentrated in tropical latitudes from its Occultation Receiver for Ionospheric Sensing and Specification (CORISS) instrument, and the Radio Occultation Sounder of the Atmosphere (ROSA) is now operational on board the OCEANSAT-2 satellite [Perona et al., 2007]. The RO data from many of these missions are processed and made available at the COSMIC Data Analysis and Archiving Center (CDAAC) [Kuo et al.,

2004]. Spaceborne RO profiles are assimilated into NWP models at many operational centers [Cucurull, 2007; Healy and Thepaut, 2006; Rennie, 2010; Wee and Kuo, 2008] and have shown a positive impact in global models in the upper troposphere and lower stratosphere. However, for focused studies of specific weather systems at the regional scale, the distribution of spaceborne RO profiles within a region and time period of interest is sparse. The airborne RO technique, where many observations can be made within a focused area, is of interest not only to improve forecasting for targeted weather systems, but also to advance the use of RO observations for this scale of problem as the constellation of spaceborne receivers develops.

The lower troposphere is a challenging environment for the GPS RO technique because rapid changes in moisture content, sharp temperature inversions, and lateral inhomogeneity contribute to multipath propagation and low signal strength. Open-loop (OL) tracking receivers were developed for missions following GPS/MET in order to improve measurements in the lower troposphere. However, there is still a sharp decrease in the number of observations available at 1 km compared to 10 km in the COSMIC archive because of these problems [Kuo et al., 2004]. Large biases are present in the retrievals below 3 km [Ao et al., 2003]. Therefore, there is a need for an increased number of independent lower tropospheric sounding measurements to make progress in retrieval and assimilation methods at these heights.

The idea of airborne RO was first suggested by Zuffada et al. [1999]. They illustrated the concept using a mountaintop receiver where signals could be recorded below the local horizon. Lesne et al. [2000] performed a sensitivity analysis of simulated airborne RO observations and showed that the technique could feasibly provide a large quantity of profiles, given reasonable assumptions for the data accuracy. Healy et al. [2002] proposed a modification to the inversion method for the airborne RO measurements using a partial bending angle, which is the difference of negative and positive elevation bending angles. Theoretically, this makes it possible to remove the effect of the atmosphere above the aircraft. Later studies implemented the airborne RO retrieval technique and made the first analysis of retrieval errors using simula-

tions [Xie et al., 2008]. The first study that looked at the impact of different types of navigation system noise from actual aircraft measurements found that retrieval of refractivity with less than 0.5 % error was possible [Muradyan et al., 2010]. Haase et al. [2012] published the first comparisons of airborne RO retrievals from a similar system deployed on stratospheric balloons that agreed closely with global model fields.

The GNSS Instrument System for Multistatic and Occultation Sensing (GISMOS) was deployed in February 2008 on the National Science Foundation (NSF) Gulfstream V aircraft for a series of research flights to demonstrate the airborne RO technique. The system recorded data from conventional closed-loop (CL) tracking receivers as well as data the GPS Recording System (GRS) for OL tracking. The initial results analyzing the data set from the conventional CL tracking receivers were limited by the receiver capabilities (Figure 5.1). The excess Doppler shift (after removing the effects of the relative transmitter and receiver geometry) is expected to increase with time due to refractive bending as the GPS satellite sets. This is shown in Figure 5.1 (black and gray dash-dotted lines in the left panel) for simulations of occulting satellites PRN05 and PRN12, given a flight altitude of 12.4 km and the orbital trajectories for 22 February 2008. An example of recordings from a conventional CL receiver for PRN05 and PRN12 are also shown, in gray and black respectively. The excess Doppler reached a maximum value of 0.3 m/s for PRN12, at which point the receiver lost lock. PRN05 shows a large gap before losing lock at less than 0.1 m/s. The CL receivers rely on feedback loops to track the signal, which assumes the carrier phase is smoothly varying in time. The data loss is probably due to signal fading and rapid phase fluctuations when the signal propagates though sharp refractivity gradients at low elevation angles. Also seen in the figure are variations in the Doppler attributed to the receiver clock errors, which are common to the two satellites. Therefore, it is necessary to use an excess Doppler profile for a high elevation satellite (which should show little variation aside from the receiver clock), to eliminate the common clock errors through single differencing.

An example of the potential improvement possible with OL tracking is shown in Figure 5.2. This method replaces the traditional feedback loops that adjust the Doppler shift of the replica carrier phase in the receiver hardware, and tracks the signals relative to an a priori estimate of the Doppler. The OL tracking excess Doppler profile for PRN12 extends up to 0.62 m/s (light gray dash-dotted line in Figure 5.2), which is a significant improvement over the conventional CL result. In this work we describe the method used for the OL tracking and analyze all airborne RO profiles for one long continuous flight to evaluate the performance of the OL tracking of the airborne RO system.

5.2 Field campaign and data

GISMOS tracks both setting and rising satellites through side-looking, high gain, narrow field of view antennas. The antennas have a peak gain at the horizon of 9.4 dB on L1 (1575.42 MHz) and 7.7 dB on L2 (1227.60 MHz) frequencies. The gain drops 3 dB at $\pm 18^\circ$ elevation relative to the horizon and $\pm 25^\circ$ azimuth relative to the side-looking direction, and drops 10 dB at $\pm 30^\circ$ elevation and $\pm 40^\circ$ azimuth. The incoming signals from the side antennas are split so that RO measurements are collected with both conventional dual frequency CL receivers (Trimble NetRS) and the 10 MHz GPS Recording System (GRS). The top antenna is used for the Applanix POS/AV 510 GPS/Inertial Navigation System (INS), which provides aircraft position and velocity, with a specified velocity accuracy of 5 mm/s [Muradyan et al., 2010]. The signal from the top antenna is also recorded by the GRS to provide high elevation satellite reference data for removing any residual clock error.

GISMOS was deployed on the NSF High-performance Instrumented Airborne Platform for Environmental Research (HIAPER) Gulfstream V aircraft for a series of flights with the purpose of validating the system in comparison to radiosondes. The data analyzed in this work was recorded by GISMOS during a 5-hour flight at a level of 13.5 km on 15 February 2008. The aircraft took off from Louisiana,

flew over the Gulf of Mexico, and landed in Colorado (Figure 5.3). The Applanix navigation system recorded continuously, with its internal GPS sampling at 10 Hz, and its inertial measurement unit sampling at 200 Hz. The Trimble NetRS receivers recorded carrier phase and pseudorange GPS observables continuously from the port and starboard antennas at 5 Hz. The GRS continuously sampled the RF signal from the top, port, and starboard antennas at 10 MHz. In-situ measurements of temperature were made at flight level at 50 Hz with a fast response, all weather deiced (Rosemount Model 102AL TAT) sensor with ± 0.5 C$^\circ$ accuracy (http://www.hiaper.ucar.edu/handbook/index.html). In-situ pressure was measured at flight level with Paroscientific Model 1000 Digiquartz Transducer (accuracy ± 1 mb).

Given the flight path (dot-dashed line in Figure 5.3) and the GPS orbits, 19 occultations were predicted while the aircraft was at cruising altitude. Ten of these occultations were predicted to be setting, and nine were rising. The tangent point, which is the point closest to the Earth on the ray path between the transmitter and receiver, drifts horizontally during the occultation. In the airborne geometry the drift can range from 200 to 500 km [Lesne et al., 2002]. The tangent point drifts for each of the predicted occultations are illustrated with black and gray lines for setting and rising occultations respectively. The crosses show the European Center for Medium Range Weather Forecasting (ECMWF) analysis profile locations that have been extracted for comparison near the tangent point locations.

5.3 Open-loop tracking method

A major challenge for the RO technique in the troposphere is obtaining continuous time series of amplitude and phase in the presence of sharp refractivity gradients causing premature signal tracking loss [Sokolovskiy, 2001]. We apply the OL tracking method to raw samples of the GPS signal to mitigate this problem. The OL tracking algorithm is explained in Beyerle et al. [2006], and implemented for airborne RO by Ventre [2006]. In this method, the satellites are first acquired and tracked in

CL tracking mode implemented in a software receiver [Acikoz, 2011; Heckler and Garrison, 2004]. The presence of signals is determined and rough estimates of Doppler frequency are obtained in the acquisition process. Then, through multiple feedback control loops, the errors between the incoming and the locally generated replica signal are minimized [Acikoz, 2011]. A delay lock loop (DLL) refines the initial estimate of code delay by correlating with the incoming signal; a frequency lock loop (FLL) refines the estimate of Doppler frequency, and the phase lock loop (PLL) updates the estimate of Doppler and carrier phase.

This is followed by the OL tracking of the signal with a goal to extract time varying phase information $\Phi(t)$ from the received and down-converted GPS signal $u_{IF}(t)$ expressed through the following equation:

$$u_{IF}(t) = A(t)p(t-\tau)D(t-\tau)e^{j(2\pi f_{IF}t+\Phi(t)+\Phi_0)} + n_{IF}(t) \tag{5.1}$$

Here Φ_0 is the initial phase at $t = 0$, $A(t)$ is the amplitude at the time of reception, $p(t)$ and $D(t)$ are the ranging code and the navigation data message respectively delayed by τ (time varying path-length delay), f_{IF} is the carrier wave at the intermediate frequency, and n_{IF} is the additive, white Gaussian noise term.

The OL tracking relies on a pre-defined Doppler frequency model, $f_D^{model}(t)$, which is calculated from the relative position and velocity vectors of the receiver and the transmitter. For the retrievals, the velocity accuracy is required to be 0.005 m/s in order to retrieve a nominal accuracy of 0.5 % refractivity up to 0.5 km below the flight level [Muradyan et al., 2010]. We calculated the position and velocity of the aircraft using the Applanix POSPac MMS post-processing software [Mostafa et al., 2001] in a two step process to 1) compute a 10 Hz precise point positioning GPS solution, then 2) compute an optimal integrated inertial navigation solution with loose coupling of the GPS position and the high precision IMU data. In the first step, ionospheric free observations were used with a 12.5^0 elevation angle cutoff. Precise final orbits and clocks were used from the International GNSS Service. Forward and reverse Kalman filter solutions were averaged to provide a smoothed combined solution. In

the second step, a smoother was run to estimate optimal error corrections to the linear acceleration and angular rates measured by the IMU, based on the precise GPS positions [Alban et al., 2003; Mostafa et al., 2001]. Then, the error corrections were applied to the IMU data in a feed forward control module to obtain the final best estimate of position, velocity, and orientation of the aircraft. Our estimate of the position precision is better than 6 cm in the horizontal and 90 cm in the vertical, and better than 5 mm/s velocity precision in all components [Muradyan et al., 2010]. The satellite positions required for the geometric Doppler calculation are obtained from the precise IGS orbit files, and are available in 15 minute intervals. These are then interpolated to 1 KHz rate using a Lagrangian interpolation method [Schenewerk, 2003; Ventre, 2006]. Corrections are made for the satellite clocks, also provided in the IGS orbit files.

To remove the code from the received signal, it is multiplied by a replica of the ranging code at estimated delay $\hat{\tau}$, which is pre-computed from the Doppler model [Lulich et al., 2010]. Assuming that the accuracy of $\hat{\tau}$ is sufficient for the received signal and the estimated ranging code alignment within a small fraction of a code chip, then:

$$p(t-\tau)p(t-\hat{\tau}) \approx 1 \tag{5.2}$$

The signal following the code wipe-off is expressed through the following equation:

$$u_s(t) \cong A(t)D(t-\tau)e^{j(2\pi f_{IF}t+\Phi(t)+\Phi_0)} + n_s(t) \tag{5.3}$$

where the noise, $n_s(t) = p(t-\hat{\tau})\, n_{IF}(t)$, is assumed to have the same statistics as $n_{IF}(t)$ since $p(t)$ is independent and $|p(t)|^2 = 1$. The subsequent evolution of the code delay over the tracking period is updated based on the pre-defined Doppler model once the initial code delay is known.

After the code wipe-off, the carrier wipe-off is performed by multiplying the post code wipe-off signal by a complex exponential replica signal $v(t)$.

$$v(t) = e^{-j(2\pi f_{IF} t + \Phi^{model}(t))} \tag{5.4}$$

Here $\Phi^{model}(t)$ is the time varying predicted phase determined from the predicted Doppler from the following relationship:

$$f_D^{model}(t) = \frac{1}{2\pi} \frac{d\Phi^{model}(t)}{dt} \tag{5.5}$$

The model phase at the time t_n is the accumulated Doppler from $n-1$ previous integration times:

$$\Phi_n^{model} = 2\pi T_I \sum_{j=1}^{n-1} f_{D,j}^{model} \tag{5.6}$$

where $\Phi_n^{model} \equiv \Phi^{model}(t_n)$ and $f_{D,j}^{model} \equiv f_D^{model}(t_j)$. The product of u_s and v is integrated over the period of T_I to form the complex correlator sum Ψ_n:

$$\Psi_n = \frac{1}{T_I} \int_{t_n}^{t_n + T_I} u_s(t)\, v(t) dt + N_n \tag{5.7}$$

The integration time T_I is set to one code period, which varies with time due to the Doppler frequency. If it is assumed that the frequency and amplitude can be approximated as $A_n \equiv A(t_n)$ and $f_{D,n} \equiv f_D(t_n)$, and that the data bit is constant over the period of integration, the result of the code wipe-off can be written as:

$$\Psi_n = \frac{A_n D_n}{T_I} \int_{t_n}^{t_n + T_I} e^{j(\Phi(t) - \Phi^{model}(t))} dt + N_n \tag{5.8}$$

$$\Psi_n = A_n D_n sinc(\pi \delta f_{D,n} T_I) e^{\frac{\delta\Phi_n + \delta\Phi_{n+1}}{2}} + N_n \tag{5.9}$$

where $\delta f_{D,n} = f_{D,n} - f_{D,n}^{model}$ and $\delta\Phi_n = \Phi_n - \Phi_n^{model}$ are the differences of the true and predicted Doppler and phase respectively.

Due to low signal power during an occultation, the phase measurements usually have discontinuities. The OL tracking result, the complex correlator Ψ_n, consists of real and imaginary components referred to as inphase, i_n, and quadrature, q_n. To

increase the SNR and reduce the probability of cycle slips, these components are coherently integrated over a single data bit, also lowering the measurement rate from 1 kHz to 50 Hz.

$$I_k = \sum_{n=20(k-1)+1}^{20k} i_n \qquad\qquad Q_k = \sum_{n=20(k-1)+1}^{20k} q_n \tag{5.10}$$

The residual phase Φ^R is then calculated as the angle between the in phase and quadrature components of the correlation sums through the use of four-quadrant arctangent function:

$$\Phi^R_{k+1} = atan2(\frac{Q_k}{D_k}, \frac{I_k}{D_k}) + C_k \tag{5.11}$$

Thus, the calculation of the residual phase requires information on the navigation data bit D_k, which is acquired from the COSMIC data bit archive. The constant term C_k in Equation 5.11 is added to eliminate the cycle slips and it takes the following values:

$$C_k = \begin{cases} C_{k-1} + 2\pi & \text{if } \Phi_k < -\pi \\ C_{k-1} - 2\pi & \text{if } \Phi_k > +\pi \\ C_{k-1} & \text{else} \end{cases} \tag{5.12}$$

The residual phase Φ^R is defined as the difference of the total $\Phi^{total}(t)$ and the model $\Phi^{model}(t)$ phase:

$$\Phi^R(t) = \Phi^{total}(t) - \Phi^{model}(t) \tag{5.13}$$

As we only account for the geometry in the calculation of the model phase, the residual phase effectively serves as an estimate of the excess phase due to the atmosphere, which we will refer to throughout this work.

For the setting occultations, the CL tracking acquires the satellite at high elevation ($>10^0$) when the signal power is high. This allows recovery and estimation

of the navigation data bits that modulate the signal. This is then used to initialize synchronization with the data bits that are retrieved from a global tracking network for the low elevation angle time period of the occultation. For the rising occultation cases, the satellite is acquired well after the start of the occultation, when the signal power reaches a sufficiently high level. Then, the OL tracking is initialized in a similar manner to the setting case, however the OL tracking is run in reverse time to recover the time period before CL tracking began. Currently we run the OL tracking only on the L1 signal.

Since there is no feedback in the OL tracking process, it continues to estimate the residual phase even after the satellite signal has disappeared. At this point, the calculated phase becomes a uniformly distributed random variable that does not contain any useful information. For spaceborne RO signals acquired in OL mode, the truncation of the signal recording is based on the deviation of smoothed SNR from a background value at the end of an occultation [Sokolovskiy et al., 2010]. Acikoz [2011] determined that for the airborne data, the statistics of the OL phase become randomly distributed when the 60-second moving average of the SNR is equal to 1. We apply this criterion as a threshold to determine the end of reliable estimates of the OL residual phase.

The OL tracking phase was compared with the phase recorded by the conventional CL tracking receiver, to estimate the OL tracking accuracy. Typically, the accuracy of the GPS phase observable is 1 % of the wavelength of the carrier phase, or about 2 mm [Hofmann-Wellenhof and Collins, 2001] for high SNR signals. Acikoz [2011] concluded that the error rate for the OL tracking is 0.9 mm/s, however lower SNR increases this error, and during an occultation rapid signal fading is common.

We compared the OL tracking phase data recorded from the top antenna with the 10 Hz carrier phase data recorded by the Applanix navigation receiver, which was connected to the same signal split from the top antenna. The difference between PRN12 and PRN10 high elevation phases are compared for each data stream to remove the error in the receiver clocks, because the two systems do not have a synchronized clock.

Figure 5.4 shows that the OL data sampled at 1000 Hz is much noisier than the 10 Hz Applanix data. For 1 minute of data for the high elevation PRN12 and PRN10 phase difference, the standard deviation for the Applanix phase (10 Hz) is 0.004 m while for the OL phase (1 KHz) it is 0.0069 m. When the OL tracking data is filtered with a 2^{nd} order Savitzky-Golay filter [Schafer, 2011] with 0.1 second window, which has an approximate frequency response of a 10 Hz low pass cutoff, the standard deviation of the random noise in the OL data decreased to 0.0039 m. Thus, we conclude that the OL phase, when filtered at 10 Hz, has comparable accuracy to a conventional CL receiver at high elevations and high SNR. Values of the standard deviation of the PRN12 and PRN10 phase difference filtered with cutoff frequencies from 1000 Hz to 10 Hz are shown in Figure 5.5.

Assuming the noise at 10 Hz was uncorrelated random white noise due to thermal processes and oscillator noise, we determined the low pass cutoff frequency necessary to obtain correlated values of phase from the independent measurements made from the Applanix and OL tracking receivers. To do this, the two time series were smoothed using the same window lengths and order for the Savitzky-Golay filter over a range of values from 0.2 to 20 seconds, then differenced (Figure 5.6). For a 5-second window length, the standard deviation of this difference decreased to a value of 0.0013 m compared to 0.0065 m for the unsmoothed case. Further smoothing does not decrease it significantly, therefore, assuming uncorrelated noise, a 5-second window optimally filters out the random noise. A window length of 5 seconds leads to a vertical sampling interval of 100-120 m in the height range below 8 km. This is smaller than the size of the first Fresnel zone, which is estimated geometrically to be 200-240 m [Xie et al., 2008]. Therefore, the vertical resolution of the observations is preserved when the smoothing filter is applied to reduce the random noise.

The 5-second window length was adopted for the operational processing of all the profiles. The 50 Hz OL excess phase profiles for each occultation were differentiated to produce excess Doppler profiles. The differentiation was implemented in the application of the second order Savitzky-Golay filter. The same filtering was applied to

the excess phase from the high elevation satellite, which was then subtracted from that of the occulting satellite to remove the receiver clock error.

5.4 Retrieval method

The method for retrieving atmospheric properties from spaceborne RO excess phase measurements has been described in the literature [Hajj et al., 2002; Kursinski et al., 1996]. Modifications to this basic approach have been derived for the airborne geometry [Healy et al., 2002; Lesne et al., 2002; Xie et al., 2008], which we have implemented here. The refractive bending of the raypath induces an excess Doppler shift in the carrier phase of the GPS signal, which is the fundamental observed quantity. The bending angle is calculated geometrically from the single differenced excess Doppler profile assuming a spherically symmetric atmosphere where Bougers law describes the bending of the signal raypaths [Vorobev and Krasilnikova, 1994]. The ellipticity of the atmosphere is taken into account by finding the local radius of curvature, then shifting the coordinates of the source and the receiver to positions relative to the center of curvature [Syndergaard, 1998]. The refractive index of the neutral atmosphere at L1 (1.57542 GHz) and L2 (1.22740 GHz) GPS frequencies is given by:

$$N = (n-1) \cdot 10^6 = k_1 \frac{P_d}{T} + k_2 \frac{e}{T} + k_3 \frac{e}{T^2} \tag{5.14}$$

where N is refractivity, n is the refractive index, P_d is the atmospheric pressure in hPa, T is atmospheric temperature in Kelvin, and e is water vapor partial pressure in hPa [Thayer, 1974], and the k_1, k_2 and k_3 constants are 77.6 $\frac{K}{hPa}$, 70.4 $\frac{K}{hPa}$ and $3.739 \cdot 10^5$ $\frac{K^2}{hPa}$ [Bevis et al., 1994].

The integrated bending angle, α, caused by refraction, is given by:

$$\alpha = 2 \int_{r_t}^{r_R} \frac{1}{\sqrt{n^2 r^2 - a^2}} \frac{d(\ln n)}{dr} dr + \int_{r_R}^{r_T} \frac{1}{\sqrt{n^2 r^2 - a^2}} \frac{d(\ln n)}{dr} dr \tag{5.15}$$

where r_R is the distance from the center of the Earth to the GPS receiver, and r_T is the distance to the GPS transmitter, r_t is the distance to the tangent point,

or point of closest approach to the surface, n is the refractive index, and a is the impact parameter given by $a = nr$ [Fjeldbo et al., 1971; Healy et al., 2002; Xie et al., 2008]. Unlike spaceborne RO, the airborne RO measurements must be corrected for the asymmetric sampling geometry, in other words eliminate the second term in Equation 5.15. Rays reaching the antenna from above and below the aircraft local horizon are both affected by atmospheric refractivity, however we cannot retrieve unambiguous information from the positive elevation angle rays. Therefore, we use the partial bending angle, which is the difference between the negative and positive elevation angle bending for a common impact parameter, a, as described in Healy et al. [2002] and Xie et al. [2008], which removes the second term from Equation 5.15 above. It is the accumulated bending from the tangent point to the aircraft height (Equation 5.16).

$$\alpha' = \alpha_N(a) - \alpha_P(a) = -2a \int_{n_t r_t}^{n_R r_R} \frac{d(\ln x)}{dx} \frac{dx}{\sqrt{x^2 - a^2}} \tag{5.16}$$

The bending angles near the top of the profile and the positive elevation bending angles are very noisy, which are likely the result of the random noise in the velocity estimates of the aircraft, primarily due to turbulence. Therefore we replace the observed bending angle with a simulated profile for the positive elevation angle bending and the top 1 km impact height of the negative elevation angle bending. The positive elevation bending angle was simulated for an assumed atmospheric profile above the aircraft from the CIRA-Q monthly climatology of refractivity, which is solely a function of latitude [Kirchengast et al., 1999], and is within 2 N-units of the in-situ refractivity measured at the aircraft height. The simulation numerically integrates the forward Abel integral in Equation 5.16.

The bending angle profile was interpolated at regular intervals of impact parameter. For the largest bending angles near the surface, the bending is not a single-valued function of impact parameter, because of strong gradients. For these preliminary calculations, we reduce the magnitude of the bending angle variations so that the bending is single valued, so that the inverse Abel transform can be used to retrieve

refractivity. After the interpolation to regular impact parameter intervals, the partial bending is calculated.

The refractivity profile is retrieved from the partial bending angle using the inverse Abel transform in Equation 5.17.

$$n(a) = n_R \cdot exp\Big[\frac{1}{\pi}\int_{x=a}^{n_R r_R} \frac{\alpha'(x)dx}{\sqrt{x^2 - a^2}}\Big] \tag{5.17}$$

This requires the information about the refractivity at the aircraft, The aircraft did not collect measurements of in-situ moisture, therefore we calculated N from the in-situ measurements of temperature using the first term in Equation 5.14 assuming negligible moisture at 13.5 km altitude. The integral was then carried out numerically from the observed partial bending angle profile.

5.5 Results

5.5.1 Setting occultations

Figure 5.7 shows the excess phase and Doppler profiles for the setting satellite PRN13 (black). The reference high elevation satellite is PRN02 (dark gray), and the time series of excess phase for PRN02 is used to eliminate the receiver clock errors present in the occulting satellite signal through single differencing (light gray). These common receiver clock errors are visible in the excess phase and Doppler profiles shown in Figure 5.8. The airplane heading is examined to verify that aircraft turns do not terminate the profile early by rotating the satellite azimuth out of the gain pattern of the antenna or blocking the signal with the aircraft structure (Figure 5.7, top right panel). The heading changes dramatically at 18.17 hours (top right), however, the 60-second moving average of the SNR (gray line) for PRN13 (bottom right) indicates that the signal is lost at about 18.1 hour, before this turn. The truncated excess Doppler profile (light gray line, bottom left panel) is used in the refractivity retrieval.

We calculated the bending angle profile from the PRN13-PRN02 single differenced excess Doppler profile (gray line in Figure 5.9) using the method described in the pre-

vious section. The maximum impact parameter corresponds to the ray path arriving at the receiver horizontally (0° elevation angle). For elevation angles below 0°, the bending increases rapidly as the ray descends in the atmosphere, and it reaches its maximum value just before the signal is blocked by the limb of the Earth. Near the maximum impact parameter (0° elevation angle), the Doppler shift due to the atmospheric bending is small relative to the noise level, producing very noisy and unreliable bending angle values. We simulated the negative (black line in Figure 5.9) and positive (dash-dotted line) elevation bending angles using an a priori estimate of the atmosphere from the CIRA-Q model at the latitude of the aircraft at the time of maximum impact parameter. Then, the top and the positive elevation sections of the observed bending angle profile and the negative elevation sections down to an impact height of 13.5 km are replaced with the simulated values (gray line in Figure 5.10).

The refractivity profile for the PRN13 setting occultation is retrieved from the partial bending angle, using the Abel transform, described above. The refractivity at the receiver is calculated from the in-situ temperature, which was within 1.47 N-units (less than 2.5 %) of the value from the CIRA-Q model profile assumed for the atmosphere above the flight level.

To evaluate the quality of the retrieved profiles, they were compared to the ECMWF analysis profiles. These analyses are the end product of over a year of coordinated observing, modeling and forecasting of organized tropical convection [Waliser and Moncrieff, 2007]. The model fields have approximately 25 km grid spacing, 91 vertical levels, and are available in 6-hour time windows. We chose the ECMWF analysis profile closest to the lowest tangent point location for the comparison with a given occultation, and closest in time to the time of the occultation. The refractivity was calculated from Equation 5.14 [Thayer, 1974] using the relative humidity, pressure and temperature from the ECMWF analysis profile using a variable saturation pressure [Vedel, 2001] for the conversion from relative humidity to water vapor pressure. Because ECMWF analysis uses pressure levels as a reference rather than geometric height we used a value of gravity that varies with height (*Federal Meteorological Hand-*

book No. 3, Rawinsonde and Pibal Observations. May 1997) and considered the difference between geoid height and mean sea level (http://geographiclib.sourceforge.net/cgi-bin/GeoidEval) at the location of the occultation in the transformation from vertical pressure levels to geometric height.

Figure 5.11 shows the ECMWF refractivity profile at 18Z and [Lat Lon] = [27.75 -84.75], which is closest to the lowest tangent point for the PRN13 setting occultation. Figure 5.12 shows the ECMWF temperature (black line) and dew point temperature, T_{dew}, (dashed black line) profiles, which indicate a sharp temperature inversion at 1.5 km, with an associated drop in humidity, an isolated layer of dry air at around 5 km and low humidity above 13 km. The retrieval results are compared to the reference ECMWF refractivity profile (Figure 5.13). There is a 6 % refractivity bias relative to the ECMWF analysis profile. The cause of this bias has not yet been determined. However, the general structure of the profile has been retrieved, because the standard deviation of the difference between the ECMWF and the retrieval refractivity is less than 0.75 % from 1.5 km to 11.5 km. As a guide, 0.5 % refractivity variation corresponds to 1 K temperature variation, or better than 5 % relative humidity variation below 5 km [Xie et al., 2008].

5.5.2 Rising occultations

Rising occultations pose a special challenge in both spaceborne and airborne observations since the signal power is low in the beginning, therefore the satellite cannot be acquired until it rises well above the elevation angles of interest. In this case, the signal for rising PRN22 was not acquired by the CL tracking until it had reached an elevation angle of about 10°. We processed the RF recordings using the backward OL tracking method described above. For this occultation, and for the entire data set, we achieved OL tracking Doppler profiles for rising occultations with quality comparable to or better than setting cases. Figure 5.14 shows the excess phase profiles for rising satellite PRN22 (black) and a reference high elevation satellite PRN29 (dark gray).

During this occultation the airplane heading did not vary significantly. The SNR was below the threshold at approximately 19.8 hours, which indicates the start of tracking of this rising occultation. The refractivity retrieval was carried out in the same manner as for setting occultations. Figure 5.15 shows the bending angle calculated from the differenced excess Doppler for occulting satellite PRN22 and high elevation satellite PRN29 (gray). The top and the positive elevation sections of the observed bending angle profile were replaced with the simulated values from the CIRA-Q model for the latitude of the tangent point at zero elevation angle (Figure 5.16), and the refractivity was retrieved from the calculated partial bending angle. The comparison of the retrieved refractivity with the reference ECMWF analysis profile shows a bias of 5.5 % refractivity with a standard deviation of 1.5 % from 2.6 km to the flight altitude (Figure 5.17). Once again, a large positive bias was found, but the structure of the retrieved profile was similar to the model. It is useful to describe quantitatively how well the RO observations reproduce the expected variations due to synoptic scale atmospheric variations by comparing with a climatological profile. Figure 5.18 (left) shows the temperature and dew point temperature for the CIRA-Q model and the ECMWF analysis profile at the latitude of the PRN22 tangent point. On this particular day, the ECMWF analysis profile near the PRN22 tangent point has a steep temperature inversion from 11 to 13 km height, much lower than the tropopause in the CIRA-Q climatology. In terms of refractivity (Figure 5.18, right) this produces lower than average refractivity for ECMWF analysis at 13 km (warmer temperatures) and higher than average refractivity at 1 km (colder temperatures). The observed RO profile (thick black) also has this synoptic scale signature in the tropopause with relatively low refractivity at 13 km and higher refractivity at 11 km. The ECMWF analysis profile is warmer and moister than the climatology from 4 to 9 km. By plotting the dry pressure contribution to the refractivity (Figure 5.18, right, dashed gray line) we see that it is the contribution of high moisture, in the nearly saturated profile that raises the refractivity above the climatological values in this height range. The shape of the observed refractivity profile closely mimics the height variations in

the ECMWF refractivity profile with an offset of 5 % as stated above. In spite of the bias, it is clear that the airborne RO profile is qualitatively recovering the structure of the tropopause at 11 km and the variations due to moisture from 4 to 9 km. The dry layer at 3-3.5 km altitude in the ECMWF analysis profile (decrease in T_{dew} shown by dashed black line in the left panel) is expressed as a sharp decrease in refractivity. The height of this refractivity gradient is the height at which the RO observation profile starts to decrease substantially and diverge from the ECMWF analysis profile, as was noted earlier, and we hypothesize is symptomatic of the limitations of the geometric optics inversion method. So while we know the RO profiles are unreliable below this point, we suggest that it is a reliable indicator of the height at which this sharp refractivity gradient is present. Above average moisture in the ECMWF analysis profile below 2.5 km contributes to higher than average refractivity, which is not possible to retrieve in the RO observations that stop at 2 km. This example demonstrates that synoptic scale variations in the atmospheric profile are on the order of 5 %, and that variations of this order are similarly represented in the RO profiles. This gives us confidence that the RO technique will provide useful data on synoptic scale weather systems, once the source of the 5.5 % bias is resolved.

5.6 Reliability of the OL tracking method

Nineteen occultations were predicted for the 15 February 2008 flight. We were able to retrieve profiles successfully for ten of those cases, of which five were setting and five were rising occultations. The most important factor determining the number of missed occultations was the lack of navigation data bits that are normally furnished by the global reference GPS tracking network. Missing navigation data bits and inconsistency or parity errors when decoding the navigation data bits [Beyerle et al., 2009] affected five out of nineteen occultations. However, the current global coverage of ground networks providing the navigation data has improved since 2008 and now records approximately 99 % of the available data [Zus et al., 2011]. Also, the

navigation data bits can be used from different sources in the case of erroneous subframes in the data message at one archive center (GFZ German Research Centre for Geosciences archive [Beyerle et al., 2009] and the COSMIC archive at http://cosmic-io.cosmic.ucar.edu/cdaac/index.html). Therefore, for current flights, using different sources for the navigation data bits, the number of the airborne RO profiles successfully retrieved is expected to be about 26 % greater. The second important factor decreasing the number of occultations recorded using side looking antennas was the aircraft turns, which rotated the line-of-sight out of the antenna gain pattern or blocked the signal entirely by the aircraft structure. That eliminated three rising occultation cases (PRN28, PRN21 and PRN24) and one setting occultation, PRN10. In these cases, it may be possible to retrieve lower quality data from the top antenna. For example, we were successfully able to retrieve a rising occutation profile (PRN16) on the top antenna, while this satellite was not able to be acquired in CL tracking from the port antenna, which is required to be able to align the navigation data bits to initialize OL tracking. This was due to the low SNR because of the azimuth of the PRN16 satellite relative to the peak in the RO antenna gain pattern (PRN16 in Figure 5.19). Therefore, we suggest that having the top antenna recordings as backup to the high gain RO antennas can potentially minimize the number of missed occultations during the airplane turns.

Table 5.1 summarizes the results of the retrievals for all of the OL excess phase profiles for 15 February. The occultations are ordered in latitude from north to south. For most cases the OL retrievals successfully extend to below 1 km height. An airplane turn during the PRN05 occultation truncated the profile early, however it still reached down to 2.94 km height.

We evaluate the performance of the RO antennas in terms of whether the current design limits in any way the number of occultations that are recovered because of limitations in the signal to noise ratio (SNR). To do this, we examine the amplitude profiles for the PRN12 high elevation satellite recorded through the top and port antennas at the same time. Figure 5.20 shows the amplitude profiles (black lines

in top and middle panel) for both antennas as well as the satellite's elevation angle during the occultation period (dashed gray lines). The azimuth of the satellite varies from $+28^\circ$ to $+15^\circ$ ahead of the port direction. The SNR from the side looking RO antenna consistently increases with the descent of the satellite, however, the airplane turn that occurs 19 UTC degrades the SNR on the port antenna, while the measurements on the top antenna are unaffected. When the satellite is below 10° elevation (Figure 5.21), the SNR for the RO antenna is approximately 10 dB larger on the port antenna compared to the top antenna. This is consistent with the design of the high-gain, narrow field of view RO antennas that have a gain pattern focused toward the horizon. The residual phase profiles for top and port antenna recordings both show a cycle slip at 19.3 and 19.9 decimal hours respectively but agree very well otherwise (Figure 5.22).

Figure 5.19 shows the azimuth of the recorded occultations relative to the aircraft heading. We found that the antenna gain pattern was sufficient for tracking all signals, and there were no missed occultations because of the flight direction. There was no evidence in the side-looking antenna signal of local multipath interference from the aircraft structure in the SNR observations. The antenna gain pattern is symmetric above and below the horizon. We can see from the SNR for PRN12 setting satellite that the gain remains high at $+5^\circ$ elevation, so this shows that the antenna gain pattern is not limiting recording of low SNR signals below the horizon at -5° elevation. The drops in the SNR (Figure 5.20) are due to attenuation, defocussing, and fading effects of the atmosphere and not due to passing out of the antenna gain pattern. The peak gain of the antenna is 9.4 dB, compared to 12 dB for the COSMIC RO antennas. We see that there are significant SNR fluctuations starting when the satellite is as high as 20° above the horizon, so that the aperture of the antenna gain pattern of 18° is close to optimal, and cannot be significantly decreased for the benefit of increasing the gain at the horizon.

5.7 Discussion

5.7.1 Potential sources of retrieval bias

While the observed excess Doppler profiles are clearly measuring properties specific to the local atmosphere, the large biases currently limit their expected impact in data assimilation. Results from airborne balloon occultation measurements in the Antarctic made with a conventional receiver that use similar analysis methods did not show these large biases [Haase et al., 2012]. Preliminary results from a subsequent flight campaign in the tropics with the same instrumentation and analysis techniques produced only one profile out of 9 with a bias greater than 4 %. So far the bias has appeared mainly in the observations made at intermediate latitudes.

One potential source of bias in the retrieved refractivity is a bias in the excess Doppler profiles. The largest error source above 5 km altitude is the navigation velocity error. It has been found Muradyan et al. [2010] that random 5 mm/s errors in the velocity determined from the GISMOS GPS/INS navigation system produce less than 0.2 % refractivity errors up to flight altitude. For a 4 mm/s bias in velocity, a bias of up to 0.5 % was produced in the refractivity. Most of the profiles do indeed have a non-zero mean Doppler prior to the beginning of the occultations. However, these are not large enough to produce 5 % bias in refractivity, and there is no systematic relationship between the size of the mean Doppler and the refractivity bias.

We have also investigated other possible sources of the bias, such as errors in the refractivity at the receiver, and in the assumptions about the refractivity profile above the flight level. The refractivity at the receiver location, which is required in the calculation of the bending angle from the excess Doppler as well as in the Abel inversion of the partial bending angle, is calculated from the in-situ temperature measurements. These are within 0.3-1.7 N-units of the values from the CIRA-Q atmospheric model profile, which was assumed for above the aircraft height in the retrieval. We investigate the sensitivity of our results to this error by introducing an error of ± 2 N-units into the in-situ refractivity value at the receiver height (N_{rec})

(Figure 5.23) for the PRN13 setting occultation. The black line shows the original percent difference between the retrieved and reference ECMWF refractivity profiles without any introduced errors. The blue and red lines represent the retrievals using values for N_{rec} that are 2 N-units higher and lower, respectively. Thus, 3.4 % errors in the in-situ refractivity values can greatly affect the retrieval by introducing a bias that is increasing with height. However, smaller values of 0.3 to 1.7 N-units observed for other retrieval cases have little effect. In addition, the bias for the retrieved profiles is typically increasing as height decreases, which makes this source for the bias unlikely.

Throughout this study, we have replaced the positive elevation bending angles, as well as negative elevation bending angle extending 1 km below the maximum to the maximum impact height, with the simulated bending angle from an assumed climatological atmospheric profile above the aircraft. The effects of the assumptions about the refractivity above the aircraft height are shown for the retrieval for the PRN12 setting occultation, which has a larger offset between the observed and the climatological simulated bending angle profiles 1 km below the top. We retrieve a preliminary estimate of the refractivity profile from the entire observed PRN12 bending angle profile, including positive and negative elevation angles. Then we make a Fourier fit [Yang et al., 2005] to this refractivity profile from the surface to the aircraft height. This is used to create a simulated bending angle profile, which then is used to replace the top and the positive elevation bending angles of the observed bending angle profile. Figure 5.24 shows the percent difference of the retrieved refractivity for the two cases relative to the reference ECMWF analysis profile. The retrieval that assumed the CIRA-Q model above the aircraft height is shown with the black line, and the retrieval that assumed the Fourier fit to the PRN12 preliminary refractivity profile is shown in the red line. This introduces a small improvement of 0.8 % refractivity from 6 to 11 km altitude. Note that neither the Fourier fit nor the CIRA-Q a priori model had a tropopause. This remains to be investigated, whether the lack of a tropopause in the assumed model just below flight level could in fact be causing the bias at lower levels.

Thus, while both variations in the in-situ refractivity at the receiver and the profile above the aircraft height need to be carefully taken into account for improving the estimate of the airborne RO accuracy, neither of these effects is large enough to produce a 5 % bias throughout the height of the profile.

Several other factors might be potential sources of a bias. The measurements are currently not corrected for the effects of the ionosphere, because OL tracking has only been implemented for L1. OL tracking for L2C is currently under development, however it will only be possible on the subset of satellites transmitting on L2C. In spaceborne RO, the ionospheric contribution is eliminated by using a combination of L1 and L2 bending angles at a common impact parameter [Vorobev and Krasilnikova, 1994] at altitudes above 10 km. An ionospheric correction term is then extrapolated below that height [Syndergaard, 2000]. A similar technique could be used to extrapolate ionospheric correction terms from the CL tracking data at higher elevations.

Finally, there is a possibility of an unmodeled geometric effect, unmodeled antenna phase pattern variations, propagation effects through the window of the aircraft, or unmodeled delays in the RF path within the receiver or transmitter system. Most of these are not effects where the phase would increase significantly at greater depth in the atmosphere, so would not be an obvious source of a relatively constant bias in refractivity with height. These possible sources are under further investigation.

The current procedure of handling multivalued bending angles for a single impact parameter involves a linear interpolation when calculating the partial bending angle. This could possibly introduce a bias, therefore a better method for dealing with multivalued bending angles needs to be developed.

The refractivity retrieval clearly diverges from the model analyses below about 4 km depth. This is also approximately the height level where there are large variations in the OL residual phase and amplitude, and the retrieval of bending angle from Doppler begins to produce large fluctuations in bending that result in a multivalued function of impact parameter as seen in Figure 5.10. Simple methods for interpolating the bending angle profiles allowed us to carry out preliminary retrievals that illustrate

the potential depth of the sampling of the profiles, and also provide some indication of sensitivity to the height level of significant changes in refractivity. However, the assumptions of geometrical optics clearly do not hold. We are currently investigating methods for radioholographic inversion techniques such as Full Spectrum Inversion (FSI) [Jensen et al., 2003] for the derivation of bending angle from the amplitude and phase of the OL tracking signals. This requires a significant development effort as FSI assumes a circular geometry for the source and receiver trajectories. This is expected to provide better retrievals below 4 km in the future.

We can also potentially make an improvement to the excess Doppler results from the OL tracking by incorporating an estimate of the excess Doppler due to a climatological model of the atmosphere into the Doppler prediction. The OL tracking method does not rely on any feedback mechanism to track the code delay, but is solely based on a pre-computed Doppler frequency model. In the current implementation, the pre-computed Doppler frequency has only considered the geometric Doppler due to the relative motion of the transmitter and receiver. Previous work has shown [Sokolovskiy, 2001] that as long as the model Doppler is within approximately 10-20 Hz of the actual Doppler, the extracted phase measurements are valid. While the transmitting satellite is at relatively high elevation, the excess phase contribution from the atmosphere is small. However, at low elevation angles, the contribution from the atmosphere reaches 0.6 m/s or about 3 Hz. With the very rapid fluctuations in phase seen in the data at low elevation angles, it is possible that the 10-20 Hz range is exceeded, or at least the SNR is reduced, which may lead to poorer results. Therefore, some improvement in the results may be expected when a more advanced Doppler prediction is implemented, such as incorporating raytracing results from the CIRA-Q climatological model, which may lead to a closer agreement in the height range below 4 km.

5.8 Future perspectives for NWP

Given that we have shown consistent success in extracting excess phase with the OL software receiver tracking to low altitudes, one can consider the potential contribution the airborne RO system could make in the future to NWP. The amplitude and phase profiles that have been retrieved are consistent in quality with the COSMIC data. The airborne RO profiles could be extended to lower altitudes if FSI is implemented using the airborne RO measurements of phase and amplitude directly, as is currently done with COSMIC data. The spaceborne RO profiles from the OL signals penetrate well below the sharp top of the atmospheric boundary layer up to the Earths surface. Even using the Full Spectrum Inversion Technique, however, the spaceborne RO profiles have a negative bias of 1-1.5 % with respect to ECMWF below 2 km altitude, and with a standard deviation of 2-2.2 % below 5 km altitude [Gorbunov and Shmakov, 2011], so there is progress to be made for both systems. Assuming that FSI is implemented, the airborne system has two prospective contributions to make: 1) the capability to provide high vertical and temporal resolution profiles for targeted missions and 2) development into an operational system on commercial aircraft.

For targeted missions, the airborne RO profiles can be valuable as a complement to the existing COSMIC profiles which are rather sparse both temporally and spatially. During the same 5-hour time period of the 15 February flight, COSMIC provides only 5 occultations within 700-800 km of the flight path. Case studies have tested spaceborne GPS RO data assimilation for the purpose of improving forecasting of tropical cyclones [Huang et al., 2010]. One GPS RO profile was available within the 6-hour assimilation window within 1000 km of tropical cyclone Gonu in 2007. Three profiles were within 1000 km of typhoon Nargus in 2008. There was improvement of the storm track for Gonu, but not for Nargus. Clearly much improvement could be made with airborne observations in the vicinity of this type of storm where on the order of 10-14 profiles could be provided in the same time window within 250 km of the target. Both spaceborne and airborne RO have similar horizontal averaging kernels for each

observation height with a larger tangent point drift in case of airborne RO. However, operational centers have already implemented assimilation of the observations at each height at different locations based on the tangent point drift, so this is no longer an issue.

Regarding operational systems on commercial aircraft, Lesne et al. [2002] showed that 225 occultations in the North Atlantic flight corridor would be provided by 14 aircraft in one day. This would be a significant supplement to the 48 occultations provided by COSMIC in the same area. Several implementation issues would need to be resolved, principally dealing with real time communication for the data to and from the aircraft. The advantages of on-board processing would increase the requirements for data transmission to the on-board system (precise orbits, global tracking data), but decrease the requirements for data transmissions from the system. Efforts to miniaturize the recording system and streamline data processing are important to support this. The particular example of the North Atlantic is of high potential impact because the improvements in NWP forecasting due to the increase in data collection would directly benefit flight safety. Therefore, looking forward, if the current biases in the airborne RO are resolved, this dataset, with similar quality to spaceborne data, can play an important role in NWP forecast improvements in the troposphere.

5.9 Conclusions

For a 5-hour flight at 13.5 km altitude on 15 February 2008, 19 rising and setting occultations occurred. We have successfully retrieved the excess phase and amplitude profiles using the OL tracking method for 5 setting and 5 rising occultations. The rising occultations are processed and refractivity is retrieved with comparable quality for both rising and setting occultations. The most important reason for the missed occultations (five profiles) was the lack or the poor quality of the navigation data bits necessary for the OL processing. Three occultations were lost due to aircraft turns during the occultation. Since 2008, the global network providing data bits has

improved significantly, so that from a practical point of view the same airborne RO system deployed today on a straight flight path would achieve 2.9 occultations per hour of flight time.

The OL tracking software receiver consistently recovers data below 1 km in the atmosphere (6 out of 10 profiles), with one profile reaching as low as 0.562 km in the atmosphere, even in the presence of sharp inversions at the atmospheric boundary layer. We were consistently able to retrieve bending angle and refractivity profiles from the excess Doppler down to 0.5-3 km. Currently, the bending angle profiles have been shown to be biased relative to ECMWF analysis profiles. This bias can be as great as 5-6 % of the refractivity relative to the values from the ECMWF analysis profiles, over the height range from 4 km to flight altitude. This bias is present in the profiles retrieved from conventional receiver observations as well as in profiles retrieved from the OL tracking. The standard deviation of the difference between the retrieved and reference ECMWF refractivity profiles is 0.75 % for setting satellite PRN13 and 1.5 % for rising satellite PRN22, indicating that once a solution for removing the bias is found, the quality will be sufficient for NWP assimilation. Indeed, when the vertical structure of the airborne profiles are compared with the ECMWF analysis profiles, it is clear that the airborne measurements are recovering the tropopause reliably, and that the height levels of sharp refractivity gradients are being recovered.

The retrieved refractivity decreases greatly relative to ECMWF analysis below 4 km. However, this is due to the limitations of the geometric optics Abel inversion. This was also a problem for spaceborne RO prior to the development of techniques such as FSI for dealing with multipath propagation in the lower atmosphere due to strong moisture gradients. A significant development effort is required to implement more advanced inversion techniques such as Full Spectrum Inversion, for the airborne case because of the geometry, but this effort is underway.

Large observation errors are typically assigned to spaceborne RO data during assimilation below 5 km altitude [Beyerle et al., 2004]. This is because even using the

Full Spectrum Inversion technique, the spaceborne RO profiles have an unresolved negative bias of 1-1.5 % with respect to ECMWF analysis below 2 km altitude [Gorbunov and Shmakov, 2011]. There are many questions as to the source of this bias, however it is difficult to study because the spaceborne receivers cannot transmit the entire data stream. The full signal recorded by the airborne system could provide a valuable resource for investigating biases in the lower troposphere. This quantitative analysis of the airborne RO capabilities suggests that the measurements can potentially make a valuable contribution to regional NWP in the future. What is learned from the analysis of radio occultation data about signal tracking and retrieval in the lower parts of the atmosphere will benefit the larger community, as these aspects are problematic in the spaceborne RO measurements as well.

Table 5.1: Lowest satellite elevations and corresponding atmospheric heights the retrieved refractivity profiles reach to. The occultations in the table are in descending order in latitude (from north to south).

PRN	Time (GPS sec)	Lat	Setting/ Rising	Port/ Starboard	Elevation (deg)	Geometric heigh (km)
16	501519	34.37	Rising	Top	-5	1.14
30	504271	34.22	Setting	Port	-4.46	0.25
29	490077	33.35	Rising	Starboard	-4.41	0.46
05	502656	32.23	Setting	Port	-3.83	2.94
12	502021	31.42	Setting	Port	-3.87	2.75
22	503262	31.055	Rising	Port	-4.06	1.72
13	494695	25.11	Setting	Port	-4.44	0.63
09	494695	25.1	Setting	Starboard	-4.33	0.89
26	492101	25.07	Rising	Port	-4.19	0.87
15	492410	24.81	Rising	Port	-3.78	3.34

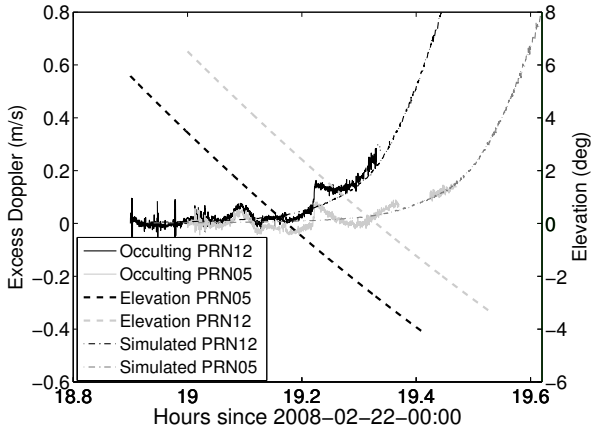

Figure 5.1.: Excess Doppler for setting satellites PRN12 (black) and PRN05 (gray) recorded by a conventional phase lock loop receiver on February 22, 2008. Black and gray dash-dotted lines show the expected increase in the excess Doppler, based on a nearby radiosonde station profile at Birmingham (BMX) at 00Z.

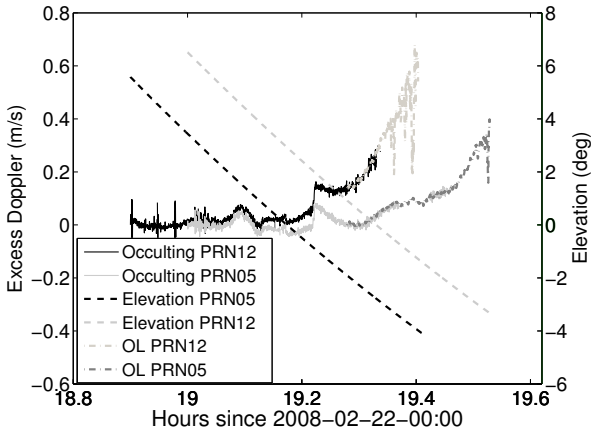

Figure 5.2.: Open-loop tracking estimates of the excess Doppler profile for PRN12 (light gray dash-dotted line) and PRN05 (dark gray dash-dotted line) continuing for a longer time period corresponding to lower atmospheric heights. The PRN12 and PRN05 elevation angles during the tracking are shown in dashed black and gray lines respectively.

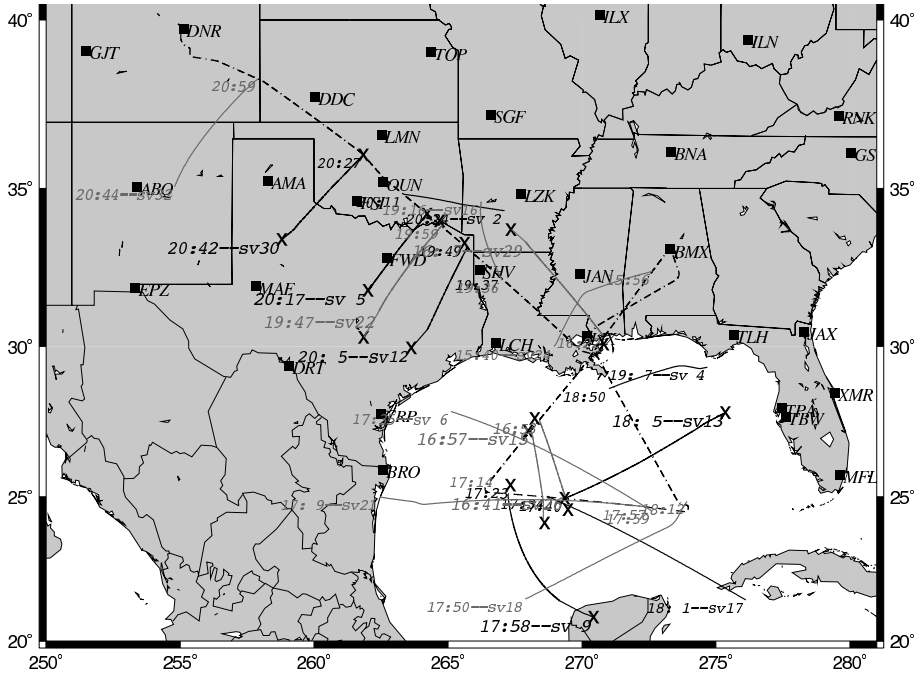

Figure 5.3.: Research flight on 15 February 2008. 7 setting and 12 rising occultations were predicted for the 5-hour flight. Black dot-dash line represents the flight path. The gray and black lines show the tangent point locations for the rising and setting occultations respectively. The numbers in the beginning and at the end of these lines indicate the start and the end time of each occultation. The crosses denote the ECMWF analysis profile locations.

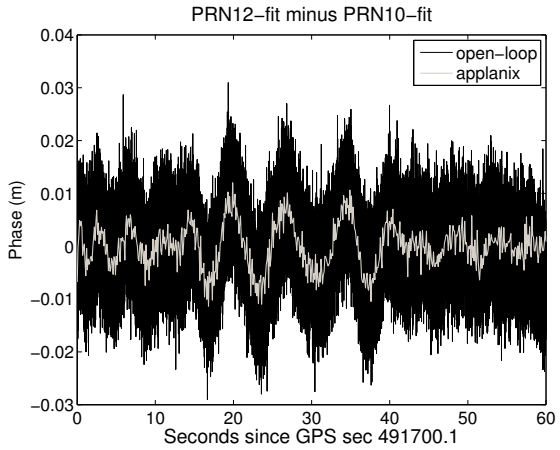

Figure 5.4.: Phase difference (L1) between high elevation PRN12 and PRN10 satellites recorded on top antenna with the Applanix receiver (gray) and the GRS (black).

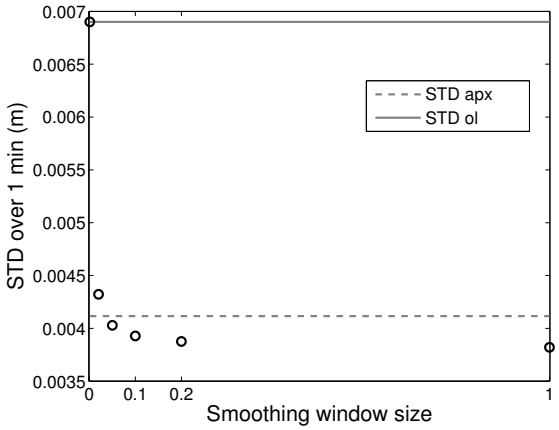

Figure 5.5.: Standard deviation of the OL phase applying different smoothing window sizes. The dashed line shows the standard deviation of the 1-minute Applanix time series, while the solid line shows the standard deviation of the non-smoothed 1-minute time series from the GRS.

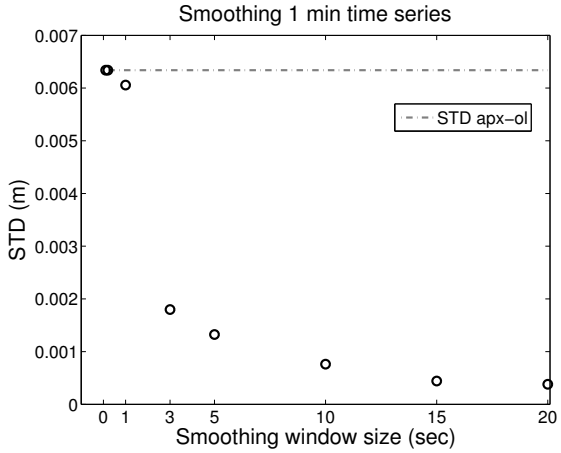

Figure 5.6.: Standard deviation of the difference of Applanix and OL phase profiles applying different smoothing window sizes. The dashed line is for the standard deviation of the difference before applying any smoothing. The phase profile in both cases is the PRN12 and PRN10 high elevation satellite phase difference.

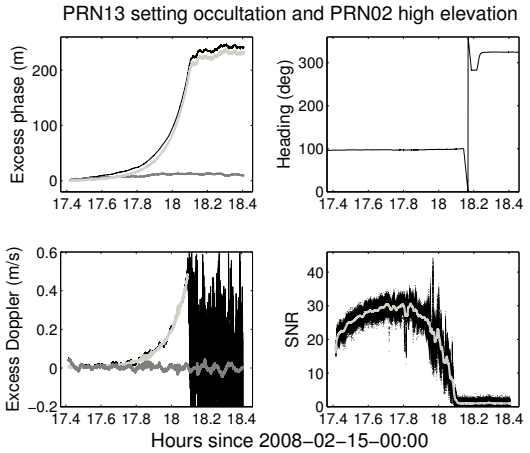

Figure 5.7.: Excess phase (top left) and excess Doppler (bottom left) profiles for setting PRN13 (black line) and high elevation PRN02 (dark gray line) satellites and their difference (light gray line). Airplane heading changes dramatically at 18.17 (top right), however, the amplitude for PRN13 (bottom right) indicates that the signal is lost before the airplane turn.

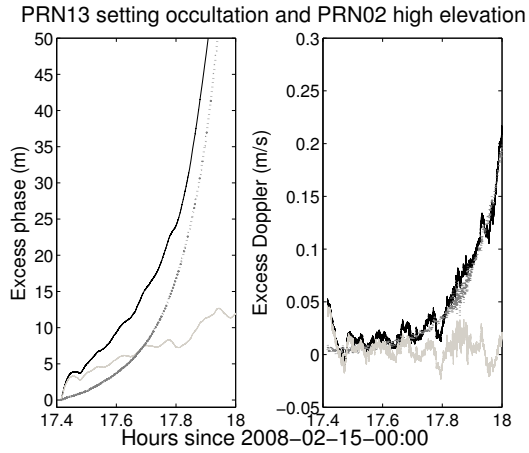

Figure 5.8.: Excess phase (left) and excess Doppler (right) profiles for setting satellite PRN13 (black line) and high elevation satellite PRN02 (gray line) satellites. The difference of the PRN13 and PRN02 excess phase and excess Doppler (dotted gray lines) illustrate the removal of the correlated clock error.

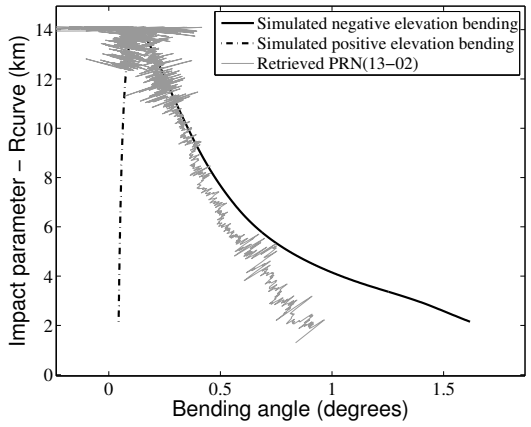

Figure 5.9.: Simulated negative (solid black line) and positive elevation bending angles (dashed line) using the CIRA-Q climatological profile at the location of the aircraft at the maximum impact height for PRN13 occultation. The gray line shows the bending angle profile calculated from the PRN13-PRN02 excess Doppler difference.

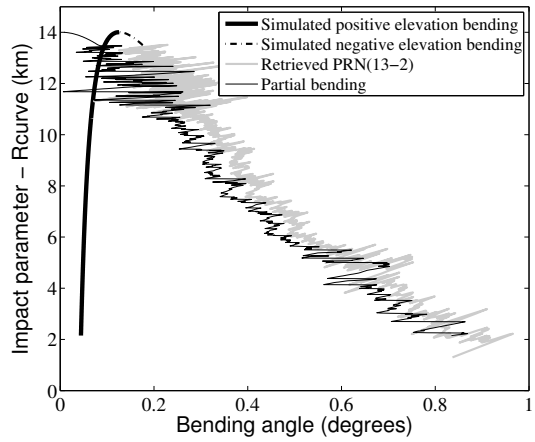

Figure 5.10.: Due to the high numerical noise at the greatest impact parameter, the top of the retrieved bending angle profile and the positive bending angle are replaced with simulated values from the CIRA-Q . The partial bending angle (thin black line) is calculated from these new negative and positive elevation bending angles.

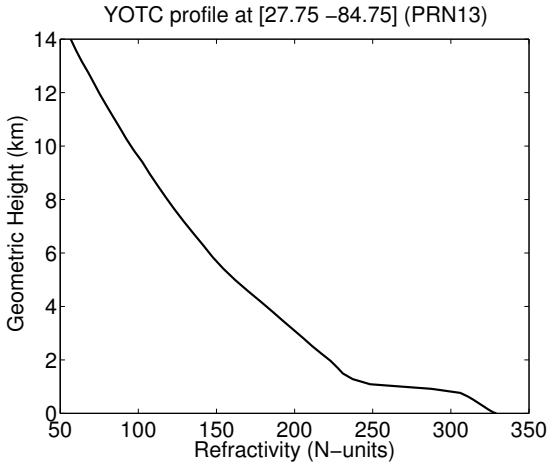

Figure 5.11.: Refractivity calculated from the ECMWF analysis profile at 18Z and at [Lat Lon] = [27.75 -84.75].

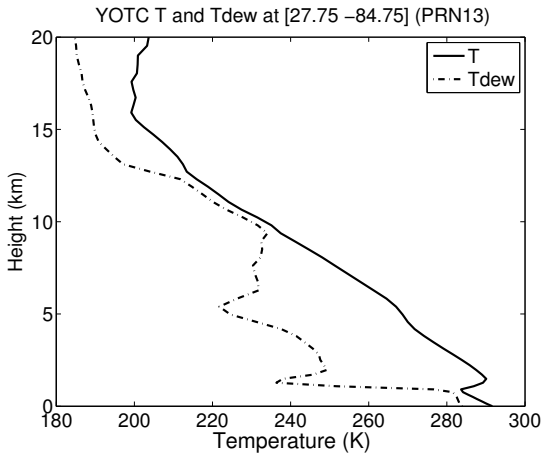

Figure 5.12.: Temperature (solid line) and dew point temperature (dashed line) calculated from the ECMWF analysis profile at 18Z and at [Lat Lon] = [27.75 -84.75].

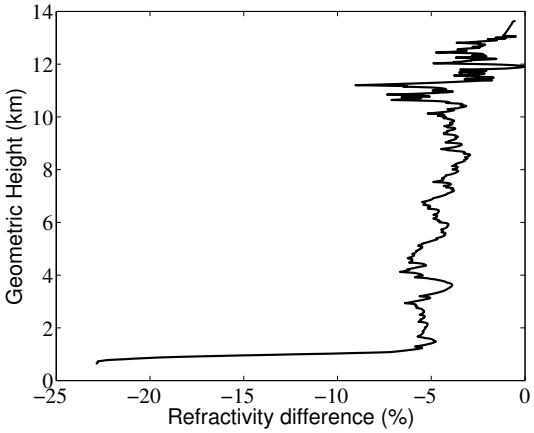

Figure 5.13.: The percent difference of the reference ECMWF analysis and the retrieved profiles for PRN13 occultation.

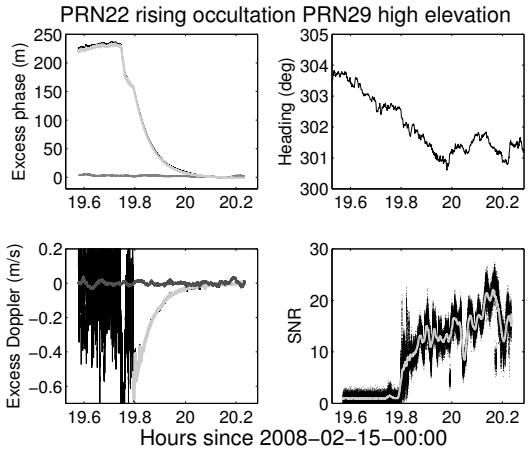

Figure 5.14.: Excess phase (top left) and excess Doppler (bottom left) profiles for rising PRN22 (black line) and high elevation PRN29 (blue line) satellites and their difference (red line). Airplane heading does not experience large variations over the occultation period. The 60-second moving average of the SNR indicates that this rising occultation was acquired at 19.8 hour.

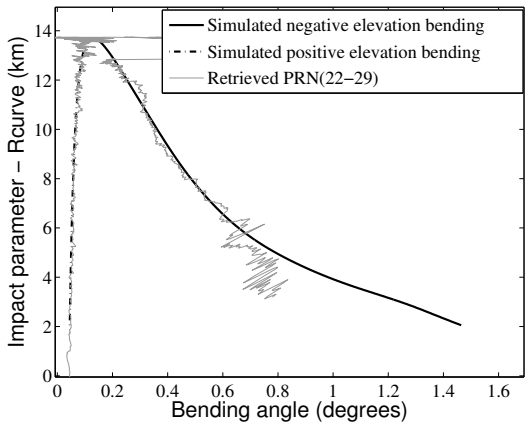

Figure 5.15.: Simulated negative (solid black line on the left) and positive elevation bending angles (dashed line) using the CIRA-Q climatological profile at the location of the aircraft at the maximum impact height for PRN22 occultation. The gray line shows the bending angle profile calculated from PRN22-PRN29 excess Doppler difference.

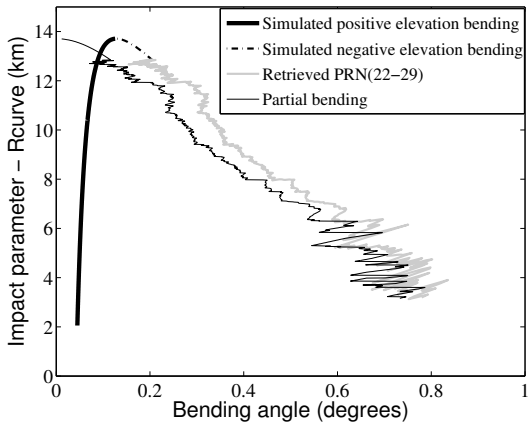

Figure 5.16.: The top of the retrieved bending angle profile is replaced by the simulation using the CIRA-Q profile.

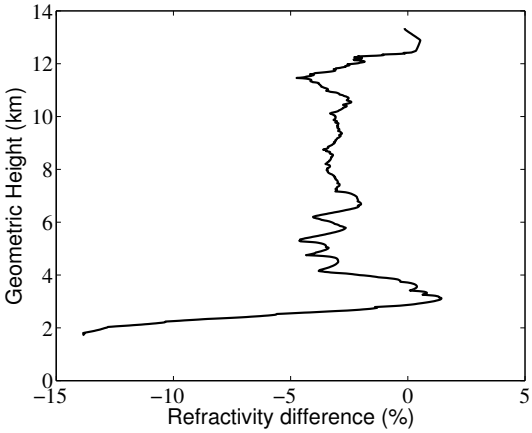

Figure 5.17.: The percent difference of the reference ECMWF analysis and the retrieved profiles for PRN22 occultation.

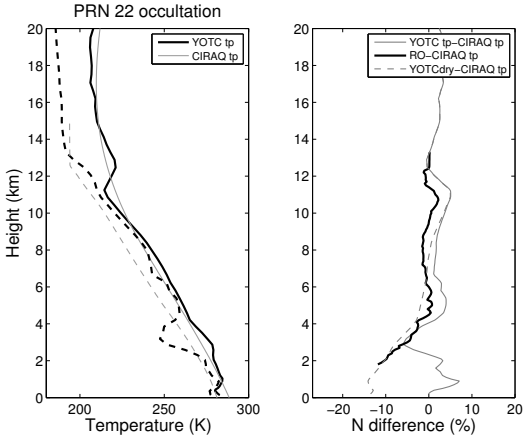

Figure 5.18.: (Left) T and T_{dew} (black solid and dashed lines respectively) from ECMWF analysis profile at 18Z and [Lat lon] = [34.00 -95.25] near the tangent point of the PRN22 rising occultation. T and T_{dew} for CIRA-Q climatological profile at the tangent point latitude of 34° are shown in thin gray solid and dashed lines. (Right) Black line shows the difference of the observed RO profile and the CIRA-Q profile at the tangent point latitude, while the difference of ECMWF and the CIRA-Q profiles at the tangent point latitude is shown in thin gray line. The dashed gray line shows the difference of the dry component in the ECMWF refractivity and the CIRA-Q profile at 34° latitude.

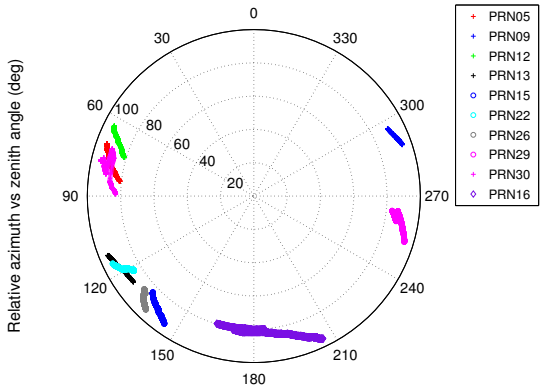

Figure 5.19.: Relative azimuth for February 15 2008 occultations vs. zenith angle.

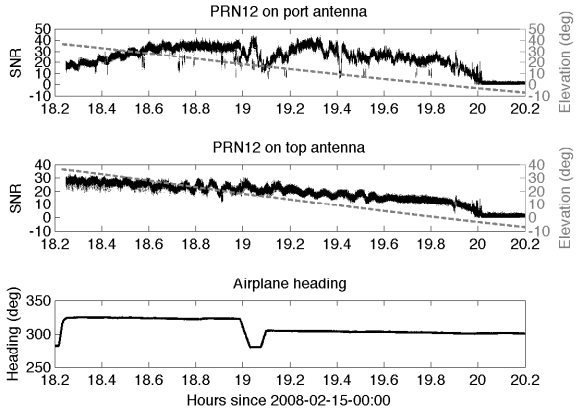

Figure 5.20.: The SNR for PRN12 on port (first panel) and top (second panel) antennas are shown in black lines. The elevation of PRN12 during the tracking period is illustrated in dashed gray line. The airplane heading is shown in the third panel.

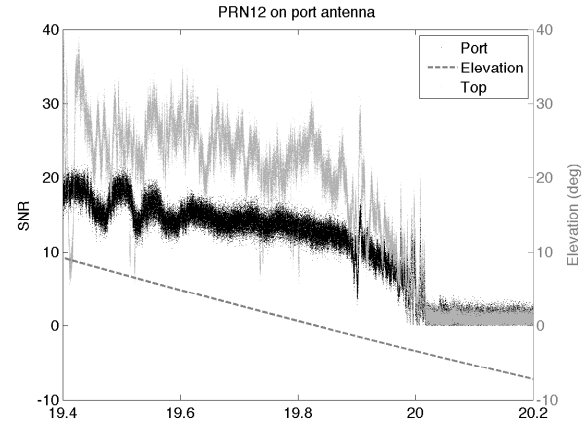

Figure 5.21.: The SNR for PRN12 on top (black) and port (gray) antennas during [19.4 20.2] time window, when the satellite elevation (gray dashed line) is less than 10°.

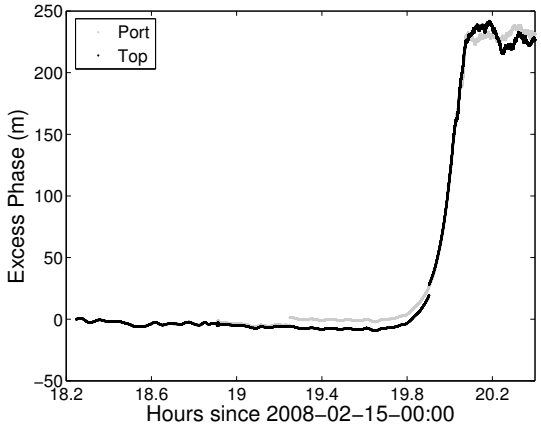

Figure 5.22.: The excess phase for PRN12 on top (black) and port (gray) antennas.

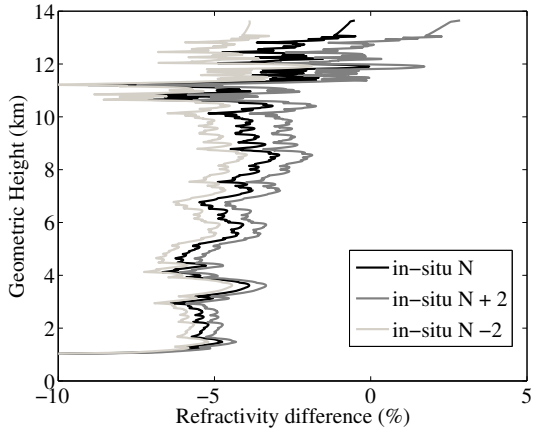

Figure 5.23.: The percent difference of the retrieved and the reference ECMWF analysis refractivity profiles for PRN13 setting satellite (black line). Light and dark gray lines show the retrieval cases when +/- 2 N-units error is added to the in-situ refractivity measurement.

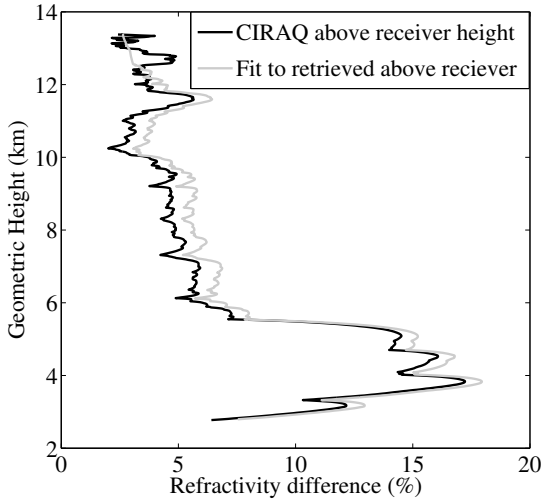

Figure 5.24.: The percent difference of the retrieved and the reference ECMWF analysis refractivity profiles for PRN12 setting occultation. The black line corresponds to retrieval case assuming a simulated refractivity above the aircraft height using the CIRA-Q climatological profile. The gray line illustrates the case when a Fourier fit to the PRN12 retrieved refractivity is used above the aircraft height.

6. ACCURACY OF AIRBORNE RO PROFILES BASED ON INDEPENDENT MEASUREMENTS

The accuracy of the airborne RO measurements and their utility for assimilation into NWP models can be assessed through comparisons with independent datasets. The accuracy requirement, for example, for the Global Navigation Satellite System receiver for Atmospheric Sounding (GRAS) RO sounder is 0.5-3 K in temperature and 5 % relative humidity [Luntama et al., 2008]. As a reference, 1 K temperature error corresponds to 0.5 % [Xie et al., 2008]. To estimate the accuracy of the airborne RO measurements, we consider the retrieved refractivity profiles in comparison with a refractivity profile calculated from a radiosonde sounding, as well as comparison with a co-located spaceborne RO profile. If the accuracy of the retrieved profiles from airborne RO measurements can be shown to be comparable to the GRAS accuracy requirement, then the airborne RO measurements are likely to have an impact in improving forecasts of severe weather events such as hurricanes, where supplementary humidity observations can play a critical role.

6.1 Comparison of the retrieved and radiosonde refractivity profiles

Radiosonde soundings are a valuable and trusted source of upper air data by the meteorological community. Therefore, comparison of the airborne RO retrieved profiles against this standard will provide a convincing assessment familiar to the NWP community. During the February 2008 flight campaign, radiosonde profiles from 28 supplementary launches were acquired in addition to the operational radiosonde launches at 00:00 and 12:00 UTC to validate the airborne RO retrieved profiles. For this purpose, we choose the closest possible radiosonde site to the occultation location having also the minimal temporal separation. We consider the PRN12 setting satellite

on February 22 2008. The PRN05 satellite is chosen as the reference satellite for the same time period to eliminate the receiver clock error common to both profiles, however care must be taken because the PRN05 satellite occults at the end of tracking period as well. Both these occultations take place in the same area as shown in Figure 6.1, therefore sampling similar atmospheric conditions. As reference, we use the Birmingham (BMX) radiosonde station in Alabama, for which high-resolution atmospheric profiles were acquired at 00Z on 23 February 2008, which is the closest launch time to the occultation time window of [19:00 19:30].

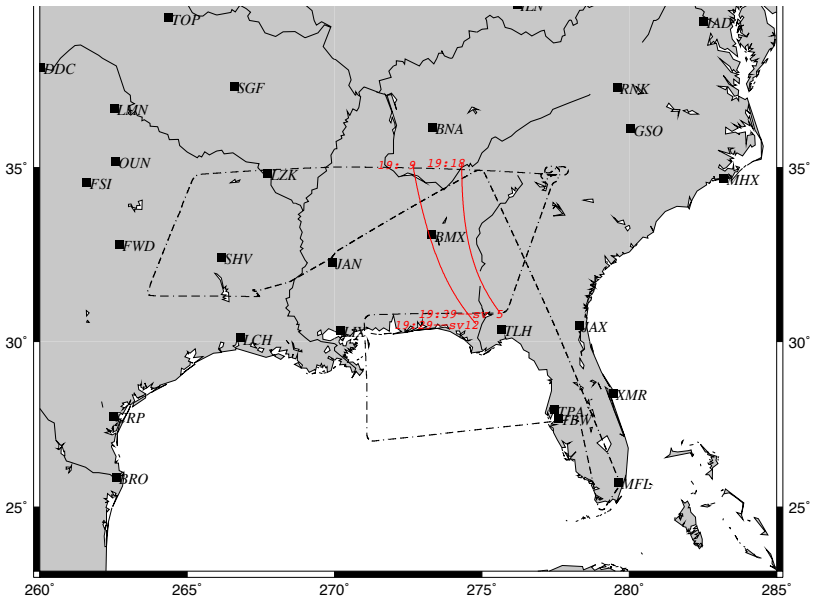

Figure 6.1.: Flight map for February 22 2008 along with PRN05 and PRN12 occultation tangent point locations shown in red. Black squares denote the radiosonde locations.

A refractivity profile is calculated from the BMX temperature and relative humidity profiles according to the method described in Section 4.2. The temperature and dew point temperate from the BMX sounding are shown in Figure 6.2 (left). From this figure a sharp temperature inversion can be noted at approximately 2 km. The air is saturated from 6 to 7.5 km, which is followed by dry atmospheric layers at

about 11 km altitude and above. The refractivity profile shown in the right panel of Figure 6.2 has its maximum at the surface, and as the atmospheric density decreases with height, the refractivity decreases as well.

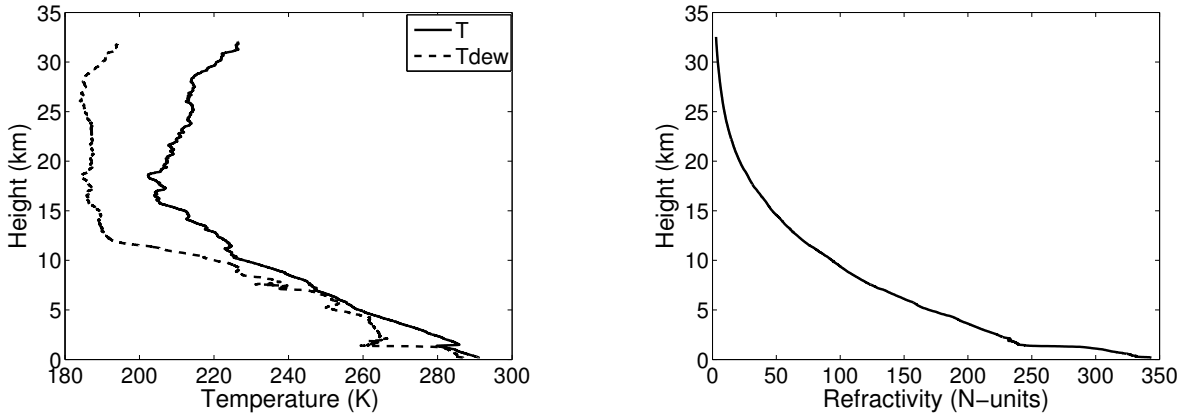

Figure 6.2.: Temperature (solid line) and dew point temperature (dotted line) profiles at 00Z on February 23, 2008 from station BMX (left). Refractivity profile derived from BMX radiosonde station measurements at 00Z on February 23, 2008 (right).

Since PRN05 is not a high elevation satellite, the single difference between PRN12 and PRN05 profiles not only removes the common clock errors, but also removes a significant amount of excess phase due to the atmosphere for PRN05. Therefore, we simulate the PRN05 GPS signal through the given model atmospheric refractivity field using a ray-tracing method, in which an initial elevation angle is specified and a search for correct ray paths from the specified GPS and airplane positions is performed. This simulated atmospheric delay is then added back to the difference of PRN12 and PRN05. Assuming the PRN05 simulation is close enough to the truth, we will be able to retrieve reliable profiles from the much larger excess phase signal due to the PRN12 occultation. Figure 6.4 (left) shows the simulated excess Doppler profiles as a function of time for PRN12 and PRN05 in blue and red dashed lines respectively. Both of these simulated profiles increase rapidly from hour 19.25 following the trend seen in the observations. The difference between the PRN12 and PRN05 excess Doppler

profiles (right) is already free of clock drift. The difference profile from the airborne RO observations is offset with respect to the simulated difference, and this offset increases with time leading to a difference of 0.072 m/s at the end of the occultation.

The corresponding bending angle profile derived from the excess Doppler [Vorobev and Krasilnikova, 1994] is illustrated in Figure 6.5. The maximum impact parameter nr corresponds to the ray path arriving at the receiver horizontally (0°). For elevation angles bellow 0°, the bending increases rapidly with the descent of the ray reaching its maximum just before the signal is blocked by the limb of the Earth at $-3.89°$ elevation angle below the local horizon. The top 1 km impact height for negative elevation angles and the positive elevation bending are replaced with the simulated profile using the BMX 00Z radiosonde sounding (Figure 6.5. The partial bending angle is then calculated (shown in black line). A refractivity profile is retrieved from the resulting partial bending angle, and this is compared to the BMX refractivity profile. This comparison (Figure 6.6) shows that the airborne RO observations are biased with respect to the radiosonde profile, with a standard deviation of about 2.3 % from 5 km to 12 km. Although we are able to retrieve airborne RO measurements in OL mode, below this height the geometric optics approximation does not work well. The effect of the multipath is evident in the bending angle profile (Figure 6.5) below 6 km impact height, where the same bending angle value corresponds to multiple impact heights.

In spite of the bias, there is a correlation in the vertical structure of the airborne RO observations and the radiosonde profile. The saturated layer of air seen in Figure 6.2 from 6 km to 7 km corresponds to a slope change in the negative elevation bending angle from 7 km and 8 km impact height. Also, the change of slope in the bending angle at approximately 11 km impact height corresponds to the drying of the atmospheric layers above $9.5 - 10$ km altitude. Therefore, once the source of the bias in the retrieved refractivity is found, we will be able to perform comparisons for the absolute accuracy of the airborne RO measurements, which demonstrate the po-

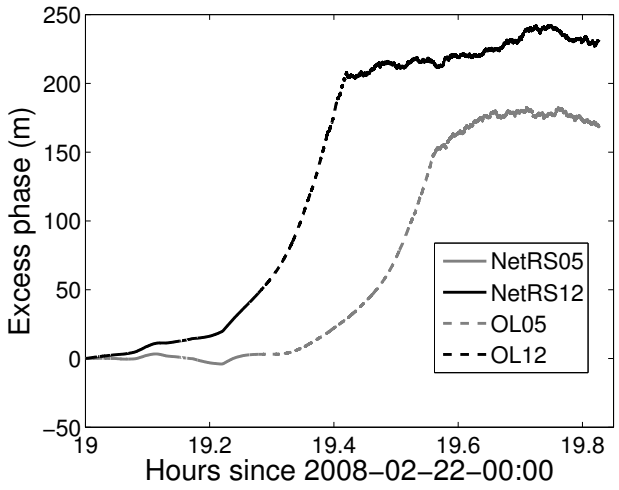

Figure 6.3.: PRN12 and PRN05 excess phase profiles on February 22, 2008 combined from NetRS and GRS measurements.

tential of capturing information on the layered structure of the atmospheric moisture field.

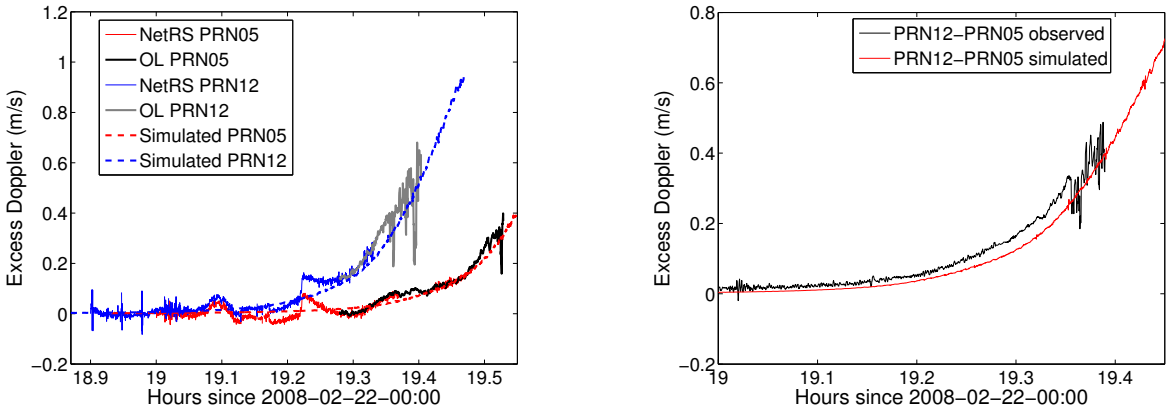

Figure 6.4.: PRN12 and PRN05 excess Doppler profiles on February 22, 2008 combined from NetRS and GRS measurements. The simulated PRN05 and PRN12 profiles are shown in red and blue respectively (left). PRN12 and PRN05 difference is shown in black (right) for the airborne observations and in red for simulations.

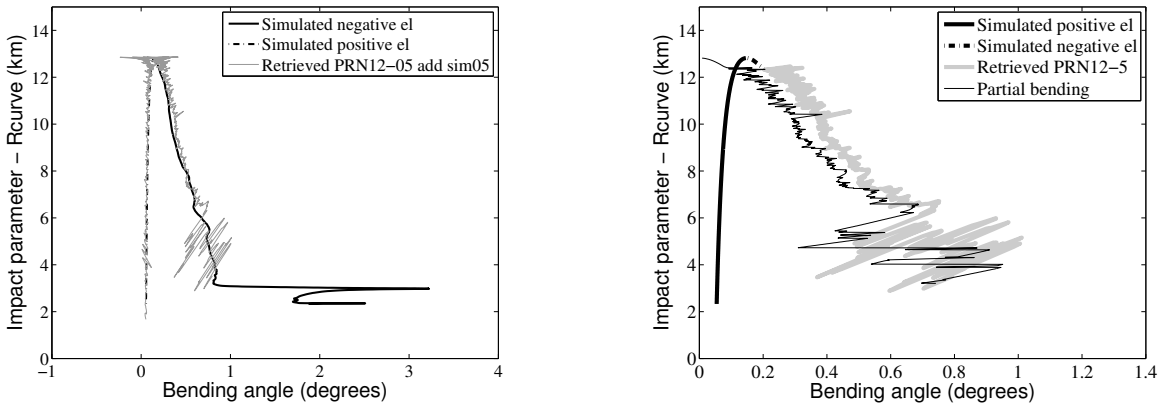

Figure 6.5.: Bending angle calculated from PRN12 and PRN05 excess Doppler difference. Simulated PRN05 is added back to this difference to account for the removed atmospheric effect as a result of the single difference (left). The top and the negative elevation bending region in the observations are replaced with the simulated profile using refractivity profile calculated from BMX sounding at 00Z on February 23, 2008 (right).

6.2 Comparison of the retrieved and COSMIC refractivity profiles

The COSMIC [Anthes et al., 2000] provides global RO profiles, however it typically provides only one profile within a 500 x 500 km region per day. The comparison of the quality of the airborne relative to the spaceborne dataset will allow assessment of the potential value of the higher temporal and spatial resolution provided by airborne RO measurements. This opens doors to future assimilation tests using the same algorithms that have been developed at many operational centers for incorporating RO data into numerical weather prediction models.

During the 5 hour flight on February 15, there were only 5 spaceborne occultations available in the vicinity of the survey area (Figure 6.7). We present the PRN15 occulting satellite, the closest COSMIC profile to the flight path of the available spaceborne occultations, in comparison with the PRN13 airborne RO case as they

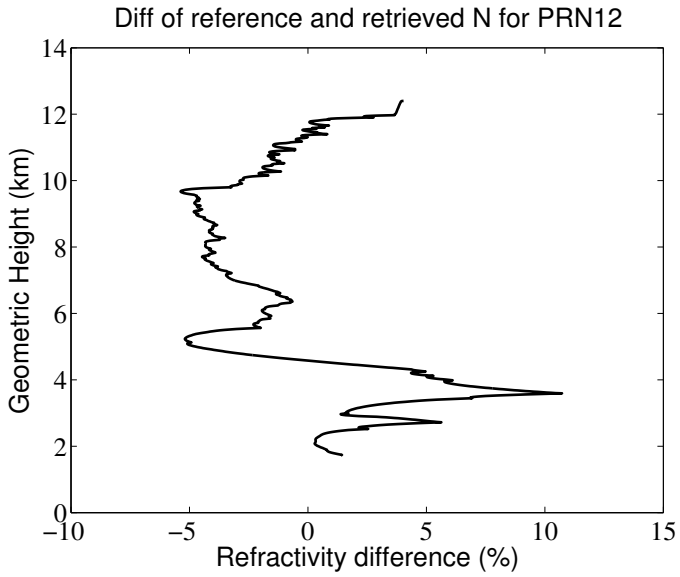

Figure 6.6.: Refractivity profile derived from BMX radiosonde station measurements at 00Z on February 23, 2008.

take place in the same area and are temporally separated by less than an hour (the airborne RO profile starts at 17:25 while the spaceborne RO starts at 16:58).

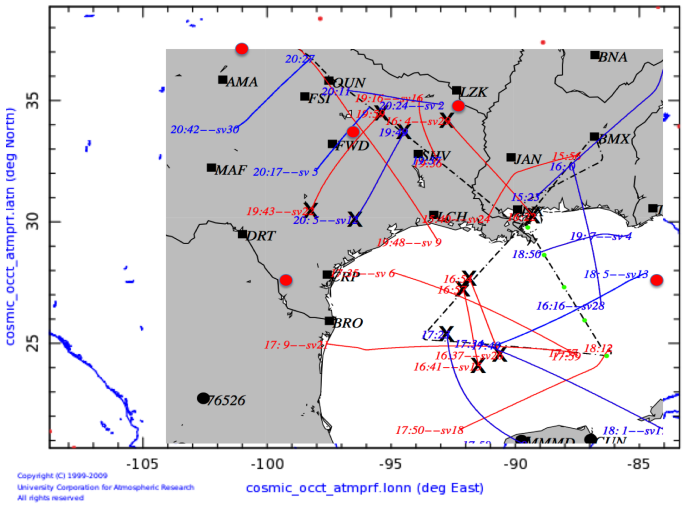

Figure 6.7.: Spaceborne RO profiles (red dots) available during the February 15 2008 flight.

Figure 6.8 shows the bending angle for PRN13 (black) and PRN15 (red) occultations. Although the bending angle profile from airborne RO measurements are biased with respect to the spaceborne RO, this comparison clearly shows variations in the bending angle that are common to the two. The percent difference of refractivity profiles from airborne, spaceborne and the ECMWF analysis are compared to the model refractivity (CIRA-Q), and this comparison is shown in the right panel of Figure 6.9 in black, blue and red lines respectively. These refractivity differences show that although the airborne RO profile is biased, it clearly captures the layered atmospheric structure similar to spaceborne RO profile, and at the correct heights. The difference between the retrieved refractivity for PRN13 setting occultation and the refractivity for the reference PRN15 satellite from spaceborne measurements (left panel of Figure 6.9) shows a bias of 5.5 %, with a standard deviation of 1.42 % below about 11 km altitude. Therefore, once the source of the bias in the retrieved refractivity is found, similar impact to spaceborne RO can be expected from airborne RO measurements when assimilated in NWP models.

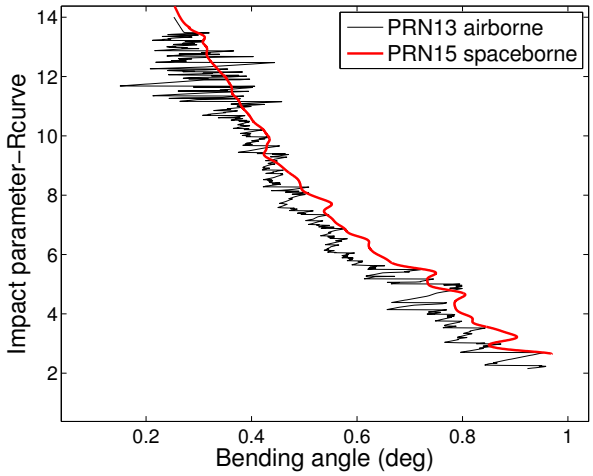

Figure 6.8.: Bending angle profiles for PRN13 (airborne RO) in black and PRN15 (spaceborne RO) in red.

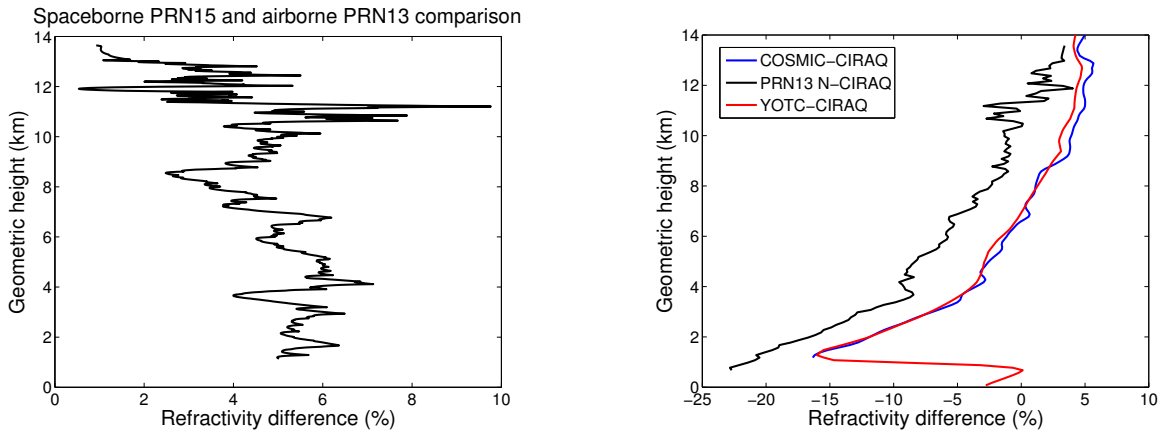

Figure 6.9.: The percent difference of retrieved refractivity profile for PRN13 (airborne RO) and PRN15 (spaceborne RO) occultations.

To summarize, the study of the accuracy of the airborne RO measurements in comparison with independent set of measurements shows that there is a bias of yet unknown origin in the airborne RO profiles. The spaceborne RO comparison illustrates that the airborne RO captures similar features present in the COSMIC profile in spite of the current bias. The comparison with a refractivity profile calculated from a radiosonde sounding once again shows that the airborne RO profiles are biased with a standard deviation of 2.3 % above 5 km. Thus, once the origin of the bias is found and removed, the airborne RO measurement errors will be within the range of the observation errors typically assigned to radio occultation data below 10 km during assimilation. Although we successfully retrieved profiles to lower than 1 km height (Chapter 5) for most of the occultations, below 6 km altitude the geometric optics retrieval algorithm does not suffice. A Full Spectrum Inversion (FSI) can potentially improve the performance of the airborne RO system providing valid profiles especially below these heights. Applying the FSI to this data set will also help to better understand the airborne RO accuracy. The FSI technique requires an inversion of the phase and amplitude profiles directly, and we have successfully recovered valid phase and amplitude profiles from the airborne RO measurements, with variations similar

to those seen in COSMIC data. This new dataset will be of interest to larger community involved in data assimilation, as studying the 3-dimensionally varying lower tropospheric moisture field from RO remains problematic.

6.3 Sensitivity tests of the retrieval to different parameters

At different steps of the refractivity retrieval from the airborne RO measurements using the geometric optics retrieval method, we make assumptions about some parameters, or make use of external data sets such as in-situ measurements of atmospheric parameters. We perform sensitivity tests to study how these assumptions and errors in independent measurements will affect the retrieved values.

6.3.1 Sensitivity of the retrieval to refractivity at the receiver

The calculation of the bending angle from the excess Doppler as well as the Abel inversion of the partial bending angle to acquire a refractivity profile (both described in Chapter 1) require information about the refractivity at the receiver from the in-situ temperature measurements. These high rate (50 Hz) measurements are made with a fast response, all weather deiced (Rosemount model 102Al TAT) sensor with $\pm$ 0.5 C° accuracy (http://www.hiaper.ucar.edu/handbook/index.html). For the sensitivity studies, retrievals for occultations on February 15 2008 are considered. A thorough analysis for all occultation cases for this flight day will be presented in Chapter 5. The in-situ humidity sensors during the February 15 flight were not functioning, therefore, we assumed negligible humidity at the flight level in the calculation of refractivity. The calculated values for all airborne RO cases discussed in next Chapter are within $0.3 - 1$ N units agreement with the climatological profile which we assume for the atmosphere above the airplane height.

We study the sensitivity of the airborne RO retrieval to the refractivity at the receiver value considering the retrieval for PRN13 setting satellite during the February 15 flight. The in-situ measurements are modified by $\pm$ 2 N-units, which is equivalent

to 3.4 % for flight level atmospheric conditions. Figure 6.10 shows the percent difference of the retrieved profile relative to the reference ECMWF analysis refractivity profile for the PRN13 setting occultation (black line) using the in-situ refractivity at the receiver value. The blue and red lines represent the retrievals using values for refractivity at the receiver that are 2 N-units higher and lower respectively. Thus, 3.4 % errors in the in-situ refractivity values can affect the retrieval by introducing a bias that is increasing with height. Smaller values of 0.3 to 1 N-units observed for other retrieval cases will have a smaller effect.

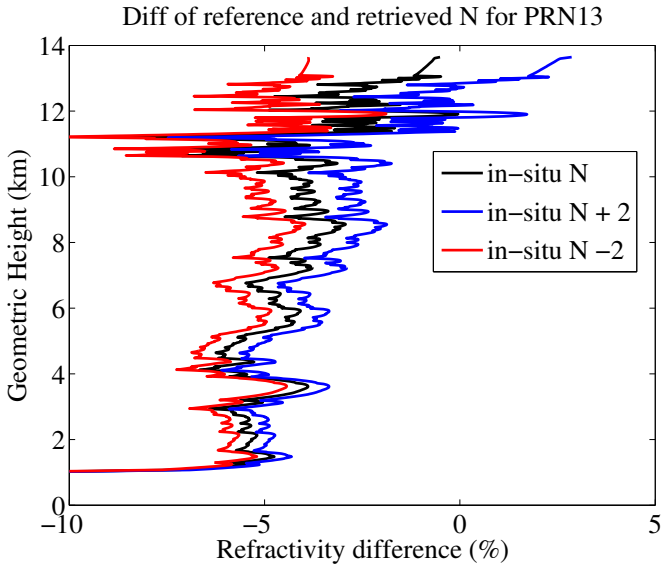

Figure 6.10.: Percent difference of the retrieved and reference ECMWF refractivity for PRN13 setting occultation (black line). Blue and red lines show the percent difference when the in situ refractivity measurements are contaminated by 2 and -2 errors respectively.

6.3.2 Sensitivity of the retrieval to the refractivity profile above the aircraft

As mentioned in Chapter 1, the bending angle profiles in the airborne RO technique are separated into two components - positive and negative elevation bending

angles for rays reaching the aircraft from above and below the local horizon respectively. The random noise in the aircraft velocity, mainly due to turbulence, has a very large effect at the top of the bending angle profile corresponding to 0° elevation rays, and also for the positive elevation bending where the accumulated bending is quite small. Therefore, throughout this work we have replaced the observed positive bending angle and the negative elevation bending from the maximum impact height to 1 km below the maximum impact height with the simulated bending angle from the CIRA-Q monthly mean climatology [Kirchengast et al., 1999].

We study the effect of the assumptions about the refractivity above the aircraft height on the retrieval for the PRN13 setting occultation by comparing the retrieved refractivity replacing the top and the positive elevation bending using two different assumed models. One model is the CIRA-Q climatological profile for the month of February and at $Latitude = 27.83^\circ$, which is the latitude of the tangent point closest to the surface. The second model is the ECMWF profile at $[Lat\ Lon] = [27.5\ -84.75]$ at 18 UTC, which is the grid point closest to the tangent point. The CIRA-Q and ECMWF profiles used in this test differ little in refractivity above the aircraft height, but have a significant difference in tropopause structure. The refractivities are quite different below 8 km.

Figure 6.11 shows that the differences between the simulated positive elevation bending using the ECMWF and CIRA-Q profiles are small. As expected, the bending angles are very different for the lower part of the negative elevation bending region. For the two retrievals using the CIRA-Q or the ECMWF profile above the aircraft height, Figure 6.12 shows the percent difference of the retrieved profile with respect to the reference ECMWF profile: the black line shows the case when the top and the positive elevation bending are replaced with the simulation using the CIRA-Q profile, and the red line illustrates the case when they are replaced with the simulation using the ECMWF profile. This comparison shows that the retrieved refractivity profile below 10 km changes by less than 0.5 % when assuming different atmospheric model profiles above the aircraft height, either from the ECMWF analysis profiles or from

the CIRA-Q climatology. Most importantly, we see that the assumption made above flight level is not responsible for the 5 % bias in the retrieved refractivity below 10 km as seen in Chapter 5. It is interesting that the use of the CIRA-Q model, which does not represent the height of the tropopause locally, produces rapid large variations in the retrieved refractivity at the tropopause height.

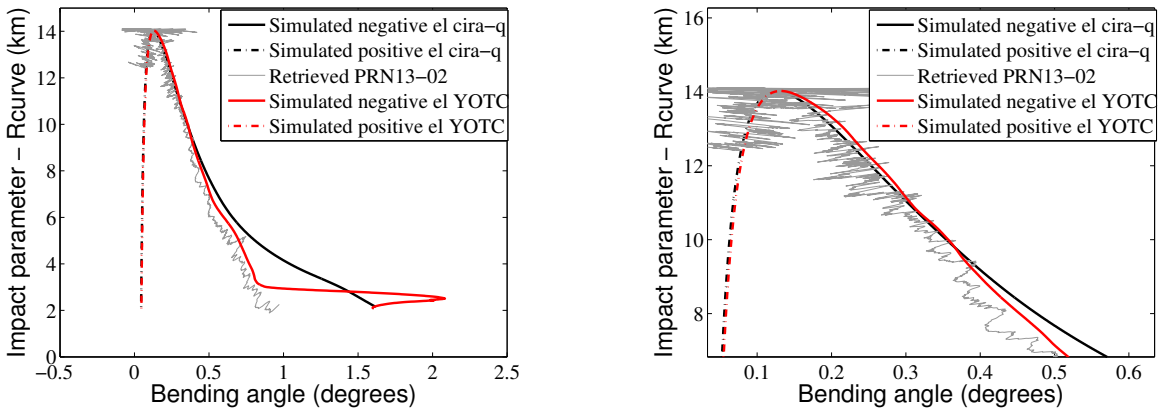

Figure 6.11.: The retrieved bending angle for PRN13 setting occultation (gray), and the simulated bending angles using the CIRA-Q (black) and ECMWF (red) refractivity profiles (left). The same figure is shown on the right with the top of the bending angle profile magnified for visibility of the simulated bending angle differences.

In the routine processing of airborne RO presented in Chapter 5, we use the CIRA-Q model for the a priori model above the aircraft flight level. However, we also test the possibility of using the RO observations themselves to extrapolate a profile for the height above where we start the replacement. For this example, we consider the PRN12 setting occultation during February 15 flight, which has a large offset in the observed bending angle with respect to the simulated ECMWF analysis profile at the height of the bending angle replacement. We carry out the following procedure to derive a profile that produces a better representation of the observed bending angle profile at the replacement height:

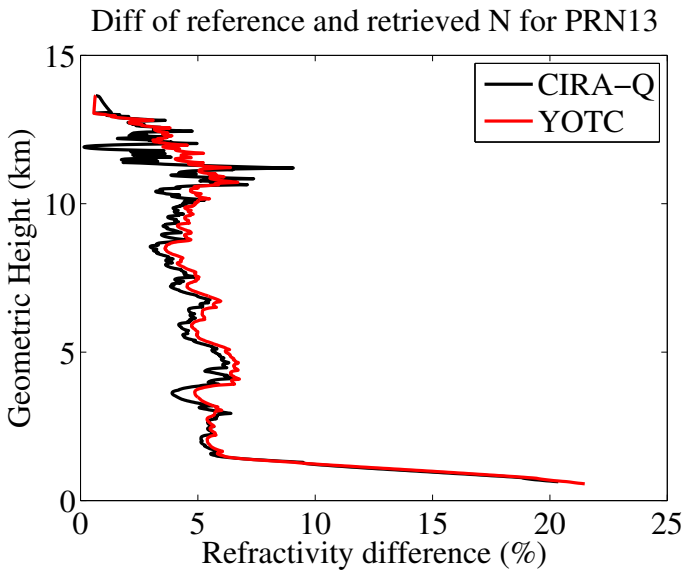

Figure 6.12.: The difference of the two retrieved refractivity profiles (PRN13 setting occultation) with respect to the reference ECMW Frefractivity profile. The two retrievals were based on bending angle profiles where the top and the positive elevation bending were replaced with simulated bending using ECMWF (red) and CIRA-Q (black) profiles.

- Use the complete (noisy) positive and negative elevation bending angle profile calculated from the excess Doppler difference for PRN12 and high elevation PRN24 satellites (gray line in Figure 6.13 (right)) to calculate the partial bending angle
- Retrieve refractivity using this noisy observed partial bending angle profile (red line in Figure 6.13 (left))
- Fit a Fourier 1^{st} degree polynomial model ($a_0 + a_1 cos(xw) + b_1 sin(xw)$) to the retrieved refractivity profile (black line in Figure 6.13 (left)) and extrapolate to the height of the aircraft
- Simulate bending angle from this Fourier fit to the refractivity (black line in Figure 6.13 (right))

- Replace the top and the positive elevation bending angles down to the replacement height with the simulated bending angle profile from the Fourier fit refractivity

- Retrieve refractivity from this combined bending angle profile via the Abel integral inversion

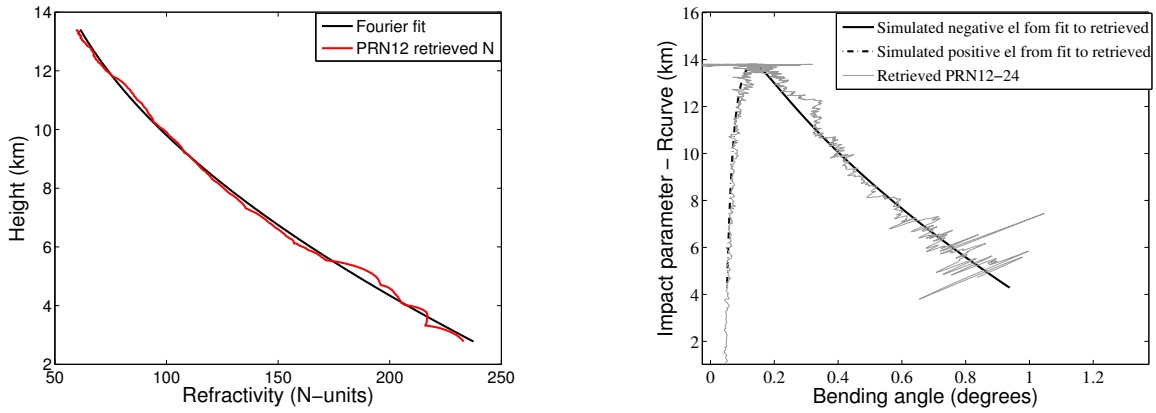

Figure 6.13.: Retrieved refractivity for PRN12 and its Fourier fit (left). Simulated bending angle from the Fourier fit to PRN12 refractivity (black line), and PRN12 observed bending angle (gray line).

Figure 6.14 shows the percent difference of the two retrieval cases relative to the ECMWF reference refractivity profile for the PRN12 setting occultation. The red line is the case when the replacement used the Fourier fit to the refractivity profile retrieved from PRN12 RO measurements, while the black line shows the case when the replacement used the CIRA-Q climatological profile. The results show that for this occultation, assuming an atmospheric model above the aircraft height that has been simulated from a fitted refractivity profile improves the retrieval result by 0.8 % from 6 to 11 km.

This sensitivity study for both PRN13 and PRN12 occultation cases (Figure 6.12 and 6.14 respectively) demonstrate that although the assumptions we make about

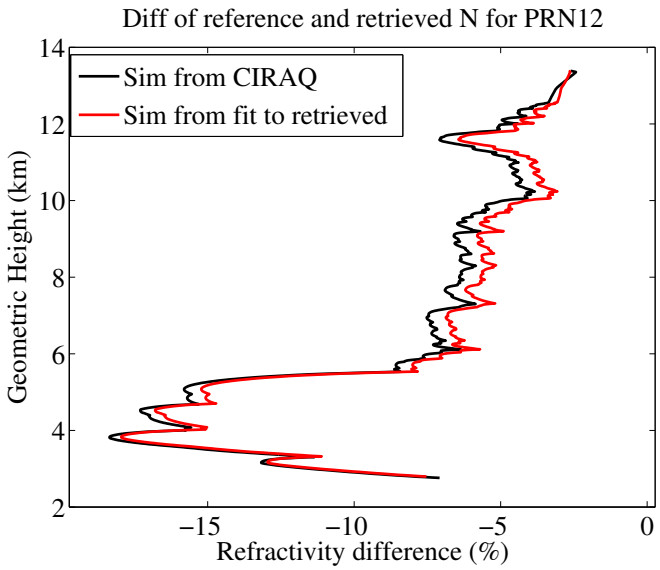

Figure 6.14.: The difference of the retrieved (PRN12 setting occultation) and reference ECMWF refractivity profiles replacing the top and the positive elevation bending with simulated bending from CIRA-Q climatology (black) and a simulation from a refractivity profile which is a Fourier fit to the PRN12 refractivity.

the refractivity above the aircraft height affects the retrieved profile, its effect is small compared to the current retrieval bias (Chapter 5), however, it needs to be carefully taken into account to achieve the desired 0.5 % in retrieved refractivity accuracy.

6.3.3 Sensitivity of the retrieval to a bias in the excess Doppler

The excess Doppler profiles from the OL tracking should be near zero mean at the beginning of tracking, when the satellite is at relatively high elevation angles. However, the Doppler profiles often have a small bias in the beginning, usually on the order of 0.002 to 0.005 m/s, which can result in a bending angle bias. To evaluate how big of an effect a constant bias in the excess Doppler would have on the calculated bending angle, we add and subtract 0.005 m/s to a simulated excess Doppler profile based on an ideal airplane/satellite geometry. The ideal occultation geometry is generated with a circular GPS orbit and an airplane trajectory at a fixed height. The height of the GPS satellite is chosen to be $20,000$ km above the Earth's surface. The velocities of the GPS satellite and the airplane are specified to be 3.83 km/s and 0.25 km/s respectively. In this ideal case, both the airplane and the GPS satellite are moving away from each other in the same Y-Z plane. An exponential *1-D* refractivity profile with a fixed height scale $H = 7$ km is used in the bending angle simulation, such that $N(h) = N_0 exp(-\frac{h}{H})$, where h is the altitude and $N_0 = 385$ is the refractivity at the surface.

Figure 6.15 shows the bending angle calculated from the simulated excess Doppler (blue line), and bending angles when the excess Doppler is offset by 0.005 m/s and -0.005 m/s (red and green lines respectively). The right panel in Figure 6.15 shows the top of these bending angle profiles on a larger scale demonstrating that a positive offset of 0.005 m/s in the excess Doppler moves apart the positive and negative elevation bending profiles with the largest separation being at the top of the profile (0° elevation), while the negative offset of the excess Doppler causes the negative and positive elevation bending angle profiles to cross over with maximum underestimation (overestimation) of negative elevation (positive elevation) bending angles at the top of the profile. Figure 6.16 shows the percent difference of the retrieved and the reference exponential refractivity profiles (blue line), and the percent difference when the excess Doppler is offset by 0.005 m/s (red line) and by -0.005 m/s (green line).

Thus, although the offset in the excess Doppler profile in the beginning of tracking results in a bias in the retrieved refractivity, it is negligible compared to the current bias in the retrieved profiles presented in Chapter 5.

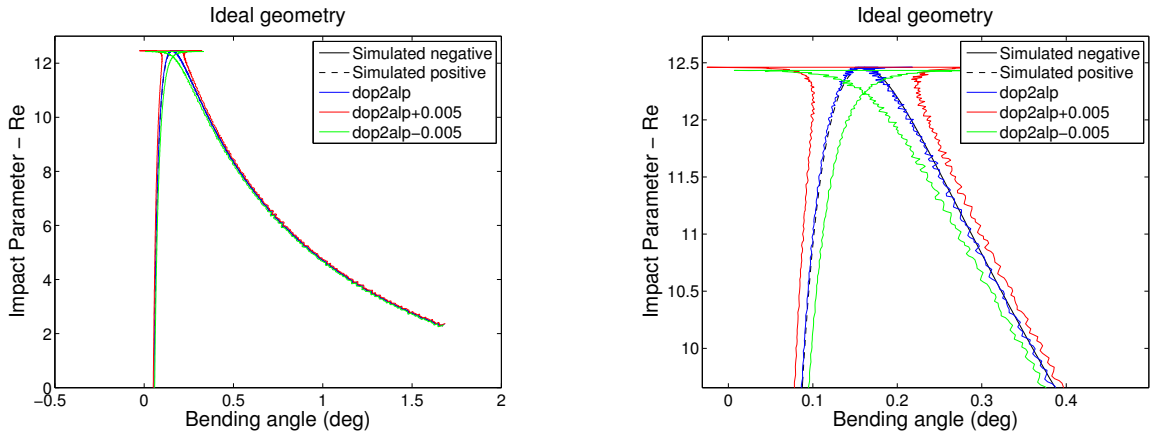

Figure 6.15.: The change in bending angle introducing $-0.05\ m/s$ (red) and $0.05\ m/s$ (black) excess Doppler error. The unaltered excess Doppler is shown in blue line.

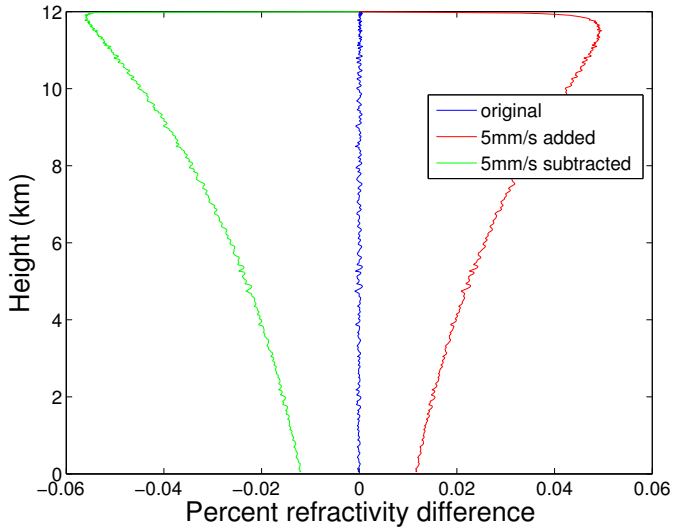

Figure 6.16.: The change in retrieved refractivity introducing $-0.005\ m/s$ (red) and $0.005\ m/s$ (black) excess Doppler error.

To summarize these sensitivity tests, the effects of potential error sources in the geometric optics retrieval from the airborne RO measurements are evaluated to be small. Having thoroughly studied the impacts of the errors at different steps in the retrieval method, the excess phase profiles from automated OL tracking procedure are used in a systematic study of retrievals of airborne RO measurements presented in the next chapter.

7. DEPICTION OF SYNOPTIC SCALE WEATHER AND TROPOPAUSE HEIGHT WITH AIRBORNE RO MEASUREMENTS

Spaceborne GPS RO has generally been found to provide valuable information on the vertical structure of the upper troposphere and lower stratosphere [Foelsche et al., 2007], resulting in overall improvement in global NWP for synoptic scale weather systems [Cucurull, 2007; Healy and Thepaut, 2006; Poli et al., 2010; Wee and Kuo, 2008]. Because airborne RO measurements have similar horizontal averaging lengths, they also would be expected to be most valuable for providing information on the synoptic scale, as opposed to mesoscale. To assess the airborne RO capacity to depict synoptic scale variations, we present the synoptic weather situation for February 15, and analyze the airborne RO retrieved refractivity variations for this day. Comparisons with the ECMWF analyses profiles are also useful to provide guidance on the type of refractivity profiles expected given the context of atmospheric temperature and moisture variability present on that day.

Figures 7.1 and 7.2 depict the synoptic situation from 00Z February 14 to 00Z February 16 (weather.unisys.com). These composite weather maps contain the analysis of radar reflectivity, surface data, frontal locations and pressure contours, as well as the infrared (IR) satellite cloud images. The latter shows the emission from the IR region of the solar spectrum, with high cold clouds interpreted from the brightest shades. These figures show a cold front already formed at 00Z on February 14 and moving from the Northern US to Southeast (Figures 7.1). As the front moves southwards, the heavier cool air pushes under lighter warm air causing uplift and cooling as it is being replaced by cooler air at the surface. The February 15 flight (from 18Z

to 21Z) passes over the cold front and its (Figures 7.2) associated clouds (white cloud tops) and heavy precipitation (colored contours) along the frontal line.

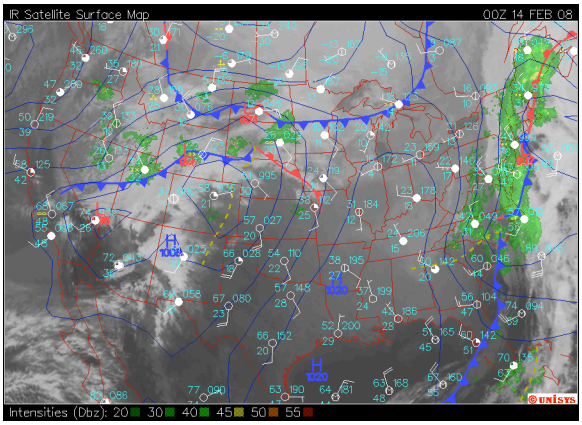

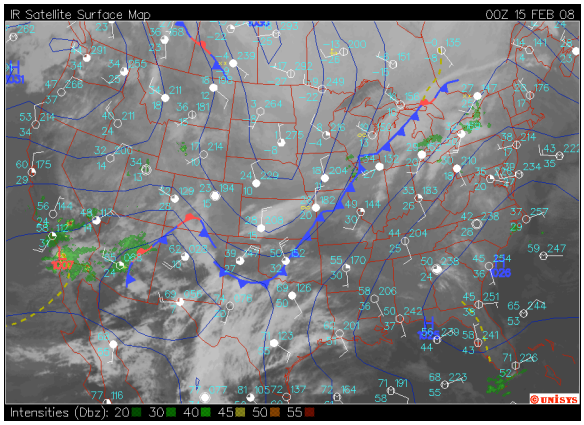

Figure 7.1.: Composite surface data and IR map at 00Z on February 14 and 15, 2008. The cooler surfaces are illustrated with bright areas indicating possible clouds with high cloud tops shown in white, while low clouds are more gray. Dark areas represent possible clear sky conditions.

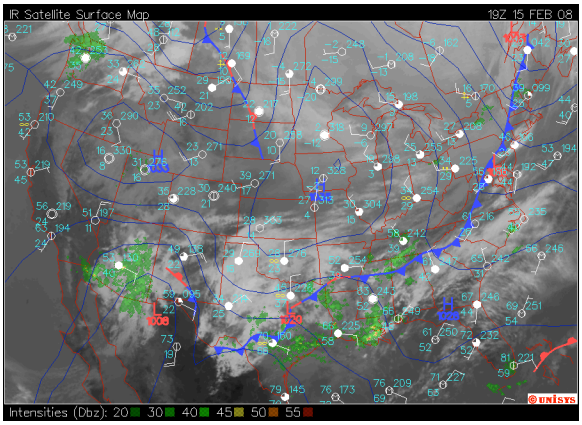

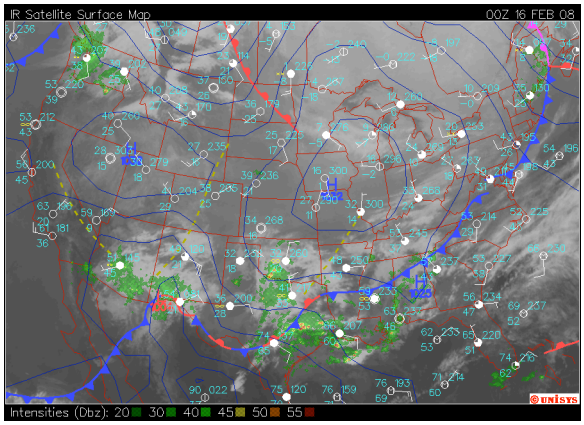

Figure 7.2.: Composite surface data and IR map at 19Z on February 15 (left) and at 00Z on February 16 (right). During the flight period, the cold front passes through the survey area.

Figure 7.3 shows the February 15 flight trajectory and the occultation tangent point locations with respect to the cold front location at 19Z on February 15, which is superimposed in the thick blue line. The cold front is expected to divide the flight region into generally cooler area behind the front and warmer conditions ahead of frontal line. The set of occultations discussed in Chapter 5 can be separated into 5 groups of occultations sampling different atmospheric conditions. These groups shown in colored circles in Figure 7.3 (tones of blue for colder northern profiles and tones of red for warmer profiles) are as follows: PRN30 and PRN05 setting occultations (in Texas); PRN22 rising and PRN12 setting occultations (in Texas); PRN29 rising occultation (in Arkansas); PRN09 setting and PRN26, PRN15 rising occultations in western Gulf of Mexico coastal region; and PRN13 in the eastern Gulf. The five different regions extend from north to south with latitudinal separation of approximately 10°.

We analyze one occultation that is representative of each of the groups of co-located airborne RO profiles. To be able to effectively and uniformly evaluate the synoptic scale variations captured with airborne RO measurements, we compare all profiles to a reference climatological profile (CIRA-Q) at $Lat = 28°$, in the center of the study region, which is shown in red star in Figure 7.3. In this way, we can illustrate the large-scale synoptic scale variations of the RO data relative to an average profile, and also investigate whether it shows the same large-scale pattern as the ECMWF analysis profiles.

Figure 7.4 illustrates the upper air conditions at $00Z$ on February 16. The top figure shows the 850 mb temperature in Celsius (color contours) derived from the ETA model [Janjic, 1990] initial gridded data (www.weather.unisys.com), and the lower figure shows the 850 mb geopotential heights (black lines) (Unisys data retrieved from locust.mmm.ucar.edu). The lower figure also shows information on temperature and dew point temperature with the green lines representing high moisture regions. This map confirms the cold temperatures behind the frontal line moving to the southeast, with higher moisture regions along the frontal boundary, where the IR and radar

images also indicate (Figure 7.2) clouds and precipitation. The driest region is associated with the high pressure zone in the Eastern coastal region (Figure 7.2), where PRN13 occultation takes place. The clear separation of dry air conditions for the PRN13 occultation region is also shown in the integrated water vapor imagery in Figure 7.5.

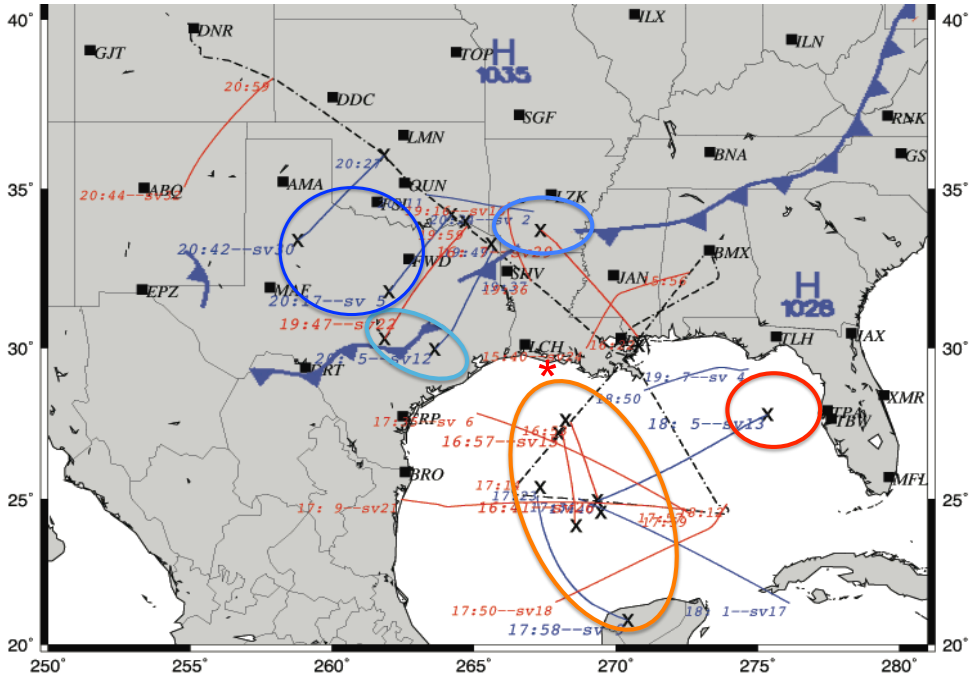

Figure 7.3.: Map of February 15 flight. The cold front moving in the region from North is shown in thick blue line. The set of occultations during this flights represent five regions circled with blue colors for associated cold temperatures behind the front, and orange and red for expected warm regions ahead of the cold front. The lowest tangent point locations for each occultation are shown in crosses. The red star shows the location of the reference climetological profile ($Lat = 28°$).

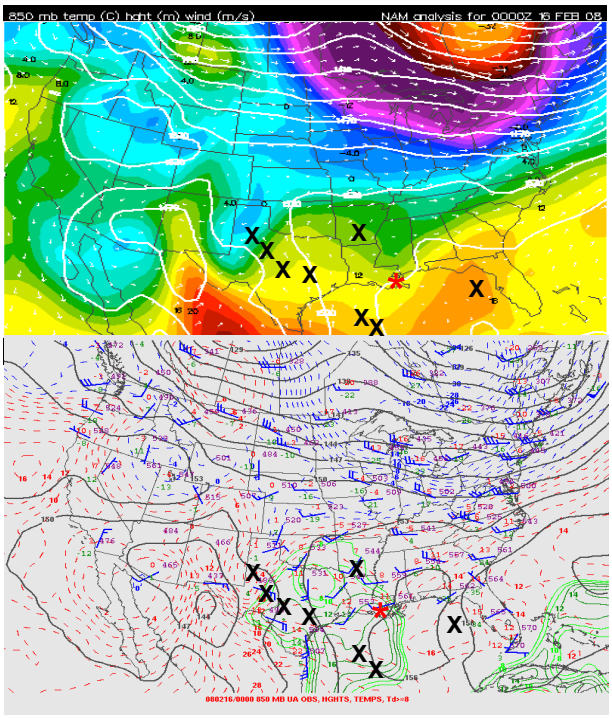

Figure 7.4.: 850 mb temperature (top) and heights (bottom) at 00Z on February 16 2008. The crosses denote the lowest tangent point location for each occultation, while the red star shows the reference CIRA-Q profile location.

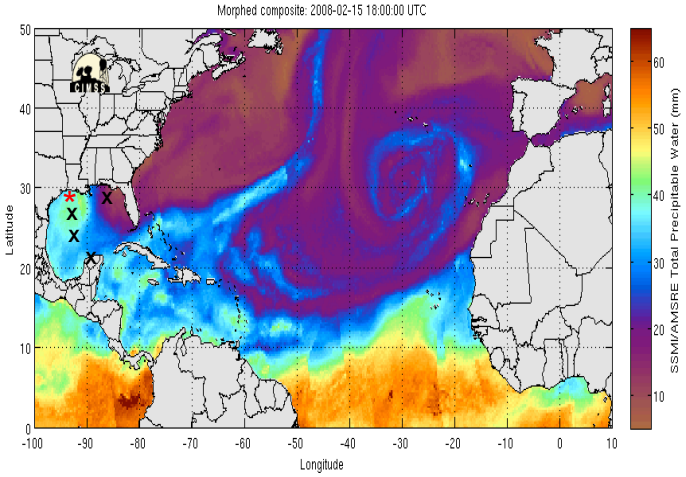

Figure 7.5.: Total precipitable water at 18Z on February 15 2008. PRN13 occultation takes place in a region of dry air in the eastern Gulf of Mexico (Morphed Integrated Microwave Imagery at CIMSS (MIMIC) from tropic.ssec.wisc.edu).

The PRN30, PRN22, PRN29, PRN09 and PRN13 occultations are compared to the closest ECMWF analysis grid point profiles in figures 7.6, 7.8, 7.10, 7.12 and 7.14, respectively. The airborne RO profiles are color coded from cold (blue) in the north to warm (red) towards the south. In the left panel of figure 7.6, for example, the reference climatological profile at $Lat = 28^{\circ}$ for temperature (T) and dew point temperature (T_{dew}) are shown in black. The same CIRA-Q profile at $Lat = 28^{\circ}$ is used as a common reference for all occultations. The light gray solid and dashed lines show T and T_{dew} for the CIRA-Q profile at the latitude of the lowest tangent point location, which is $Lat = 32.972^{\circ}$ for the PRN30 occultation. This illustrates the climatological scale variation between the monthly average at the latitude of the occultation and the reference latitude. The monthly average values, for example, at this northern location are about 2 degrees cooler, and significantly drier from the surface to 10 km than the reference location. The ECMWF T and T_{dew} profiles at the location of the PRN30 occultation are shown in blue.

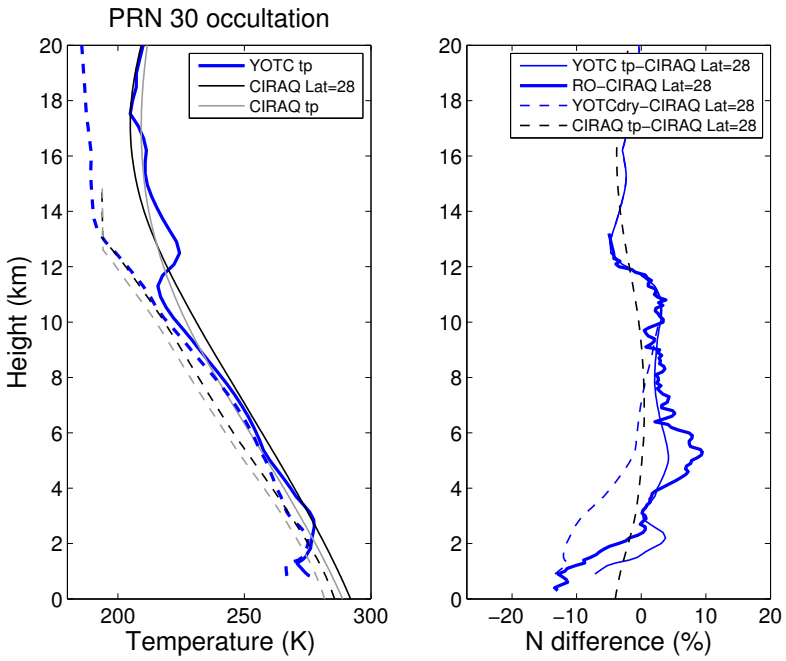

Figure 7.6.: T and T_{dew} from ECMWF analysis reference profile for PRN30 occultation (left). The percent difference of retrieved (thick line) and ECMWF profiles (thin line) with respect to mean CIRA-Q climatology (right).

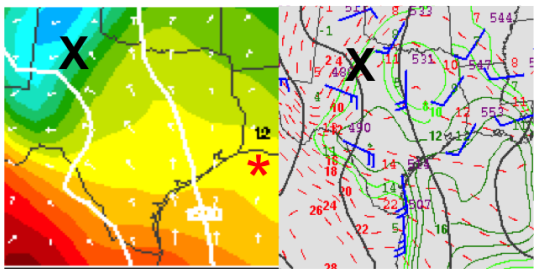

Figure 7.7.: Temperature (left) and moisture (right) in the region of PRN30 occultation. The lowest tangent point location for PRN30 is shown with a cross, while the reference CIRA-Q profile location is shown with a red star.

The right panel of Figure 7.6, shows the percent difference between the climatological value of refractivity from CIRA-Q at $Lat = 32.972°$ and the reference refractivity at $Lat = 28°$. At this latitude, the temperatures above the tropopause in the CIRA-Q model are warmer than the reference profile, yielding lower refractivity shown in the dashed black line in the right panel. Below 10 km, the cooler and dryer CIRA-Q climatological profile produces overall lower refractivity than the reference at $Lat = 28°$, indicating the effect of moisture dominates in reducing refractivity as predicted by equation 1.11, especially below 6 km. The ECMWF profiles illustrate the synoptic scale variations from the monthly climatological mean on this particular day. Near the PRN30 occultation tangent point, the ECMWF profiles of T and T_{dew} (Figure 7.6, left panel) show nearly saturated air from 5 to 11 km altitude, and a large temperature inversion at about 12 km corresponding to the tropopause height, which is the boundary between the troposphere and the stratosphere. The monthly mean climatological profile, on the other hand, does not exhibit a sharp tropopause, but only a gradual increase in temperature above 16 km height.

There is very little moisture at these altitudes, therefore, the difference in refractivity between the ECMWF and CIRA-Q climatology (right panel) shows a direct correspondence with temperature above 10 km. This is expressed as a change in slope in the refractivity difference from a cool/higher refractivity layer at 11 km to a warmer/lower refractivity layer at 13 km. This agrees very well with the tropopause signature in the RO observations, also shown in Figure 7.6 (right panel) in the bold blue line. In general, the PRN30 retrieved profile shows an excellent agreement with the ECMWF analysis from 6 km to flight altitude where the airborne RO profile captures the very moist atmospheric layer, which is expressed as a positive refractivity difference relative to the reference refractivity. The agreement between the retrieved RO profile and the ECMWF profile degrades from 1 to 6 km altitude, however the RO observations show the height level of the peak in moisture at 5 km, and a decrease in refractivity at 3 km altitude similar to that of ECMWF profile, indicating a layer of drier air where the atmosphere is not saturated.

The sequence of figures 7.6 through 7.14, provide guidance in understanding the refractivity variations of the airborne RO retrieved (thick lines) and ECMWF analysis (thin lines) with respect to the reference climatological (CIRA-Q) profile, since interpreting the refractivity profiles is not necessarily obvious or intuitive to the meteorological community. The dashed colored lines in the right panels show the contribution of the dry air pressure and temperature to the refractivity (from Equation 1.11) in the ECMWF analysis profile and the CIRA-Q profiles. From this one can see that there is virtually no contribution to refractivity above 10 km, there is about 5 % of the refractivity contributed by moisture in the 5-10 km height range, and there is a very large contribution from moisture below 5km, reaching 20 % at the surface. Also it is clear that most of the sharp variations in refractivity structure are coming from moisture variations, as the effect of temperature variations is usually very subtle below 5 km. The full set of figures for all 9 occultations are provided in the appendix. Figures 7.7, 7.9, 7.11, 7.13 and 7.15 show the atmospheric conditions (temperature on the left and moisture (in terms of dew point temperature) on the right) for regions containing each of the five occultations with the lowest tangent point locations denoted with crosses.

Continuing with the discussion of specific synoptic regions, T and T_{dew} from the ECMWF analysis profile for the PRN22 occultation show saturated air from about a layer of dry air from 5 to 10 km altitude (Figure 7.8), in a region where cold and high cloud tops are seen in the satellite imagery. There is a sharp temperature inversion at the tropopause height at approximately 12 km, which is well expressed in the percent refractivity difference (right panel) in Figure 7.8 for both the RO profile and the ECMWF analysis with a sharp decrease in refractivity as the air becomes warmer at the tropopause. Although the retrieved profile is biased with respect to the ECMWF analysis profile, the refractivity variations agree very well at all height levels, and in particular the dry layers at 7 and 3 km altitudes expressed as a decrease in the refractivity (Figure 7.8).

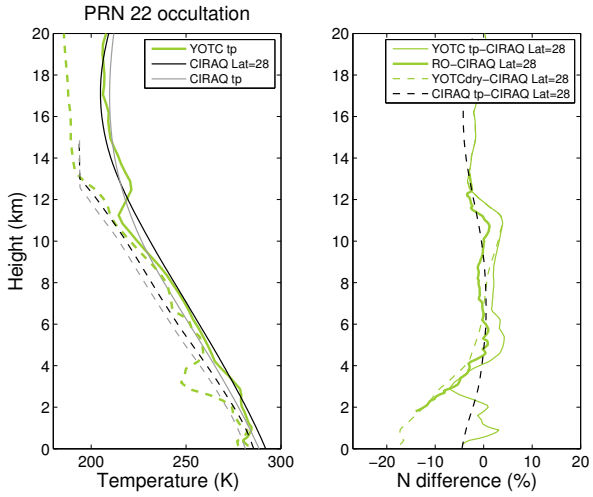

Figure 7.8.: T and T_{dew} from ECMWF analysis reference profile for PRN22 occultation (left). The percent difference of retrieved (thick line) and ECMWF profiles (thin line) with respect to mean CIRA-Q climatology (right).

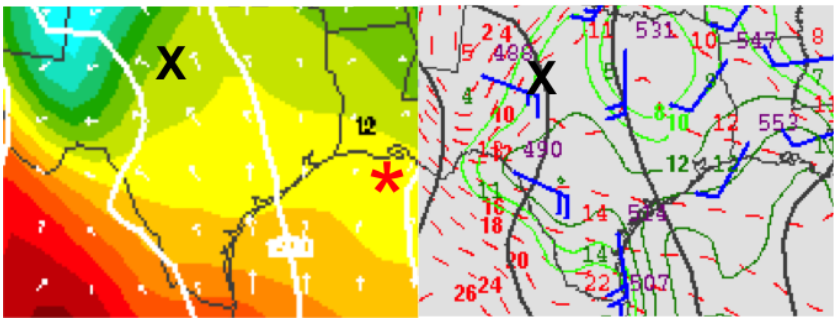

Figure 7.9.: Temperature (left) and moisture (right) in the region of PRN22 occultation. The lowest tangent point location for PRN22 is shown with a cross, while the reference CIRA-Q profile location is shown with a red star.

The tropopause height for the case of the PRN29 occultation is at approximately 11 km (Figure 7.10) shown as a slope change in refractivity. The retrieved and the ECMWF refractivity profiles are in good agreement from 5 to 10.5 km. Below this height, although the agreement once again degrades, the airborne RO profile is

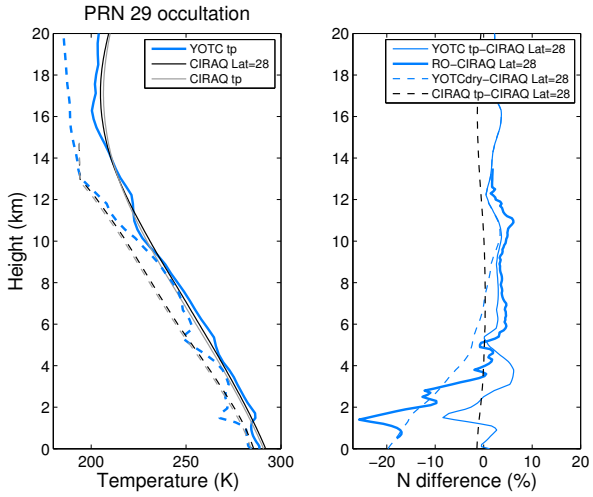

Figure 7.10.: T and T_{dew} from ECMWF analysis reference profile for PRN29 occultation (left). The percent difference of retrieved (thick line) and ECMWF profiles (thin line) with respect to mean CIRA-Q climatology (right).

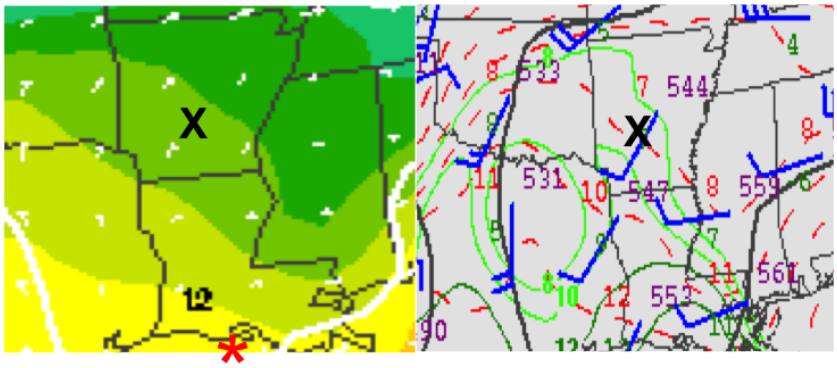

Figure 7.11.: Temperature (left) and moisture (right) in the region of PRN29 occultation. The lowest tangent point location for PRN29 is shown with a cross, while the reference CIRA-Q profile location is shown with a red star.

capable of indicating the correct heights of the dry atmospheric layers at 5 and 1.8 km with a sharp decrease in refractivity.

Although there are small temperature variations at 10 km and 13 km altitudes for PRN09 and PRN13 (Figures 7.12 and 7.14 respectively), the most significant temperature inversion indicating the tropopause is at the much higher level of about 16 km. Compared to the higher latitude profiles discussed above, there is evidence in the ECMWF profiles for a similar feature at around 16 km. The multiple changes in the temperature lapse rate are probably due to tropopause undulations and folding. This is when two or three thermal tropopauses are observed at different altitudes from a single vertical temperature sounding[Hirshberg and Fritsch, 1990]. These tropopause folds are thought to play a significant role in midlatitude cyclogenesis and in the development of severe weather in the lower troposphere [Hirshberg and Fritsch, 1990; Kim et al., 2001].

T and T_{dew} in both PRN09 and PRN13 cases indicate higher tropopause height of approximately 16 km which is typical of the tropopause at lower latitudes [Pan et al., 2008]. Since the tropopause is above the airplane cruising altitude of 13.5 km, the RO profiles do not exhibit the slope change in the refractivity as seen in previous three cases. We raise the possibility that the shorter wavelength variations seen at 11 and 13 km in the RO refractivity could be indicating the variations in moisture seen in the T_{dew} profiles, however this will require more investigation to demonstrate conclusively. The clear signal of the tropopause, or signal of the lack of tropopause, in all of the retrieved RO profiles is a very interesting result. It was unexpected from previous work [Muradyan et al., 2010] that indicated that it would be difficult to achieve high accuracy near the aircraft flight altitude. However, the evidence of the tropopause features in all profiles is conclusive.

The PRN09 and PRN13 occultation are interesting to contrast because of the extremely dry conditions sampled over the Gulf of Mexico by PRN13. For both profiles, the agreement with the ECMWF analysis profile diverges below 7 km altitude. As discussed in Chapter 5, because of the limitations of the geometric optics inversion when the bending angle is multivalued, the retrieved refractivity is often underestimated beneath sharp decreases in atmospheric moisture. In the case of the PRN09

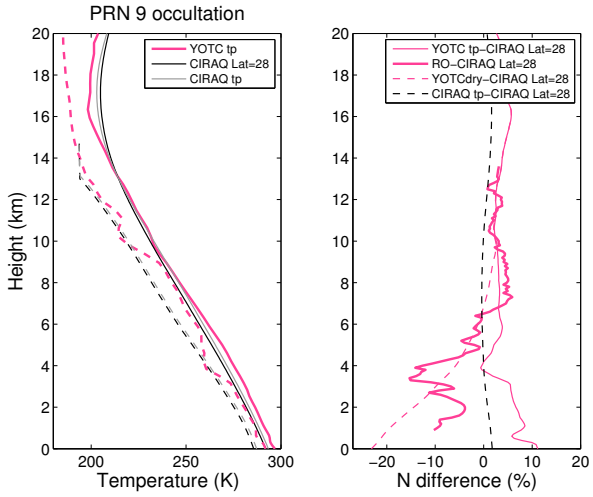

Figure 7.12.: T and T_{dew} from ECMWF analysis reference profile for PRN09 occultation (left). The percent difference of retrieved (thick line) and ECMWF profiles (thin line) with respect to mean CIRA-Q climatology (right).

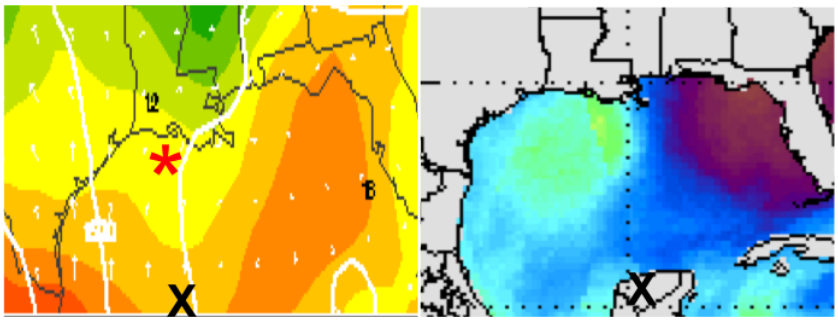

Figure 7.13.: Temperature (left) and moisture (right) in the region of PRN09 occultation. The lowest tangent point location for PRN09 is shown with a cross, while the reference CIRA-Q profile location is shown with a red star.

occultation (Figure 7.12), this is evidently the case. While the altitude of the dry layer at 4 km is correctly reproduced in the retrieved profile, the refractivity is underestimated. On the other hand, the PRN13 occultation (Figure 7.14) samples an area that is warm and very dry relative to the climatological average. In this case, the retrieved profile closely mimics the refractivity of the ECMWF analysis, where there

is a no significant contribution to the refractivity from the moisture. There is a large bias with respect to ECMWF that we have discussed previously, however there is very low moisture so there are no large variations to produce the cumulative underestimation of refractivity seen in PRN09. In summary, although we see the deficiencies of the current retrievals in terms of the bias of unknown origin, and underestimation of refractivity due to the geometric optics retrievals, we are still able to diagnose certain features of the synoptic scale refractivity variations due to moisture that are present in the region of interest.

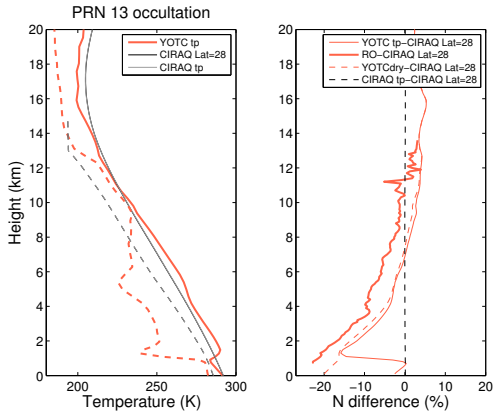

Figure 7.14.: T and T_{dew} from ECMWF analysis reference profile for PRN13 occultation (left). The percent difference of retrieved (thick line) and ECMWF profiles (thin line) with respect to mean CIRA-Q climatology (right).

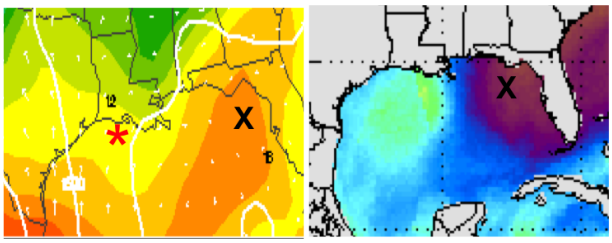

Figure 7.15.: Temperature (left) and moisture (right) in the region of PRN13 occultation. The lowest tangent point location for PRN13 is shown with a cross, while the reference CIRA-Q profile location is shown with a red star.

Figure 7.16 shows the percent refractivity differences between each of the ECMWF profiles and the reference CIRA-Q profile at $Lat = 28^{\circ}$ (left) in order to illustrate the expected systematic variations with latitude associated with the large scale synoptic pattern. In the right panel of this figure, the percent refractivity difference is for each of the profiles has been corrected by the amount at 10 km altitude. There is a clear north to south variation in refractivity above the tropopause with the expected warmer temperatures (lower refractivity) above the tropopause as latitude increases. Also, with the exception of PRN13, there is a systematic trend below 4 km to have moister air with higher refractivity as latitude decreases. Recall at the location of PRN13, the integrated water vapor imagery showed anomalously dry air.

(Figure 7.17) shows the percent refractivity differences between each of the retrieved RO profiles and the reference CIRA-Q profile for all occultation cases on February 15. The RO profiles demonstrate realistic variations above the tropopause from 12 km to flight altitude that agree with the variations seen in the ECMWF analysis. Recall that the climatological CIRA-Q model that was used as the a priori refractivity in the partial bending angle correction did not contain these variations, so that information was independently recovered from the RO data. Also the amplitude of the tropopause variations is recovered. Below this height, however, airborne RO profiles show systematic biases that seem to depend on latitude, with positive bias for higher latitudes and negative bias for lower latitudes. This may indicate the geometry as the potential source of the bias, and will have to be investigated further.

The features of airborne RO profiles from five different regions are consistent with the expected synoptic characteristics seen in the ECMWF analysis. In spite of the large biases, the RO signal is clearly capable of capturing the tropopause height as well as heights of strong variations present in the ECMWF profiles. The agreement between the airborne RO and ECMWF profiles, however, degrades below 4-5 km altitude, with the retrieved profiles demonstrating large negative differences with respect to the CIRA-Q profile. This is the region of heights where multivalued bending angle occurs (Chapter 5).

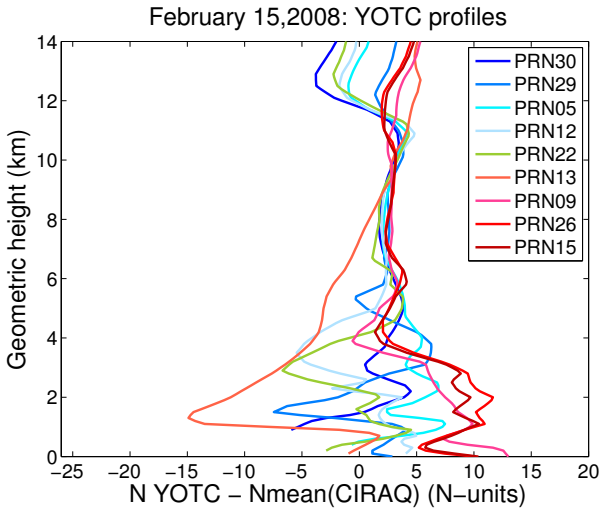

Figure 7.16.: The percent difference of nine reference ECMWF analysis profiles with respect to CIRA-Q profile.

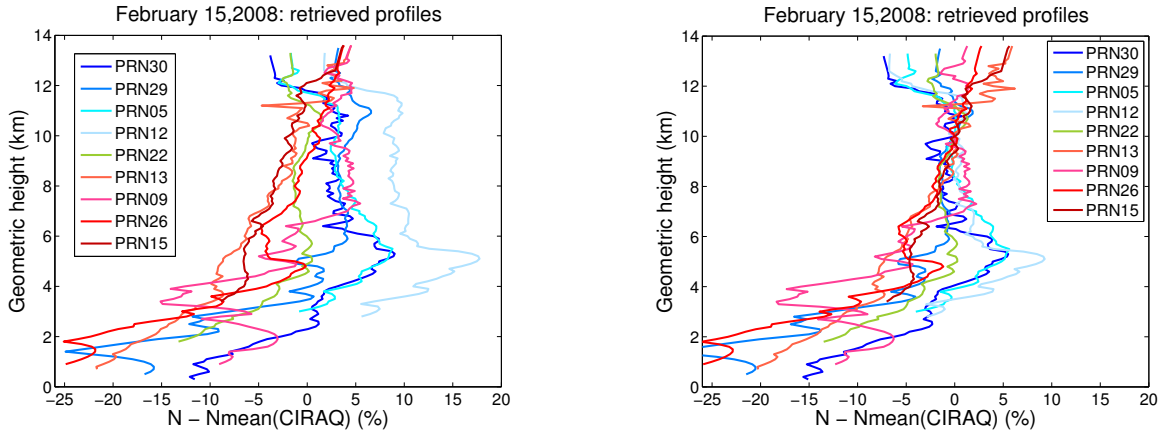

Figure 7.17.: (Left) The percent difference of retrieved airborne RO profile with respect to mean CIRA-Q profile. (Right) The refractivity percent difference is corrected for the bias at 10 km altitude for all profiles.

When calculating the partial bending angle, the non-monotonicity is eliminated by interpolation at different heights, which results in underestimated refractivity. As it can be seen in the case of PRN29, the agreement between the retrieved and ECMWF analysis profiles deteriorates below 5 km altitude, which corresponds to 6 km impact

height in Figure A.24, below which the partial bending angle (black line) is altered the most through in the ad hoc adjustment that assures monotonic behavior. Although a refractivity bias is also present in the lower tropospheric measurements in spaceborne RO [Beyerle et al., 2004; Sokolovskiy, 2001], it is much smaller. We expect that the airborne RO results will improve below 5 km with the implementation of the FSI method, which is also currently being used in spaceborne RO retrievals in the lower troposphere [Schreiner et al., 2007; Sokolovskiy et al., 2006].

Because of the large bias found between the RO and ECMWF analysis profiles, the RO profiles are not yet ready for assimilation into NWP models. However, the general results indicate that the airborne RO profiles clearly resolve the vertical atmospheric levels consistent with the synoptic scale variations. The new development in extending the airborne RO profiles through open loop tracking to altitudes below 1 km that clearly reflect atmospheric moisture variations, the technique will be very useful in providing information on the synoptic scale weather systems once the bias is removed and FSI is implemented.

The airborne RO profiles have now been shown to be able to resolve the tropopause height very well. Spaceborne RO measurements have successfully been used in different studies related to the tropopause height such as monitoring the global tropopause height trends [Schmidt et al., 2008], and studying the correlation between the tropical tropopause temperatures and inter annual changes in the stratospheric water vapor. Tropopause folds are thought to play a significant role in midlatitude cyclogenesis [Hirshberg and Fritsch, 1990; Kim et al., 2001]. Therefore, the airborne RO could also contribute to studies of the tropopause height in mid to higher latitude regions where the tropopause is lower than the flight altitude.

8. CONCLUSIONS

The lower troposphere is a challenging environment for the GPS RO technique because rapid changes in moisture content and lateral inhomogeneity contribute to multipath propagation and low signal strength. In this thesis we have analyzed the first flight data to use open loop tracking to recover observations of refractive delay due to the atmosphere from an airborne RO system. For a 5-hour flight at 13.5 km altitude on 15 February 2008, 19 rising and setting occultations occurred. We were able to successfully retrieve the excess phase and amplitude profiles using the OL tracking method for 5 setting and 5 rising occultations. We have implemented the airborne retrieval method for the OL observations and we have retrieved atmospheric refractivity profiles with comparable quality for both rising and setting occultations. The most important reason for the missed occultations (five profiles) was the lack or the poor quality of the navigation data bits necessary for the OL processing. Three occultations were lost due to aircraft turns during the occultation. Since 2008, the global network providing data bits has improved significantly, so that from a practical point of view the same airborne RO system deployed today on a straight flight path would achieve 3 occultations per hour of flight time.

The OL tracking software receiver consistently recovers data below 1 km in the atmosphere, with one profile reaching as low as 0.562 km in the atmosphere, even in the presence of sharp inversions at the atmospheric boundary layer. Given the success rate and the atmospheric heights of extracted excess phase profiles with the OL tracking method, the potential contribution of the airborne RO system to the NWP could be considered. The bending angle profiles have been shown to be biased relative to ECMWF analysis profiles. This bias can be as great as $5-6$ % in refractivity, over the height range from 4 km to flight altitude. This bias is present in the profiles retrieved from conventional receiver observations as well as in profiles retrieved from

the open-loop tracking. The standard deviation of the difference between the retrieved and reference ECMWF refractivity profiles is 0.75 % for setting satellite PRN13 and 1.5 % for rising satellite PRN22, indicating that once a solution for removing the bias is found, the quality will be sufficient for NWP assimilation. When the vertical structure of the airborne profiles are compared with the ECMWF profiles, it is clear that the airborne measurements are reliably resolving the variations associated with the tropopause, as well as recovering the height levels of sharp refractivity gradients.

The retrieved refractivity decreases greatly relative to ECMWF below 4 km. We believe this is due to the limitations of the geometric optics Abel inversion. This was also a problem for spaceborne radio occultation prior to the development of techniques such as Full Spectrum Inversion (FSI) for dealing with multipath propagation in the lower atmosphere due to strong moisture gradients. A significant development effort is required to implement more advanced inversion techniques such as FSI for the airborne case because of the geometry, but this effort is underway.

Large observation errors are typically assigned to spaceborne RO data during assimilation below 5 km altitude [Beyerle et al., 2004]. This is because even using the FSI technique, the spaceborne RO profiles have an unresolved negative bias of $1 - 1.5$ % with respect to ECMWF below 2 km altitude [Gorbunov and Shmakov, 2011]. In addition, the techniques for assimilating GPS RO observations in the presence of horizontal gradients that violate the assumption of spherical symmetry have been developed but are still being tested. With the dense datasets that can now be provided by airborne RO consistently down to lower than 1 km, there will be much more data available for advancing assimilation techniques in the lower tropopause. This quantitative analysis of the airborne RO capabilities and demonstration of the sensitivity of the technique to synoptic scale variations in the vertical structure suggests that the measurements can potentially make a valuable contribution to regional NWP in the future. What is learned from the analysis of radio occultation data about signal tracking and retrieval in the lower parts of the atmosphere will benefit the larger community, as many of these aspects are problematic in the spaceborne

RO measurements as well. The airborne system will be able to provide high vertical and temporal resolution profiles in targeted studies, and could eventually lead to development of an operational system on commercial aircraft

BIBLIOGRAPHY

BIBLIOGRAPHY

Acikoz, U. (2011). Open-loop tracking of rising gps radio occultation signals. Master's thesis, Purdue University.

Alban, S., Akos, D., and et al (2003). Performance analysis and architectures for INS-aided GPS tracking loops. *Proceedings of ION National Technical Meeting*, ION-NTM 2003. Anahiem, CA.:pp. 611–622.

Anthes, R. A., Rocken, C., and Kuo, Y. H. (2000). Applications of COSMIC to meteorology and climate. *Terrestrial Atmospheric And Oceanic Sciences*, 11(1):115–156. 1017-0839.

Ao, C., Hajj, G., Meehan, T.K. andDong, D., Iijima, B., Mannucci, A., and Kursinski, E. (2009). Rising and setting gps occultations by use of open-loop tracking. *Journal of Geophysical Research*, 114, D04101:DOI:10.1029/2008JD010483.

Ao, C., Meehan, T., Hajj, G., Manucci, A., and Beyerle, G. (2003). Lower troposphere refractivity bias in gps occultation retrievals. *Journal of Geophysical Research*, 108:doi: 10.1029/2002JD003216.

Aparicio, J. M., Deblonde, G., Garand, L., and Laroche, S. (2009). Signature of the atmospheric compressibility factor in cosmic, champ, and grace radio occultation data. *Journal of Geophysical Research*, 114:doi:10.1029/2008JD011156.

Aumann, H. H., Chahine, M. T., Gautier, C., Goldberg, M. D., Kalnay, E., McMillin, L. M., Revercomb, H., Rosenkranz, P. W., Smith, L. W., Staelin, D. H., Larabe Strow, L., and Susskind, J. (2003). Airs/amsu/hsb on the aqua mission: Design, science objectives, data products, and processing systems. *IEEE Transactions on Geoscience and Remote Sensing*, 41(2):253–264.

Baker, N. L., Hogan, T. F., Campbell, W. F., Pauley, R. L., and Swadley, S. D. (2005). The impact of amsu-a radiance assimilation in the us navy's operational global atmospheric prediction system. *Naval Research Laboratory*, NRL/MR/7530–05-8836:Monterey, CA.

Bevis, M., Businger, S., Chiswell, S., Herring, T. A., Anthes, R. A., Rocken, C., and Ware, R. H. (1994). Gps meteorology: mapping zenith wet delays onto precipitable water. *Journal of applied meteorology*, 33(3):379–386.

Beyerle, G., Ramatschi, M., Galas, R., Schmidt, T., Wickert, J., and Rothacher, M. (2009). A data archive of gps navigation messages. *GPS Solutions*, 13(1):35041.

Beyerle, G., Schmidt, T., Wickert, J., Heise, S., Rothacher, M., Konig-Langlo, G., and Lauritsen, K. B. (2006). Observations and simulations of receiver-induced refractivity biases in gps radio occultation. *Journal of Geophysical Research*, doi:10.1029/2005JD006673.

Beyerle, G., Wickert, J., Schmidt, T., and Reigber, C. (2004). Atmospheric sounding by gnss radio occultation: An analysis of the negative refractivity bias using champ observations. *Journal of Geophysical Research*, 109(doi:10.1029/2003JD003922).

Born, M. and Wolf, E. (1964). *Principles of Optics: Electromagnetic Theory of Propagation, Interference adn Diffraction of Light*. Pergamon Press.

Braasch, M. S. (1999). GPS Receiver architectures and measurements. *Proceedings of the IEEE*, 87(1):48–64.

Buck, A. L. (1981). New equations for computing vapor pressure and enhancement factor. *J. Appl. Meteor.*, 20:1527–1532.

Cardinali, C. and Prates, F. (2011). Performance measurement with advanced diagnostic tools of all-sky microwave imager radiances in 4d-var. *Quarterly Journal of the Royal Meteorological Society*, 137:2038–2046.

Collard, A. D. and Healy, S. B. (2003). The combined impact of future space-based atmospheric sounding instruments on numerical weather prediction analysis fields: A simulation study. *Quarterly Journal of Royal Meteorological Society*, 129:2741–2760.

Cucurull, L. (2007). Assimilation of GPS RO into NCEP global data assimilation system. *Monthly weather review*, 135:3174–3193.

Cucurull, L. (2010). Improvement in the use of an operational constellation of gps radio occultation receivers in weather forecasting. *Weather and Forecasting*, 25:749–767.

de La Beaujardiere, O. Retterer, J. M., Kelley, M. C., Hunton, D., and Jeong, L. (2004). A mission to forecast scintillations. *Journal of Atmospheric and Solar-Terrestrial Physics*, 66(17):1573.

Easterling, D. R., Evans, J. L., and Groisman, P. Y. (2000). Observed variability and trends in extreme climate events. *Bulletin of American Meteorological Society*, 81:417–425.

Ebi, L. K. and Schmier, K. (2000). A stitch in time: Improving public health. early warning systems for extreme weather events. *Bulletin of American Meteorological Society*, 81:417–425.

Fjeldbo, G., Kliore, A., and Eshleman, V. (1971). The Neutral atmosphere of venus as studied with the Mariner V radio occultation experiments. *Astronomical Journal*, 76(2):123–140.

Foelsche, U., Borsche, M., Steiner, A. K., Gobiet, A., Pirscher, B., Kirchengast, G., Wickert, J., and Schmidt, T. (2007). Observing upper troposphere-lower stratosphere climate with radio occultation data from the champ satellite. *Climate Dynamics*, 31:49–65.

Garrison, J. L., Walker, M., Haase, J., Lulich, T., Xie, F., Ventre, B. D., Boehme, M., Wilmhoff, B., and Katzberg, S. J. (2007). Development and Testing of the GISMOS Instrument. In IEEE, editor, *IEEE International Geoscience and Remote Sensing Symposium*, Barcelona, Spain.

Gelaro, R. (2009). Recent developments in the use and understanding of adjoint-derived estimates of observation impact in nwp. In *8th Workshop on Adjoint Model Applications in Dynamic Meteorology*.

Gelaro, R. (2011). Geos-5 data assimilation and forecast impacts for concordiasi. In *Fourth meeting of the THORPEX DAOS Working Group, Exeter, UK*.

Gorbunov, M. E. and Shmakov, A. V. (2011). Cosmic radio occultation processing: cross-center comparison and validation. *Journal of atmospheric and oceanic technology*, 28:737–751.

GRAS-SAG, E. (1998). Report of the GRAS-SAG: The GRAS instrument on METOP. Technical report, EUMETSAT.

Greenough, G., McGeehin, M., Bernard, S., Trtanj, J. Riad, J., and Engelberg, D. (2001). The potential impacts of climate variability and change on he alt impacts of extreme weather events in the united states. *Environmental Health Perspectives*, 109(2).

Haase, J. S., Maldonado-Vargas, J., Rabier, F., Cocquerez, P., Minois, M., Guidard, V., Wyss, P., and Johnson, A. V. (2012). A proof of concept baloon-borne GPS radio occultation profiling instrument for polar studies. *Geophysical Research Letters*, 39:L02803.

Hajj, G. A., Ao, C. O., Iijima, B. A., Kuang, D., Kursinski, E. R., Mannucci, A. J., Meehan, T. K., Romans, L. J., Juarez, M. D., and Yunck, T. P. (2004). CHAMP and SAC-C atmospheric occultation results and intercomparisons. *Journal Of Geophysical Research-Atmospheres*, 109(D6). D06109.

Hajj, G. A., Kursinski, E. R., Romans, L. J., Bertiger, W. I., and Leroy, S. S. (2002). A technical description of atmospheric sounding by GPS occultation. *Journal of Atmospheric and Solar-Terrestrial Physics*, 64(4):451–469.

Healy, S. B. (2011). Refractivity coefficients used in the assimilation of gps radio occultation measurements. *Journal of Geophysical Research*, 116:doi:10.1029/2010JD014013.

Healy, S. B., Haase, J., and Lesne, O. (2002). Abel transform inversion of radio occultation measurements made with a receiver inside the Earth's atmosphere. *Annales Geophysicae*, 20(8):1253–1256. paper copy Letter 583XP ANN GEOPHYS.

Healy, S. B. and Thepaut, J. N. (2006). Assimilation experiments with champ gps radio occultation measurements. *Quarterly Journal of Royal Meteorological Society*, 132:605–623.

Heckler, G. W. and Garrison, J. L. (2004). Architecture of a reconfigurable software receiver. *In Proc. ION GNSS*, pages 947–955.

Hilton, F., Atkinson, N. C., English, S. J., and Eyre, J. R. (2009). Assimilation of iasi at the met office and assessment of its impact through observing system experiments. *Quarterly Journal of the Royal Meteorological Society*, 135:495–505.

Hirshberg, P. and Fritsch, M. (1990). Tropopause undulations and the development of extratropical cyclones: Overview and observations from a cyclone event. *Monthly Weather Review*, 119:496–517.

Hofmann-Wellenhof, B. Lichtenegger, H. and Collins, J. (2001). GPS: Theory and Practice. *5th Edition, Springer-Verlag Wien*, pages New York, NY, pp. 235–237.

Huang, C. Y., Kup, Y. H., Chn, S., Terng, C. T., Chien, F. C., Lin, P. L., Kueh, M. T., Chen, S. H., Yang, M. J., and Wang, C. J. (2010). Impact of GPS radio occultation data assimilation on regional weather predictions. *GPS Solutions*, 14(1):35–49.

Hutton, J., Alan, I., Bourke, T., Scherzinger, B., Gopaul, N., Canter, P., Overland, I., and Blankenberg, L. (2008). Tight integration of gnss post-processed virtual reference station with inertial data for increased accuracy and productivity of airborne mapping. *The International Archives of the Photogrammetry, Remote Sensing and Spatial Information Sciences*, 37(B5).

Janjic, Z. (1990). The step-mountain coordinate - physical package. *Monthly Weather Review*, 118:1429–1443.

Jensen, A. S., Lohmann, M. S., Benzon, H. H., and Nielsen, S. (2003). Full spectrum inversion of radio occultation signals. *Radio Science*, 38:1048.

Kim, K., Jung, E., and Campistron, B. (2001). A physical examination of tropopause height and stratospheric air intrusion: A case study. *Journal of Meteorological Society of Japan*, 79(5):1093–1103.

Kirchengast, G., Hafner, J., and Poetzi, W. (1999). The cira86aq uog model: An extension of the cira-86 monthly tables including humidity tables and fortran95 global moist air climatology model. *IMG/UoG Techn Rep 8*, Eur Space Agency:Paris, France.

Kleist, D. T., Parrish, D., Derber, J. C., Treadon, R., Wu, W. S., and Lord, S. (2009). Introduction of the gsi into the nceps global data assimilation system. *Weather and Forecasting*, 24:1691–1705.

Kuo, Y. H., Wee, T. K., Sokolovskiy, S., Rocken, C., Schreiner, W., and Hunt, D. (2004). Inversion and error estimation of gps radio occultation data. *Journal of the Meteorological Society of Japan*, 82(1B):507–531.

Kursinski, E. R. and Hajj, G. A. (2001). A comparison of water vapor derived from gps occultations and global weather analyses. *Journal of Geophysical Research-Atmospheres*, 106(D1):1113–1138.

Kursinski et al. (1996). Initial results of radio occultation observations of Earth's atmosphere using the Global Positioning System. *Science*, 271:1107–1110.

Langland, R. H., Toth, Z., Gelaro, R., Szunyogh, I., Shapiro, M. A., Majumdar, S. J., Morss, R. E., Rohaly, G. D., Velden, C., Bond, N., and Bishop, C. H. (1999). The north pacific experiment (norpex-98): Targeted observations for improved north american weather forecasts. *Bulletin of the American Meteorological Society*, 80(7):1363–1384.

Lesne, O., Haase, J., Kirchengast, G., Ramsauer, J., and Poetzi, W. (2000). GNSS Radio occultation for airborne sounding of the troposphere. In *EGS General Assembly*, volume submitted, Nice. EGS.

Lesne, O., Haase, J., Kirchengast, G., Ramsauer, J., and Poetzi, W. (2002). Sensitivity analysis for airborne sounding of the troposphere by GNSS radio occultation. *Phys. Chem. Earth*, 27:291–299.

Liu, H., Anderson, J., and Kuo, Y. H. (2012). Improved analysis and forecasts of hurricane ernesto's genesis using radio occultation data in an ensemble filter assimilation system. *Monthly Weather Review*, 140:151–166.

Lulich, T. D., Garrison, J. L., Haase, J. S., Yang, Y. M., Voo, J., Xie, F., and Muradyan, P. (2010). Open loop tracking of radio occultation signals from an airborne platform. In 21-24, S., editor, *Proceedings of the 23rd International Technical Meeting of the Satellite Division of the Institute of Navigation*, Portland, OR.

Luntama, J. P., Kirchengast, G., Borsche, M., Foelsche, U., Steiner, A., Healy, S., von Engeln, A., O'Clerigh, E., and Marquardt, C. (2008). Prospects of the eps gras mission for operational atmospheric applications. *Bulletin of American Meteorological Society*, 89(12):1863–1875.

McNally, A. P., Watts, P. D., and Smith, J. A. (2006). The assimilation of airs radiance data at ecmwf. *European Centre for Medium-range Weather Forecasts Readings*, RG2-9AX:UK.

Misra, P. and Enge, P. (2001). *Global Positioning System: Signals, Measurements, and Performance*. Ganga-Jamuna Press, Lincoln, Mass.

Mostafa, M., Hutton, J., and Reid, B. (2001). GPS/IMU products- the Applanix approach. *Proceedings of the 48th Photogrammetric Week*.

Muradyan, P., Haase, J., Xie, Garrison, J. L., and Voo, J. (2010). Gps/ins navigation precision and its effect on airborne radio occultation retrieval accuracy. *GPS Solutions*, pages DOI:10.1007/s10291–010–0183–7.

Murphy, D. and Koop, T. (2005). Review of the vapor pressures of ice and supercooled water for atmospheric applications. *Q. J. R. Meteor. Soc.*, 131:1539–1565.

Murray, F. W. (1966). On the computation of saturation vapor pressure. *Journal of applied meteorology*, 6:203–204.

Osuri, K. K., Routray, A., Mohanty, U. C., and Kukarni, M. A. (2010). *Simulation of tropical cyclones over Indian Seas: Data impact study using WRF-Var assimilation system*. Centre for Atmospheric Sciences, Indian Institue of Technology, New Delhi.

Pan, L. L., Randel, W. J., Gary, B. L., Mahoney, J., and Hintsa, E. (2008). Definitions and sharpness of the extratropical tropopause: A trace gas perspective. *Journal of Geophysical Research*, 109(D23103).

Perona, G., Notarpietro, R., and Gabella, M. (2007). Gps radio occultation on-board the oceansat-2 mission: an indian (isro)-italian (asi) collaboration. *Indian Journal of Radio Space Physics*, 36:386–393.

Poli, P., Healy, S. B., and Dee, D. (2010). Assimilation of global positioning system radio occultation data in the ecmwf era- interim reanalysis. *Quarterly Journal of the Royal Meteorological Society*, 136:1972–1990.

Poli, P., Healy, S. B., Rabier, F., and Pailleux, J. (2008). Preliminary assessment of the scalability of gps radio occultations impact in numerical weather prediction. *Geophysical Research Letters*, 35(L23811).

Poli, P., Joiner, J., and Kursinski, E. R. (2002). 1dvar analysis of temperature and humidity using gps radio occultation refractivity data. *Journal Of Geophysical Research-Atmospheres*, 107(D20). 4448.

Rabier, F., Gauthier, P., Cardinali, C., Langland, R., Tsyrulnikov, M., Lorenc, A., Steinle, P., Gelaro, R., and Koizumi, K. (2008). An update on thorpex-related research in data assimilation and observing strategies. *Nonlin. Processes Geophys.*, 15:81–94.

Rennie, M. P. (2010). The impact of gps radio occultation assimilation at the met office. *Quarterly Journal of the Royal Meteorological Society*, 136:116–131.

Rocken, C., Anthes, R., Exner, M., Hunt, D., Sokolovskiy, S., Ware, R., Gorbunov, M., Schreiner, W., Feng, D., Herman, B., Kuo, Y.-H., and Zou, X. (1997). Analysis and validation of GPS/MET data in the neutral atmosphere. *J. Geophys. Res.*, 102:29849–29866.

Schafer, R. W. (2011). What is a savitzky-golay filter? *IEEE Signal Processing Magazine*, pages 111–117.

Schenewerk, M. (2003). A brief review of basic gps orbit interpolation strategies. *GPS Solutions*, 6:265–267.

Schmidt, T., Wickert, J., Beyerle, G., and Heise, S. (2008). Global tropopause height trends estimated from gps radio occultation data. *Geophysical Research Letters*, 35(L11806).

Schreiner, W., Rocken, C., Sokolovskiy, S., Syndergaard, S., and Hunt, D. (2007). Estimates of the precision of GPS radio occultations from the COSMIC/FORMOSAT-3 mission. *Geophysical Research Letters*, 34(4). 0094-8276 L04808.

Seidel, D. J., Angel, J. K., Christy, J., Free, M., Klein, S. A., Lanzante, J. R., Mears, C., Parker, D., Schabel, M., Spencer, R., Sterin, A., Thorne, P., and Wentz, F. (2004). Uncertainty in signals of large scale climate variations in radiosonde and satellite upper air temperature datasets. *Journal of Climate*, 17:2225–2240.

Shapiro, M. A. and Thorpe, A. J. (2004). Thorpex international science plan. *World Meteorological Organization*, TD-No 1246.

Simeoni, D. and Singer, C. (1999). Infrared atmospheric sounding interferometer. *Acta Astronautica*, 40(2):113–118.

Sokolovskiy, S. (2001). Tracking tropospheric radio occultation signals from low Earth orbit. *Radio Science*, 36(3):483–498.

Sokolovskiy, S., Rocken, C., Hund, D., Schreiner, W., Johnson, J., and Masters, D. (2006). Gps profiling of the lower troposphere from space: Inversion and demodulation of the open-loop radio occultation signals. *Geophysical Research Letters*, 33:L14816.

Sokolovskiy, S., Rocken, C., Schreiner, W., and Hunt, D. (2010). On the uncertainty of radio occultation inversions in the lower troposphere. *Journal of Geophysical Research*, 115(D22111):doi:10.1029/2010JD014058.

Steiner, A., Kirchengast, G., and Ladreiter, H. (1999). Inversion, error analysis, and validation of gps/met occultation data. *Ann. Geophysicae*, 17:122–138.

Syndergaard, S. (1998). Modeling the impact of the Earth's oblateness on the retrieval of temperature and pressure profiles from limb sounding. *Journal of Atmospheric and Solar-Terrestrial Physics*, 60(2):171–180.

Syndergaard, S. (2000). On the ionosphere calibration in GPS radio occultation measurements. *Radio Science*, 35(3):865–883.

Szunyogh, I., Toth, Z., Zimin, A., Majumdar, S. J., and Persson, A. (2001). Propagation of the effect of targeted observations: The 2000 winter storm reconnaissance program. *Monthly Weather Review*, 130:1144–1164.

Thayer, R. (1974). An improved equation for the radio refractive index of air. *Radio Science*, 9:803–807.

Turner, D. D., Linne, H., Bosenberg, J., Lehmann, S., Ertel, K., Goldsmith, J., and Tooman, T. P. (2000). Simultaneous ground-based remote sensing of water vapor by differential absorption and Raman lidars. *Tenth ARM Science Team Meeting Proceedings*, San Antonio, Texas.

Vedel, H. (2001). Hirlam assimilation experiments with ground-based gps data at dmi. In Haase-ACRI-ST, J., editor, *MAGIC Water Vapor Meteorology User Workshop*, Barcelona (Spain). Cartographic Institute of Catalonia. magicpub.

Vedel, H., Mogensen, K., and Huang, X.-Y. (2001). Calculation of zenith delays from meteorological data, comparison of NWP model, radiosonde and GPS delays. *Phys. Chem. Earth (A)*, 26(6-8):497–502. magicpub.

Ventre, B. (2006). Open-loop tracking of an occulting gnss signal. Master's thesis, Purdue University.

von Engeln, A., Healy, S., Marquardt, C., Andres, Y., and Sancho, F. (2009). Validation of operational gras radio occultation data. *Geophysical Research Letters*, 36:doi:10.1029/2009GL039968.

Vorobev, V. and Krasilnikova, T. (1994). Estimation of the accuracy of the atmospheric refractive index recovery from Doppler shift measurements at frequencies used in the NAVSTAR system. *Physics of the Atmosphere and Ocean (English Translation)*, 29(5):602–609.

Waliser, D. and Moncrieff, M. (2007). Year of tropical convection: Joint wcrp-thorpex activity to address the challenge of tropical convection. *WCRP GEWEX News*, 17(2):8.

Ware, R., Exner, M., Feng, D., Gorbunov, M., Hardy, K., Herman, B., Kuo, Y., Meehan, T., Melbourne, W., Rocken, C., Schreiner, W., Sokolovskiy, S., Solheim, F., Zou, X., Anthes, A., Businger, S., and Trenberth, K. (1996). Gps sounding of the atmosphere from low earth orbit: preliminary results. *Bull. Am. Meteor. Soc.*, 77(1):19–40.

Wee, T. K. and Kuo, Y. H. (2008). Assimilation of gps radio occultation refractivity data from champ and sac-c missions over high southern latitudes with mm5 4dvar. *Monthly Weather Review*, 136:2923–2944.

Werninghaus, R., Balzer, W., Buckreuss, S., Mittermayer, J., and Muhlbauer, P. (2004). The terrasar-x mission. *EUSAR*, pages Ulm, Germany.

Wickert, J., Beyerle, G., Heise, S., Grunwaldt, L., Michalak, G., Reigber, C., and Schmidt, T. (2005). Gps radio occultation with champ and grace: A first look at a new and promising satellite configuration for global atmospheric sounding. *Annales Geophysicae*, 23:653–658.

Xie, F., Haase, J., and Syndergaard, S. (2008). Profiling the atmosphere using the airborne gps radio occultation technique: A sensitivity study. *Trans. IEEE Geosci.and Remote Sens.*, 46 (11):3424–3435, DOI:1–.1109/TGRS.2008.2004713.

Yang, W., Cao, W., and Chung, T. S. (2005). *Applied numerical methods using Matlab* . Willey, New York.

Yoshihara, T., Fujii, N., Hoshinoo, K., Matsunaga, K., Saitoh, S., Sakai, T., Tsuda, T., Aoyama, Y., and Danno, S. (2004). Airborne gps down-looking occultation experiments. *Proc. Institute of Navigation*, pages 1713–1723.

Yunck, T. P., Lindal, G. F., and Liu, C. (1988). The role of GPS in precise Earth observation. *IEEE Position, Location and Navigation Symposium*, Orlando, FL:Nov. 29–Dec. 2.

Zuffada, C., Hajj, G., and Kursinski, E. R. (1999). A novel approach to atmospheric profiling with a mountain-based or airborne GPS receiver. *J. Geoph. Res.*, 104(D20):24435–24447.

Zus, S., Beyerle, G., Heise, S., Schmidt, T., Wickert, J., and Marquardt, C. (2011). Validation of refractivity profits derived from GRAS raw-sampling data. *Atmospheric Measurements Techniques Discussions*, 4:1825–1852.

APPENDICES

Appendix A: Full radio occultation data set

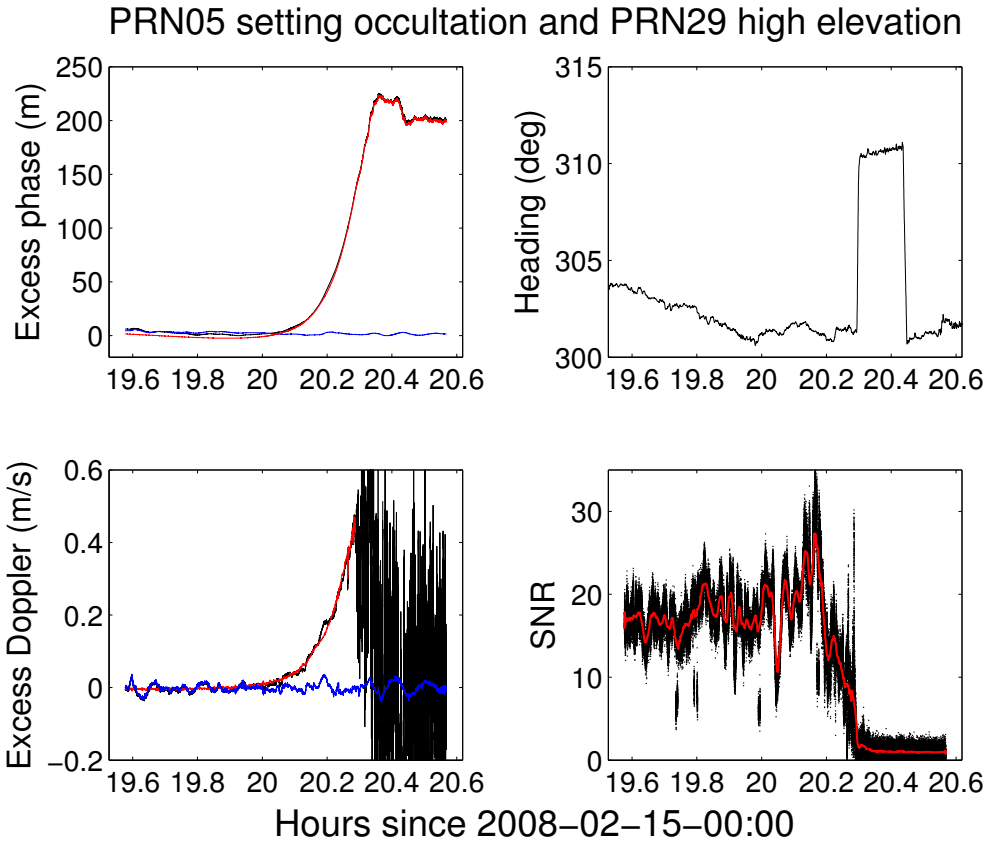

Figure A.1.: Excess phase (top left panel) and excess Doppler (bottom left) profiles for setting PRN05 and high elevation PRN29 satellites and their difference. The airplane turn at about 20.3 decimal hour (top right) causes loss of PRN05 signal.

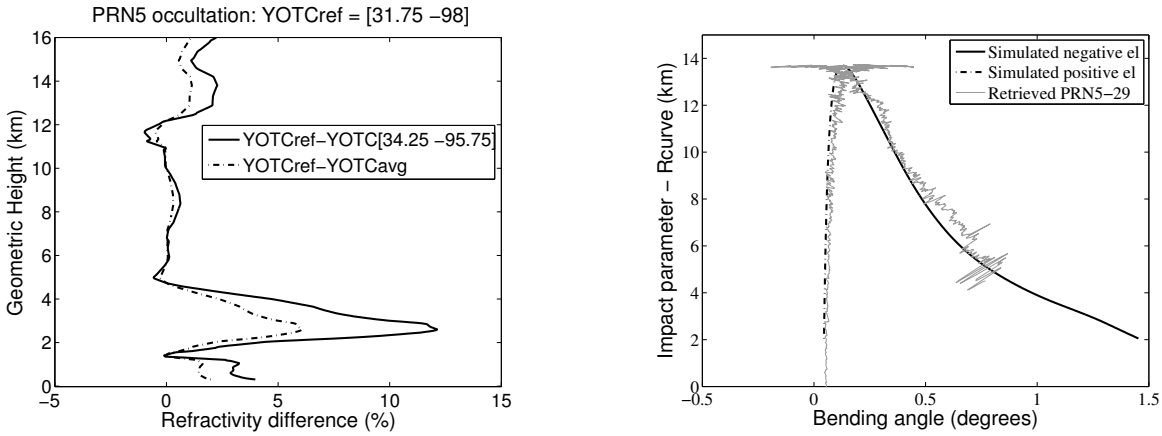

Figure A.2.: The reference refractivity profile for comparison with PRN05 occultation case is retrieved for 18Z and at a grid point [Lat Lon] = [31.7500 -98.000] (Left). Observed (gray) bending angle for PRN05 and simulated bending from CIRA-Q model profile at Lat = 34.2.

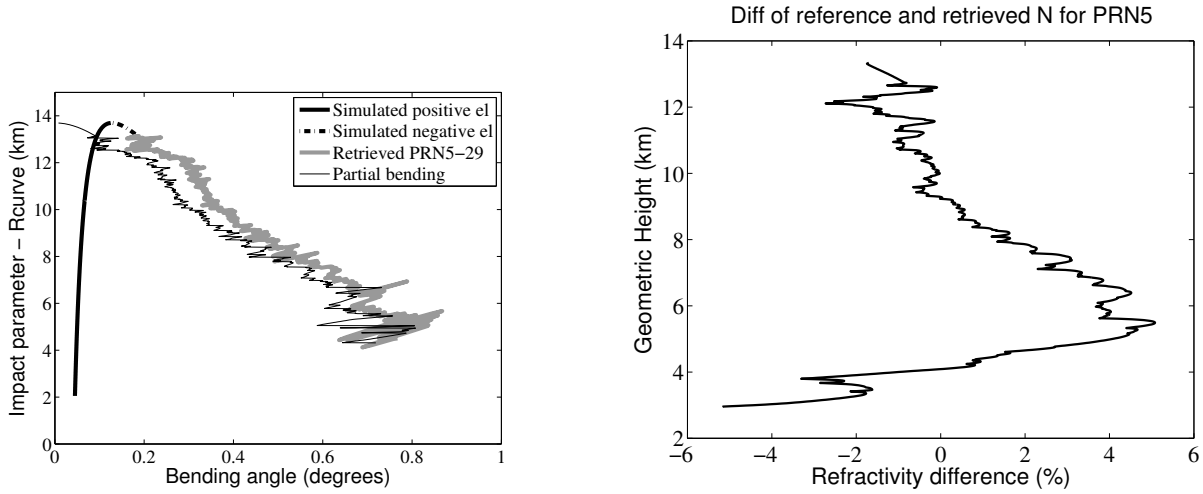

Figure A.3.: PRN05 observed bending is replaced with a simulated profile (solid and dashed black lines) for the positive elevation angle bending and the top 1 km of the negative elevation angle bending (gray line on left). Percent difference of retrieved and YOTC reference refractivity profiles.

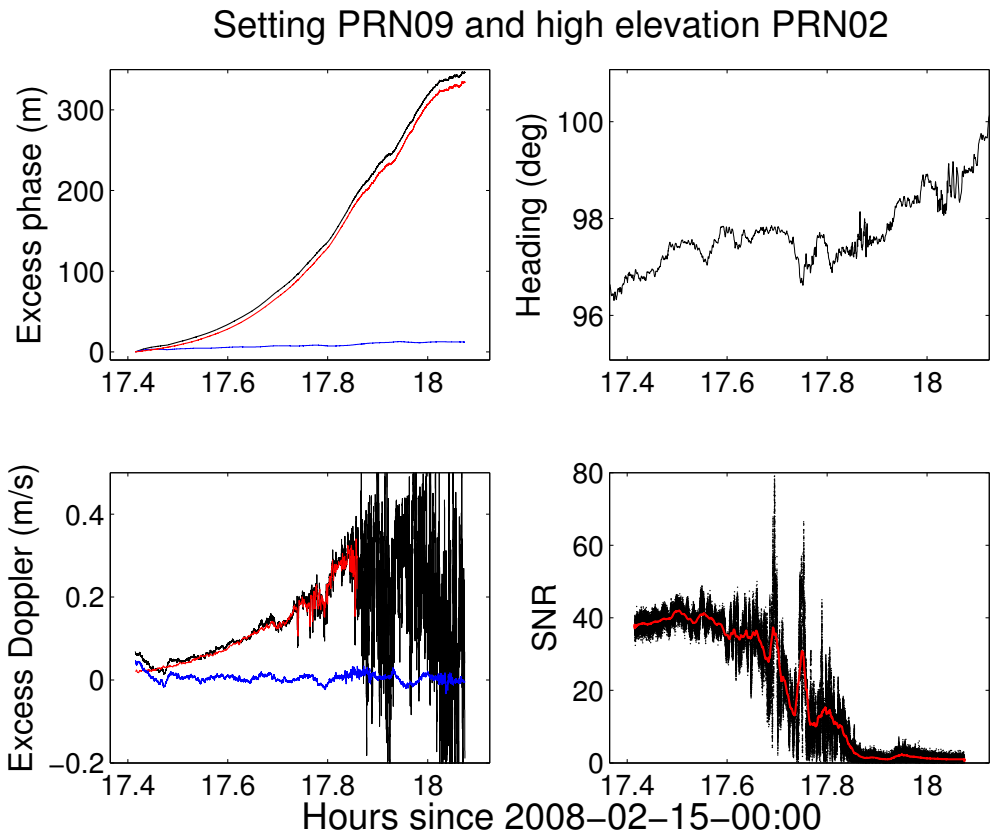

Figure A.4.: Excess phase (top left panel) and excess Doppler (bottom left) profiles for setting PRN09 and high elevation PRN02 satellites and their difference. Airplane heading does not change significantly during the PRN09 occultation (top right panel). Bottom right panel shows the amplitude for PRN09 occulting satellite.

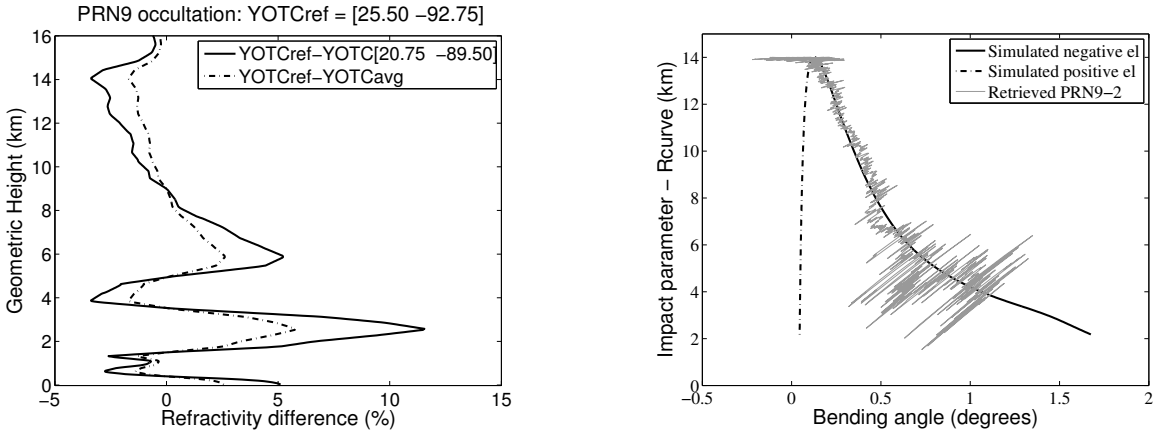

Figure A.5.: The reference refractivity profile for comparison with PRN09 occultation case is retrieved for 18Z and at a grid point [Lat Lon] = [25.5 -92.75] (Left). Observed (gray) bending angle for PRN09 and simulated bending from CIRA-Q model profile at Lat = 25.4.

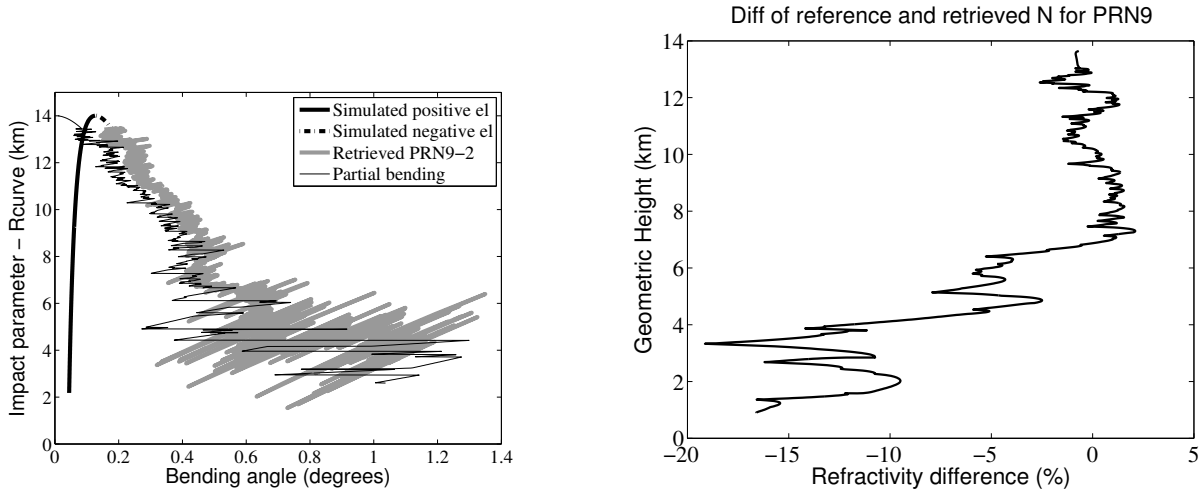

Figure A.6.: PRN09 observed bending is replaced with a simulated profile (solid and dashed black lines) for the positive elevation angle bending and the top 1 km of the negative elevation angle bending (gray line on left). Percent difference of retrieved and YOTC reference refractivity profiles.

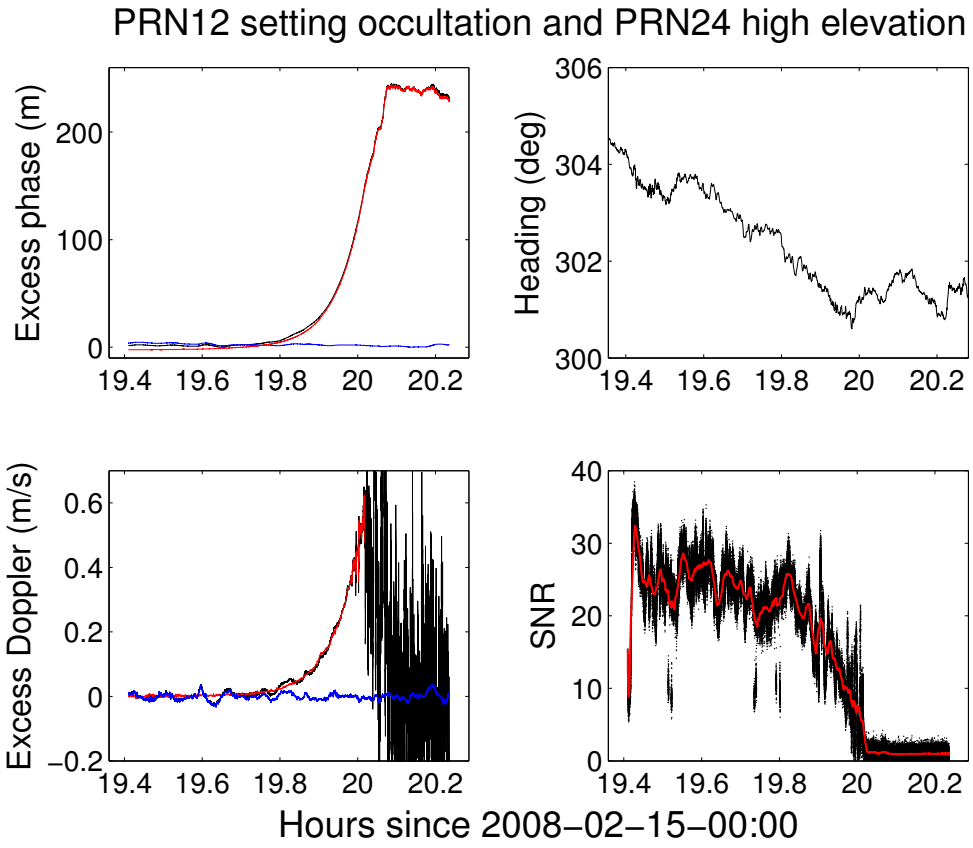

Figure A.7.: Excess phase (top left panel) and excess Doppler (bottom left) profiles for setting PRN12 and high elevation PRN24 satellites and their difference. Airplane heading does not change significantly during the PRN12 occultation (top right panel). Bottom right panel shows the amplitude for PRN12 occulting satellite.

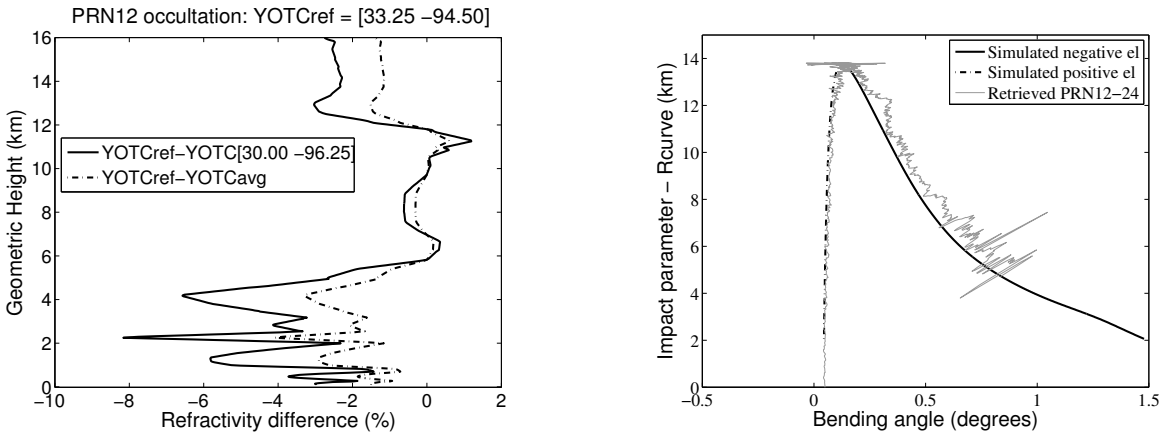

Figure A.8.: The reference refractivity profile for comparison with PRN12 occultation case is retrieved for 18Z and at a grid point [Lat Lon] = [33.25 -94.5] (Left).Observed (gray) bending angle for PRN12 and simulated bending from CIRA-Q model profile at Lat = 33.3.

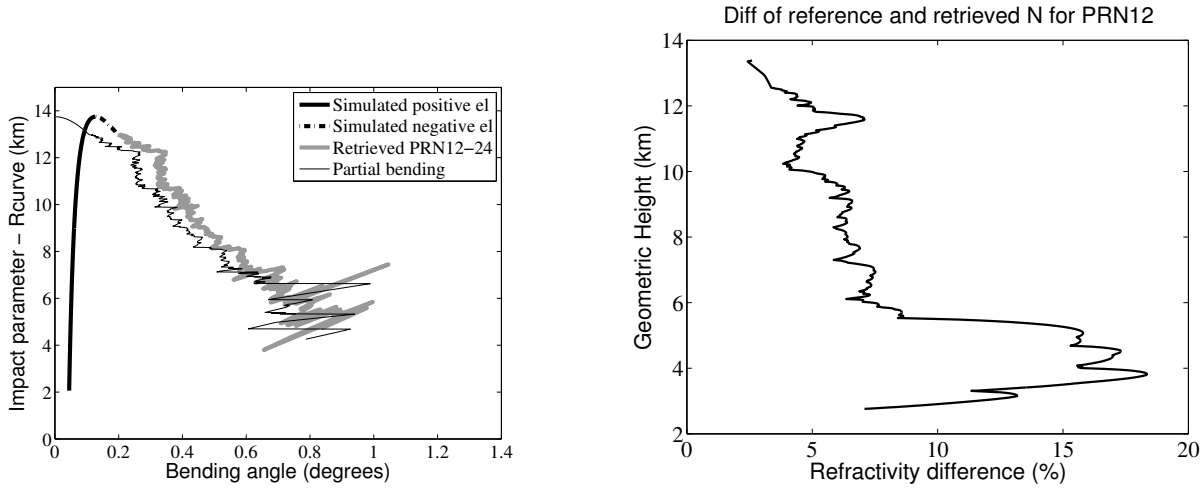

Figure A.9.: PRN12 observed bending is replaced with a simulated profile (solid and dashed black lines) for the positive elevation angle bending and the top 1 km of the negative elevation angle bending (gray line on left). Percent difference of retrieved and YOTC reference refractivity profiles.

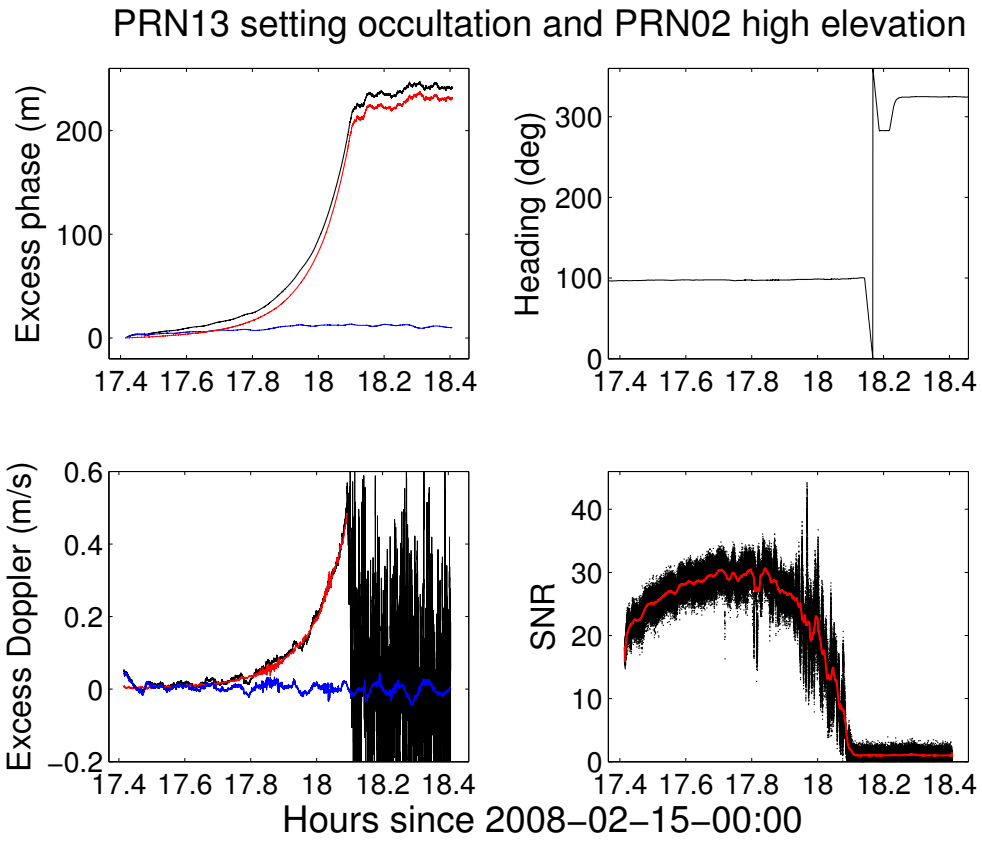

Figure A.10.: Excess phase (top left panel) and excess Doppler (bottom left) profiles for setting PRN13 and high elevation PRN02 satellites and their difference.

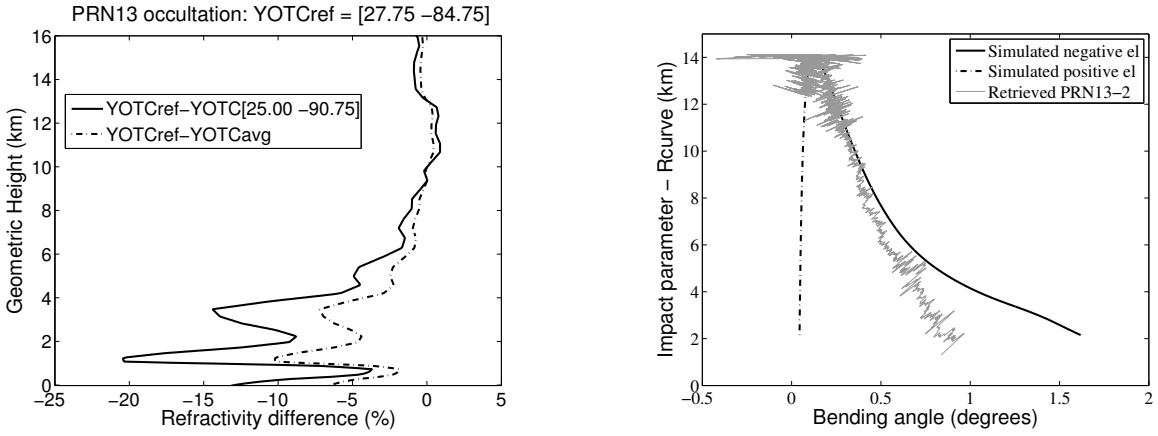

Figure A.11.: The reference refractivity profile for comparison with PRN13 occultation case is retrieved for 18Z and at a grid point [Lat Lon] = [27.75 -84.75] (Left). Observed (gray) bending angle for PRN13 and simulated bending from CIRA-Q model profile at Lat = 27.8

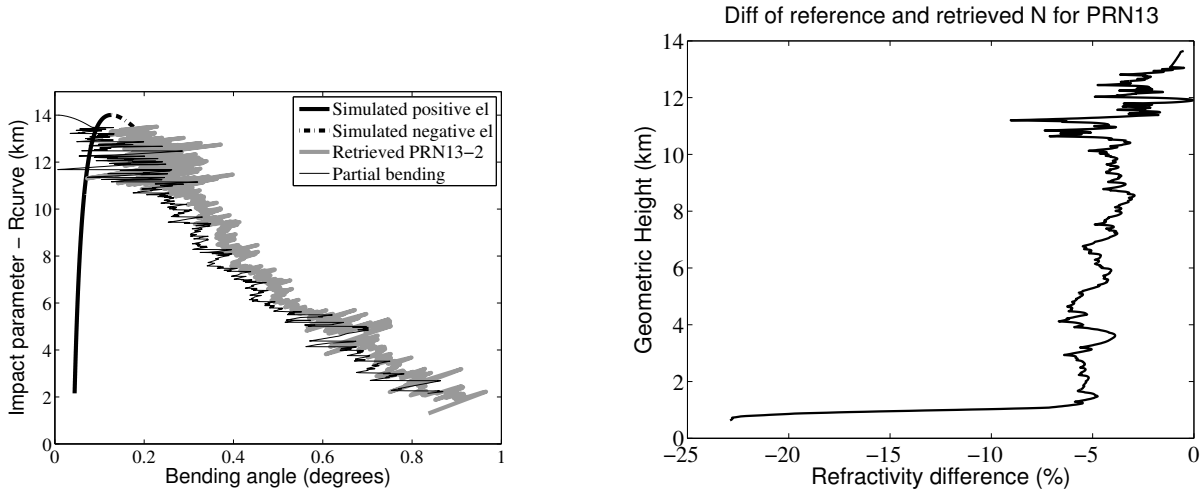

Figure A.12.: PRN13 observed bending is replaced with a simulated profile (solid and dashed black lines) for the positive elevation angle bending and the top 1 km of the negative elevation angle bending (gray line on left). Percent difference of retrieved and YOTC reference refractivity profiles.

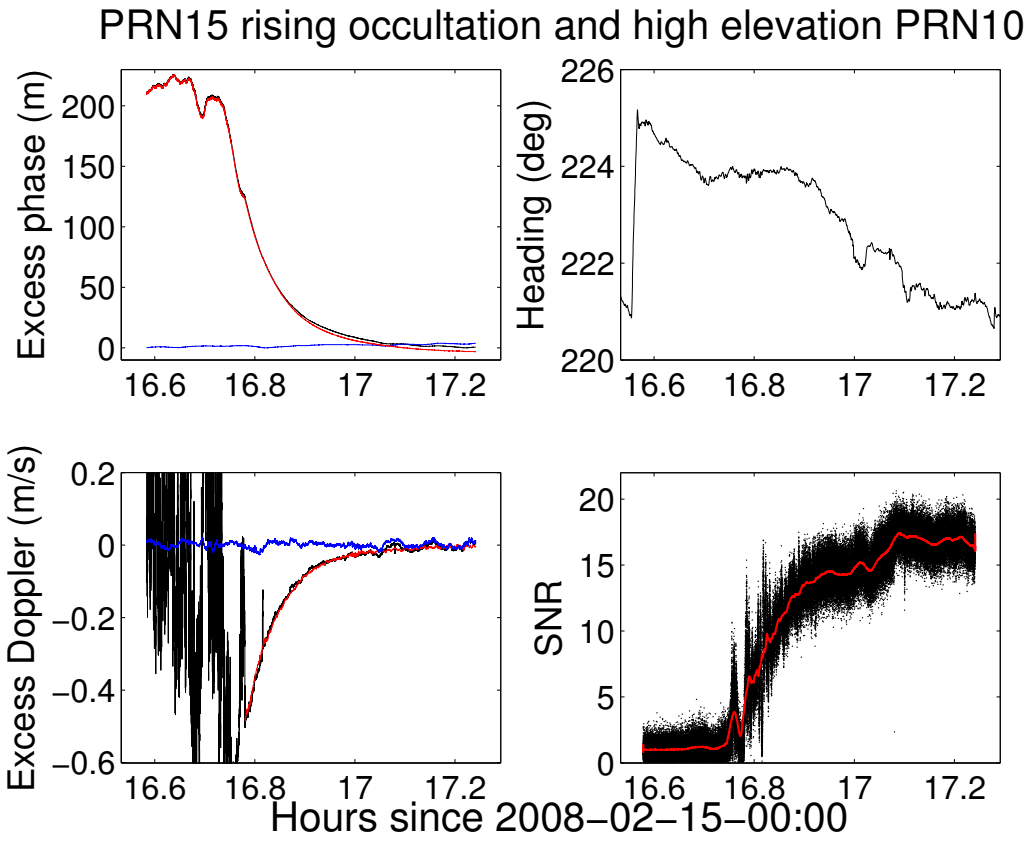

Figure A.13.: Excess phase (top left) and excess Doppler (bottom left) profiles for rising PRN15 and high elevation PRN10 satellites and their difference. Airplane heading does not change significantly during the PRN15 occultation period (top right). Bottom right panel shows the amplitude for PRN15 occulting satellite.

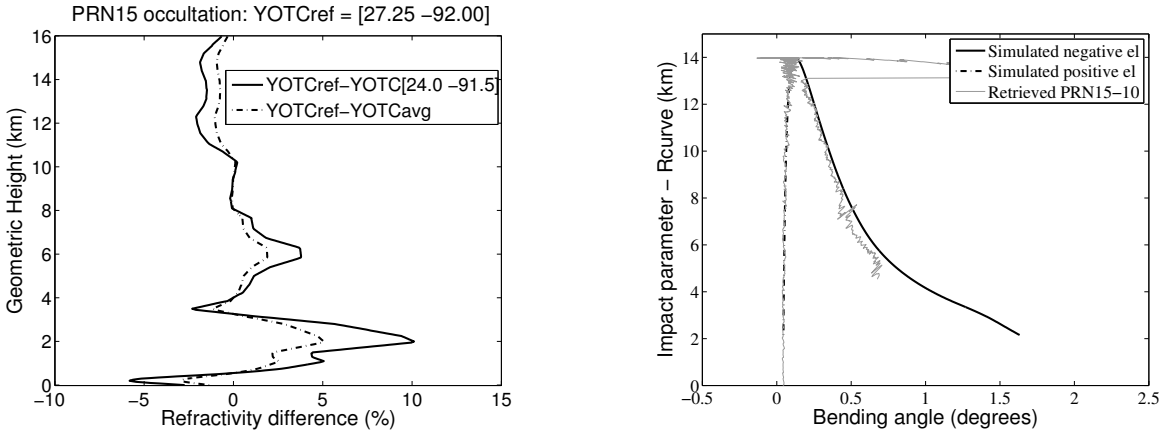

Figure A.14.: The reference refractivity profile for comparison with PRN15 occultation case is retrieved for 18Z and at a grid point [Lat Lon] = [27.2500 -92.000] (Left).Observed (gray) bending angle for PRN15 and simulated bending from CIRA-Q model profile at Lat = 27.2.

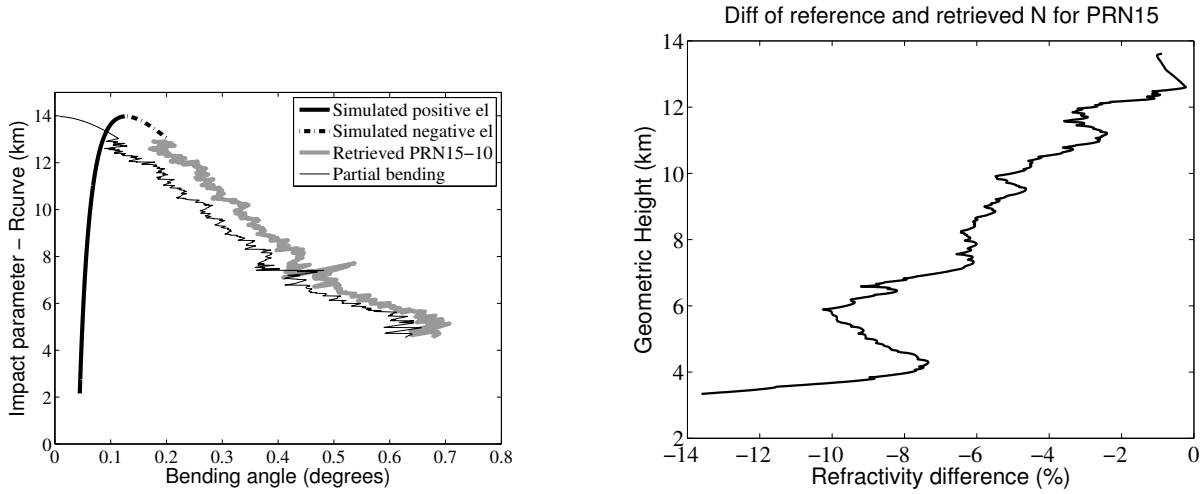

Figure A.15.: PRN15 observed bending is replaced with a simulated profile (solid and dashed black lines) for the positive elevation angle bending and the top 1 km of the negative elevation angle bending (gray line on left). Percent difference of retrieved and YOTC reference refractivity profiles.

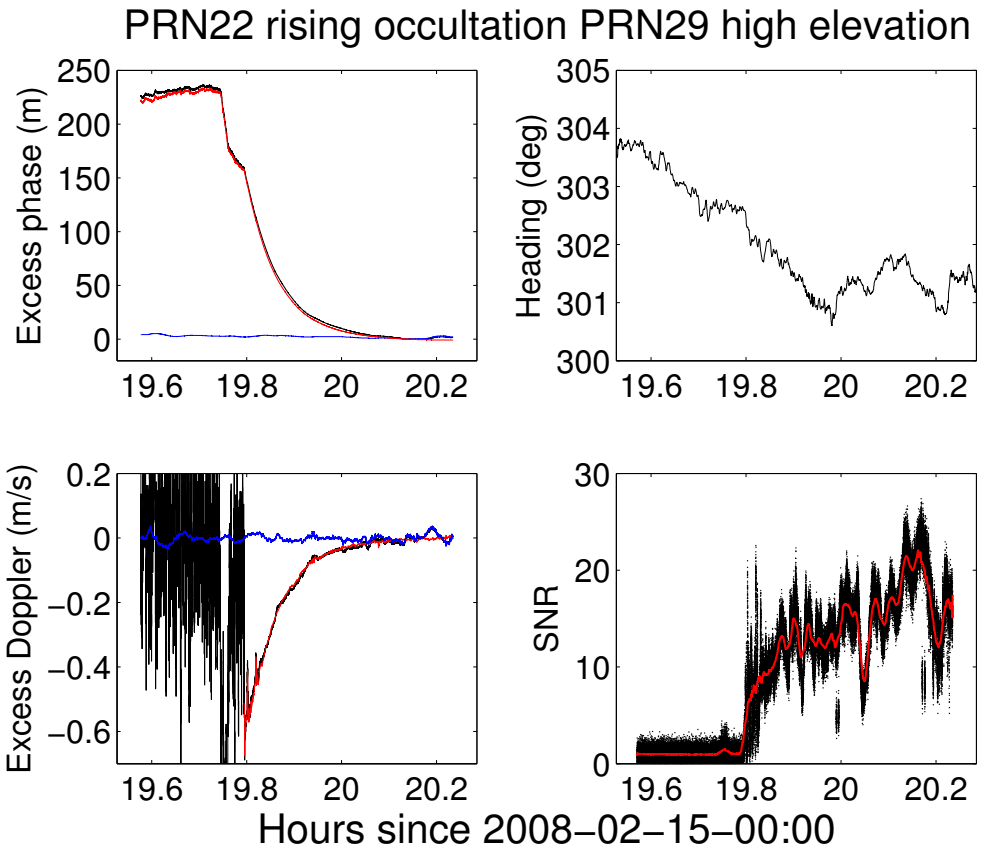

Figure A.16.: Excess phase (top left panel) and excess Doppler (bottom left) profiles for rising PRN22 and high elevation PRN29 satellites and their difference.

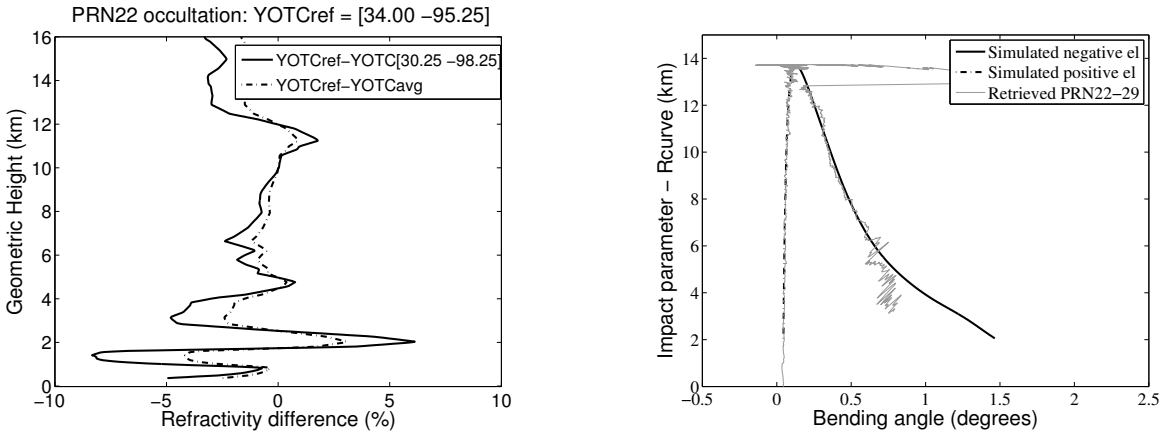

Figure A.17.: The reference refractivity profile for comparison with PRN22 occultation case is retrieved for 18Z and at a grid point [Lat Lon] = [34.00 -95.25] (Left). Observed (gray) bending angle for PRN22 and simulated bending from CIRA-Q model profile at Lat = 33.4

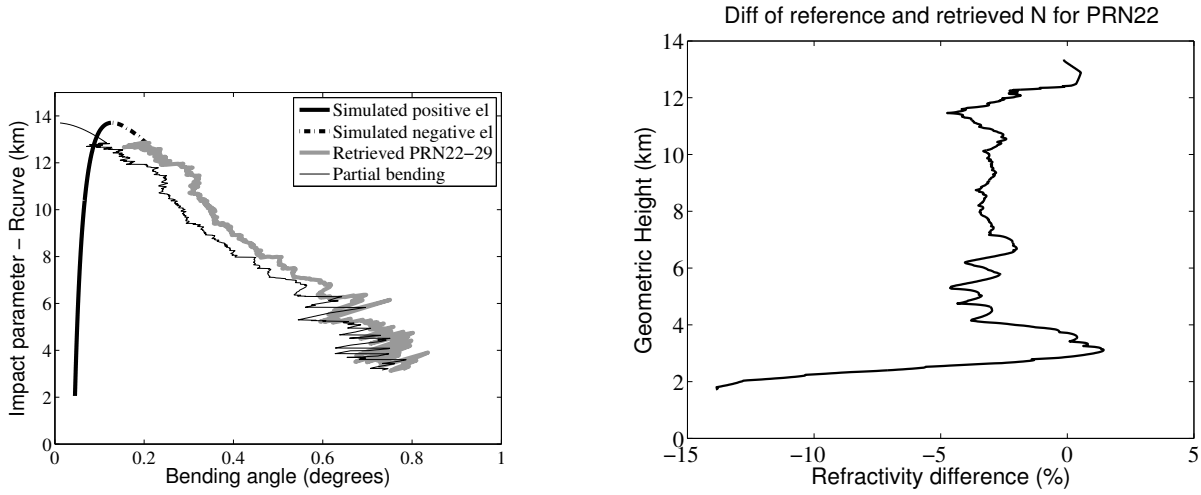

Figure A.18.: PRN22 observed bending is replaced with a simulated profile (solid and dashed black lines) for the positive elevation angle bending and the top 1 km of the negative elevation angle bending (gray line on left). Percent difference of retrieved and YOTC reference refractivity profiles.

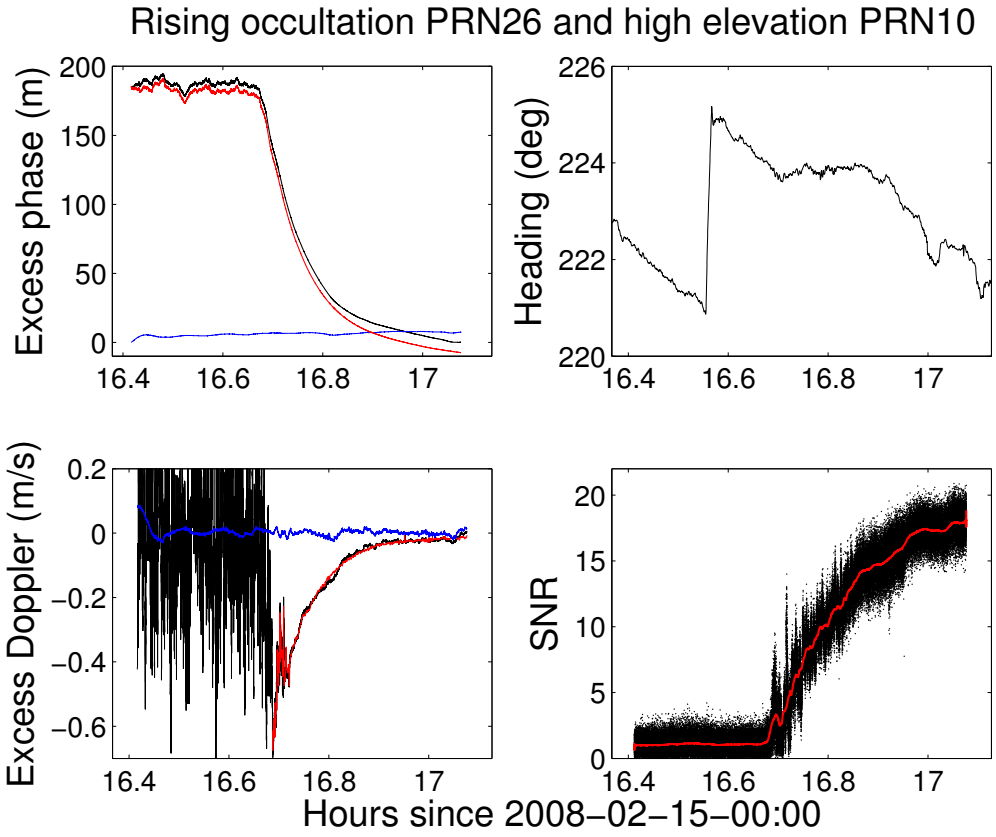

Figure A.19.: Excess phase (top left) and excess Doppler (bottom left) profiles for rising PRN26 and high elevation PRN10 satellites and their difference. Airplane heading does not change significantly during the PRN26 rising satellite is being tracked after the large airplane turn (top right). Bottom right panel shows the amplitude for PRN26.

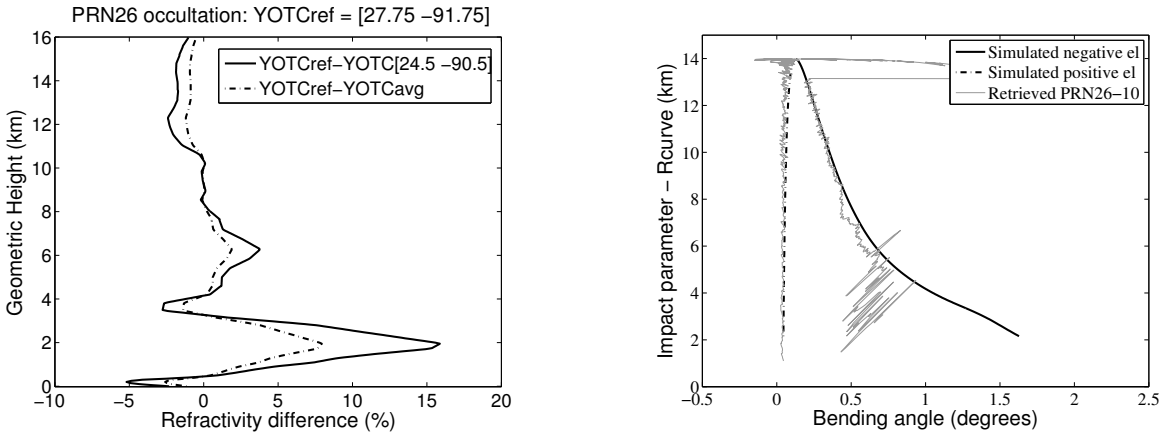

Figure A.20.: The reference refractivity profile for comparison with PRN26 occultation case is retrieved for 18Z and at a grid point [Lat Lon] = [27.75 -91.75] (Left). Observed (gray) bending angle for PRN26 and simulated bending from CIRA-Q model profile at Lat = 27.6.

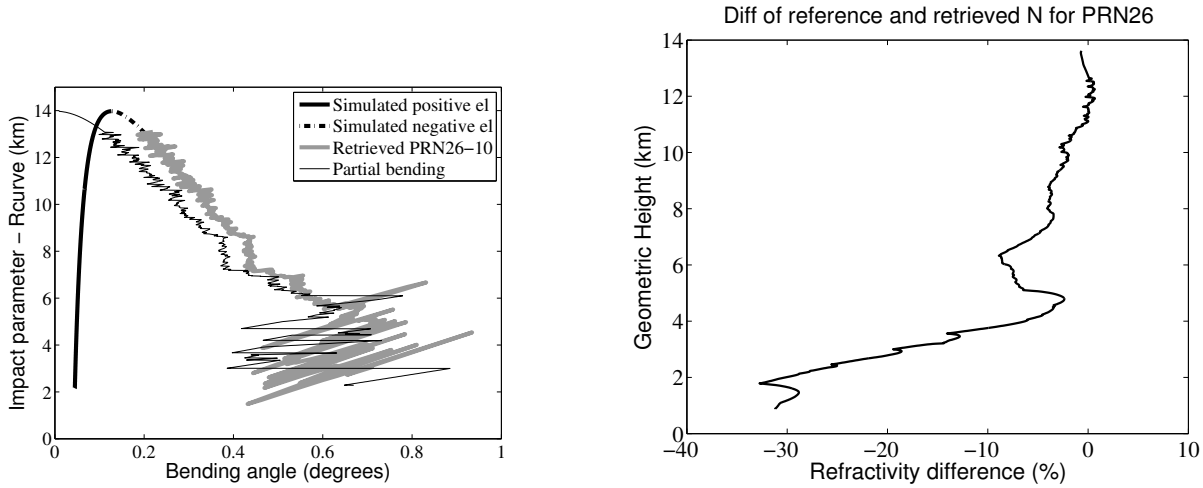

Figure A.21.: PRN26 observed bending is replaced with a simulated profile (solid and dashed black lines) for the positive elevation angle bending and the top 1 km of the negative elevation angle bending (gray line on left). Percent difference of retrieved and YOTC reference refractivity profiles.

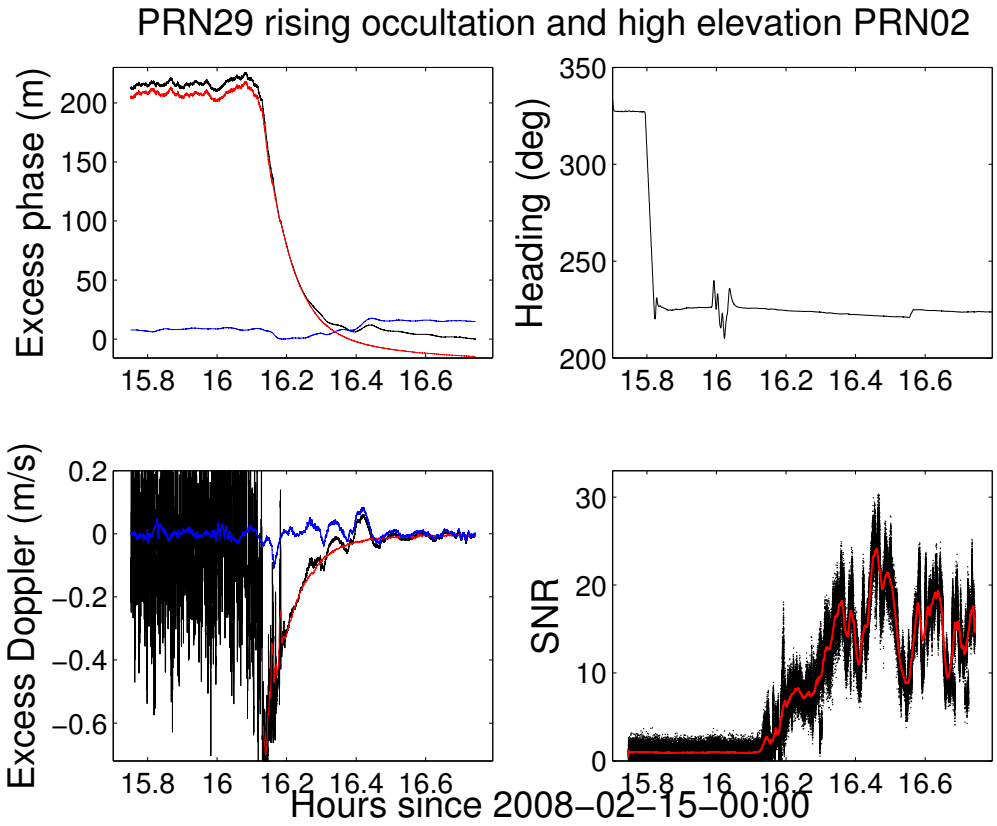

Figure A.22.: Excess phase (top left) and excess Doppler (bottom left) profiles for rising PRN29 and high elevation PRN02 satellites and their difference. Large variations in the airplane heading (top right) take place before the amplitude profile indicates the occultation period (bottom right).

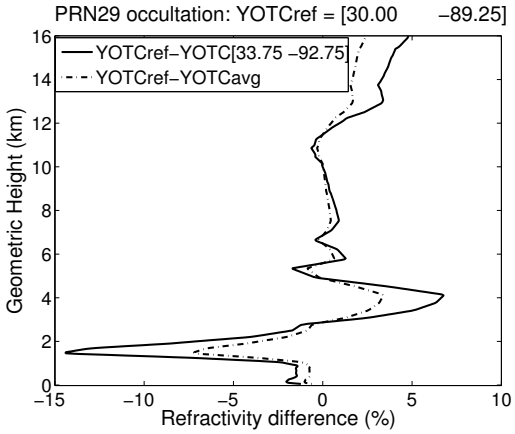

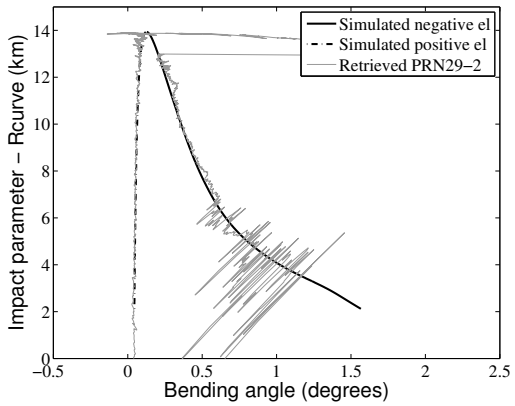

Figure A.23.: The reference refractivity profile for comparison with PRN29 occultation case is retrieved for 18Z and at a grid point [Lat Lon] = [30.00 -89.25] (Left). Observed (gray) bending angle for PRN29 and simulated bending from CIRA-Q model profile at Lat = 30.0.

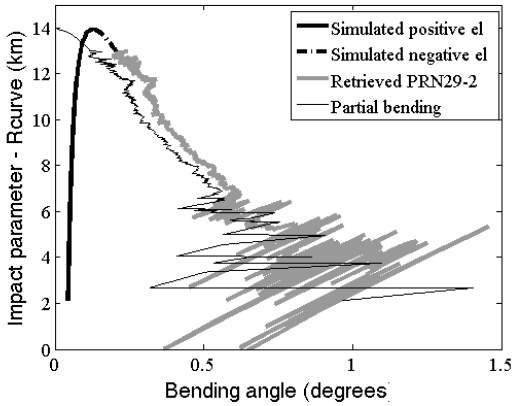

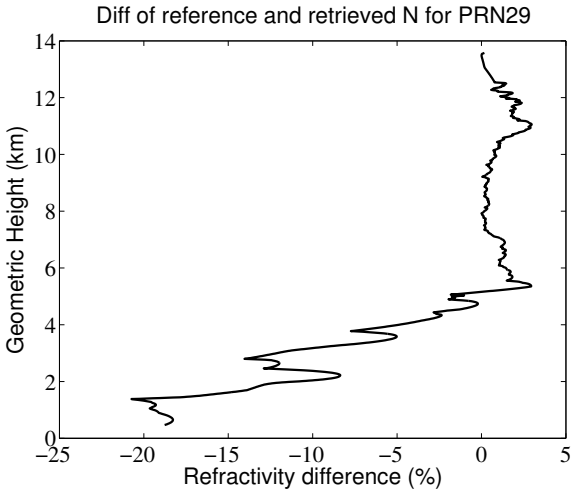

Figure A.24.: PRN29 observed bending is replaced with a simulated profile (solid and dashed black lines) for the positive elevation angle bending and the top 1 km of the negative elevation angle bending (gray line on left). Percent difference of retrieved and YOTC reference refractivity profiles.

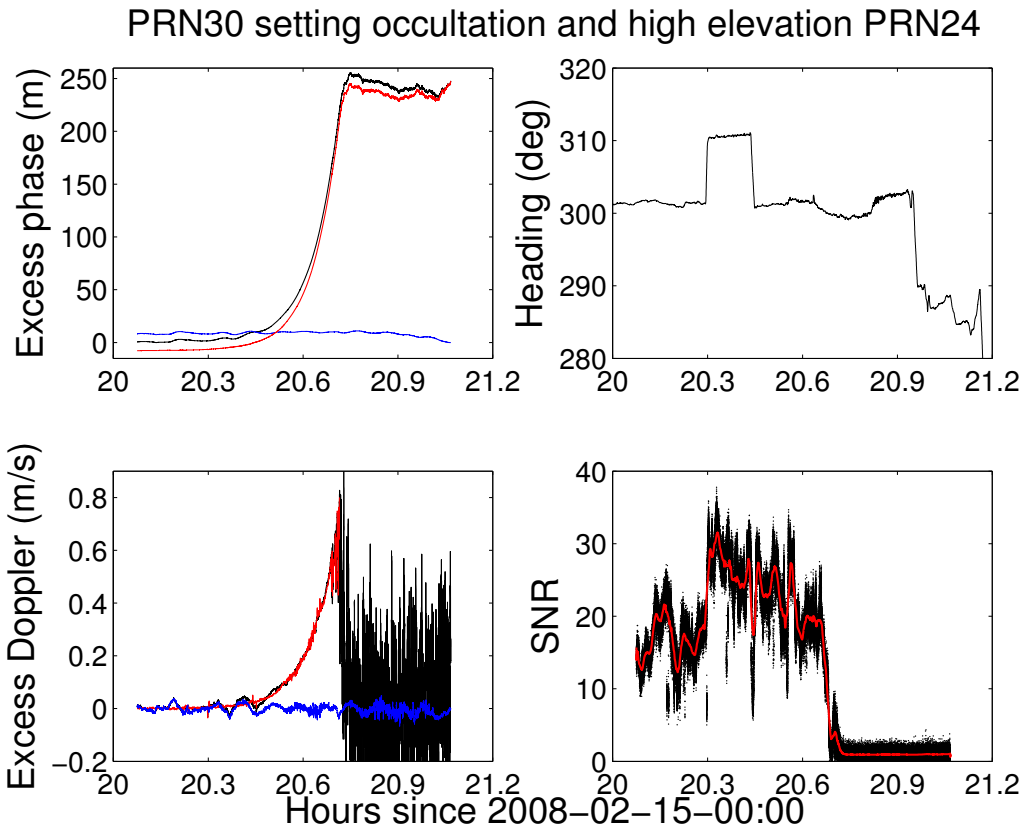

Figure A.25.: Excess phase (top left) and excess Doppler (bottom left) profiles for setting PRN30 and high elevation PRN24 satellites and their difference.

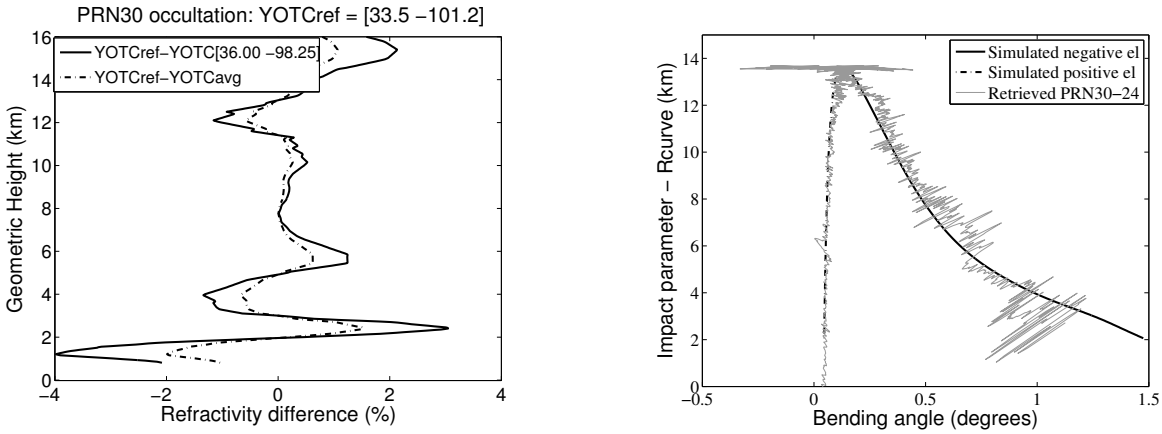

Figure A.26.: The reference refractivity profile for comparison with PRN30 occultation case is retrieved for 18Z and at a grid point [Lat Lon] = [33.5 -101.25] (Left). Observed (gray) bending angle for PRN30 and simulated bending from CIRA-Q model profile at Lat = 33.4.

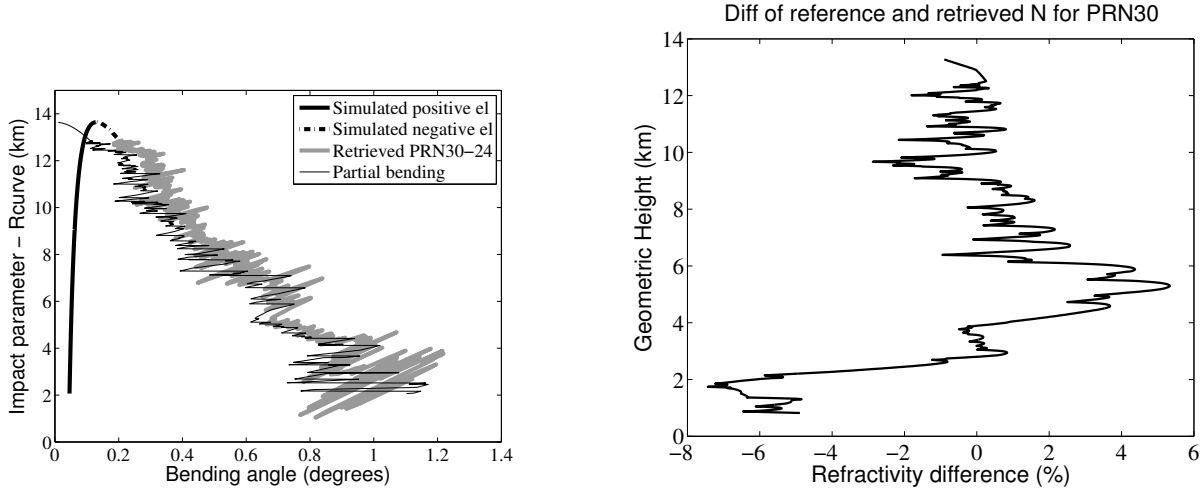

Figure A.27.: PRN30 observed bending is replaced with a simulated profile (solid and dashed black lines) for the positive elevation angle bending and the top 1 km of the negative elevation angle bending (gray line on left). Percent difference of retrieved and YOTC reference refractivity profiles.

Appendix B: Predicted occultations for February 15, 2008

Table B.1: HEFT08 day 046 predicted occultations.

Lon_st (deg)	Lat_st (deg)	Ht_st (m)	T_st (dec_hr)	PRN	Set (-1) Rise(1)	Star Port	Acq	Data Bit	Lon_end (deg)	Lat_end (deg)	T_end (dec_hr)
-90.03	30.03	-22.12	14.4	12	1	-	-	-	-90.02	30.03	14.7
-90.03	30.03	-22.41	14.4	20	-1	-	-	-	-90.03	30.03	14.9
-90.03	30.03	-22.45	14.9	10	1	-	-	-	-90.03	30.03	15.2
-90.03	30.03	-22.42	15.0	05	1	P	o	o	-90.03	30.03	15.3
-88.80	30.99	8549.40	15.4	28	-1	P	o	x	-88.80	30.99	15.7
-87.20	31.79	12260.28	15.6	09	-1	S	o	o	-87.20	31.79	16.2
-86.62	32.97	12522.64	15.8	30	1	S	o	o	-86.62	32.97	16.1
-87.51	32.25	13464.71	15.9	13	-1	P	o	o	-87.51	32.25	16.6
-89.01	30.50	13518.20	16.3	24	1	S	o	o	-89.01	30.50	16.6
-90.57	28.67	13575.77	16.6	17	-1	P	o	x	-90.57	28.67	17.0
-91.35	27.84	13595.03	16.8	29	1	S	o	o	-91.35	27.84	17.2
-93.52	25.42	13619.87	17.3	26	1	P	o	o	-93.52	25.42	17.5
-93.56	25.17	13629.94	17.3	15	1	P	o	o	-93.56	25.17	17.6
-92.78	25.10	13633.14	17.4	04	-1	P	o	o	-92.78	25.10	18.3
-86.91	25.64	13642.20	18.3	06	1	P	o	o	-86.92	25.64	18.6
-87.73	26.95	13611.54	18.5	21	1	P	o	o	-87.730	26.95	18.9
-87.99	27.37	13603.75	18.6	18	1	P	o	o	-87.99	27.37	19.0
-90.31	30.08	13527.65	19.1	12	-1	P	o	o	-90.31	30.08	19.4
-91.00	30.64	13510.73	19.2	05	-1	P	o	o	-91.01	30.64	19.6
-92.62	31.90	13466.46	19.5	02	-1	S	o	o	-92.62	31.90	19.8
-93.22	32.35	13444.37	19.6	30	-1	P	o	o	-93.22	32.35	20.0
-97.33	35.26	13327.60	20.3	16	-1	-	x	-	-97.33	35.26	21.4
-97.80	35.69	13312.83	20.3	22	1	P	o	o	-97.81	35.69	20.6
-98.84	36.45	13290.23	20.5	10	-1	S	o	o	-98.84	36.45	20.8
-102.47	38.41	10439.00	21.0	03	1	S	o	o	-102.47	38.41	21.3
-104.38	38.91	4357.78	21.2	09	1	P	o	x	-104.38	38.91	21.6
-105.12	39.91	1704.77	21.5	14	1	P	o	x	-105.12	39.91	21.8

Table B.2: Post-processing status of February 15 2008 GRS data in open-loop mode.

Time (dec hour)	PRN	Processing Status
14.41	12	Airplane on ground
14.46	20	Airplane on ground
14.94	10	Airplane on ground
15.06	05	Airplane take off
15.42	28	Airplane take off
15.59	09	Processed
15.79	30	PSRBitGen "One or more subframes did not parity"
15.98	13	Processed
16.31	24	Processed. However, the airplane turns during occultation
16.66	17	No COSMIC or GFZ data bits
16.82	29	Processed
17.28	26	Processed
17.32	15	Processed
17.41	04	PSRBitGen "One or more subframes did not parity"
18.36	06	PSRBitGen "One or more subframes did not parity"
18.57	21	Processed. However, the airplane turns during occultation
18.64	18	Processed. However, the airplane turns during occultation
19.14	12	Processed
19.26	05	Processed
19.53	02	PSRBitGen "One or more subframes did not parity"
19.63	30	Processed
20.29	16	Not acquired
20.37	22	Processed
20.54	10	GRS last file ends when PRN10 is at 0° (at 21:14)
21.03	03	Airplane landing
21.26	09	Airplane landing
21.58	14	Airplane landing

Appendix C: Simulation of realistic multipath for HIAPER aircraft

GPS carrier phase multipath is a major source of error in high precision differential positioning that can reach up to several centimeters [Braasch, 1999]. As any velocity errors in the GPS/INS navigation solution resulting from multipath will map onto the excess Doppler error, and the airborne RO retrieval is dependent on very accurate navigation solution for the aircraft, it is important to estimate the magnitude of multipath for general flight conditions, to see how big of an effect it will have on the retrieval accuracy. Also, it is possible that some occultations can be missed due to the interference from airplane structure during the transmission of the occulting signal. To evaluate the multipath errors introduced by the HIAPER aircraft's structure, we have simulated excess path length of possible reflections off the wing and tail for a simplified aircraft geometry. For the HEFT08 flight campaign, the RO antennas were located in the front windows of HIAPER aircraft. The approximated geometry for a signal reflected from the airplane wing is depicted in Figure C.1.

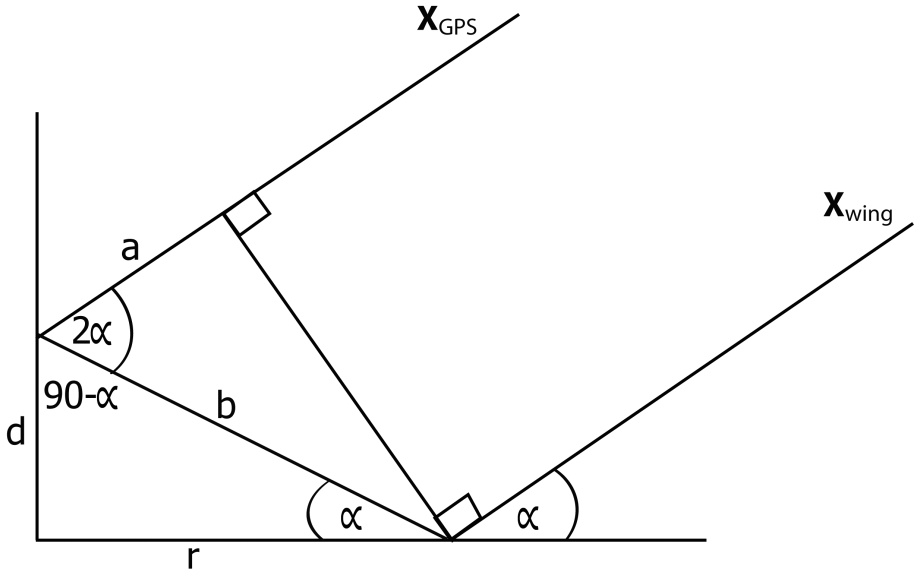

Figure C.1.: The multipath effect for the HIAPER airplane.

Here d is the height of the antenna above the wing's surface (Z direction), which is estimated to be 1.5 m. α is the angle the signal is incident on the reflecting point on the airplane's wing (X_{wing}), after which the signal travels an extra b path to the antenna at an α angle with respect to the wing. a is the distance by which the direct signal X_{GPS} range is larger than X_{wing}. r is the distance of the reflecting point on the wing's surface from the antenna in the Y direction. The length of the wing is approximated to be 20 m. For the simulation, all reflecting points on the wing from 0 to 20 m are considered in the Y direction. From Figure C.1 it is apparent that the extra path (D) the signal travels due to the multipath effect is:

$$D = b - a \tag{C.1}$$

Where a and b can be expressed in terms of the α angle:

$$a = bcos2\alpha \tag{C.2}$$

Thus, D can be written as:

$$D = \frac{d}{sin\alpha}(1 - cos2\alpha) \tag{C.3}$$

Using the known positions of antenna and the reflecting point, the α angle is calculated from the dot product between the unit vector in the y direction and the $\vec{X}_{wing}$ vector.

Similar calculations were carried out for signals reflected off the airplane tail, which can potentially be a high multipath environment. For this case, the tail of the airplane is approximated to be 18 m away from the RO antenna in the X direction, 4 m away in the y direction, and 4 m higher than the antenna (Z direction). The simulations of the multipath effect for HIAPER were performed for February 22 flight, for GPS satellites SV11, SV18, SV22, SV24, and SV29. The results for SV11 and SV18 are shown in Figures C.2 and C.3 respectively. The results demonstrate that for a signal reflected from the airplane's wing, the position errors can be up to 3 m, which increase in case of signals reflected off the airplane's tail reaching up to 8 m. In terms

of velocity error, the results yield an RMS time rate of change of up to 0.4 mm/s, and as it has been demonstrated by Muradyan et al. [2010] that velocity errors as big as 5 mm/s have very little effect on the refractivity retrievals. In the following pictures the results of the extra signal path due to multipath and the resulting velocities are shown for all considered satellites. The occasional spikes in the velocity plots are due to data gaps in the GPS antenna positions.

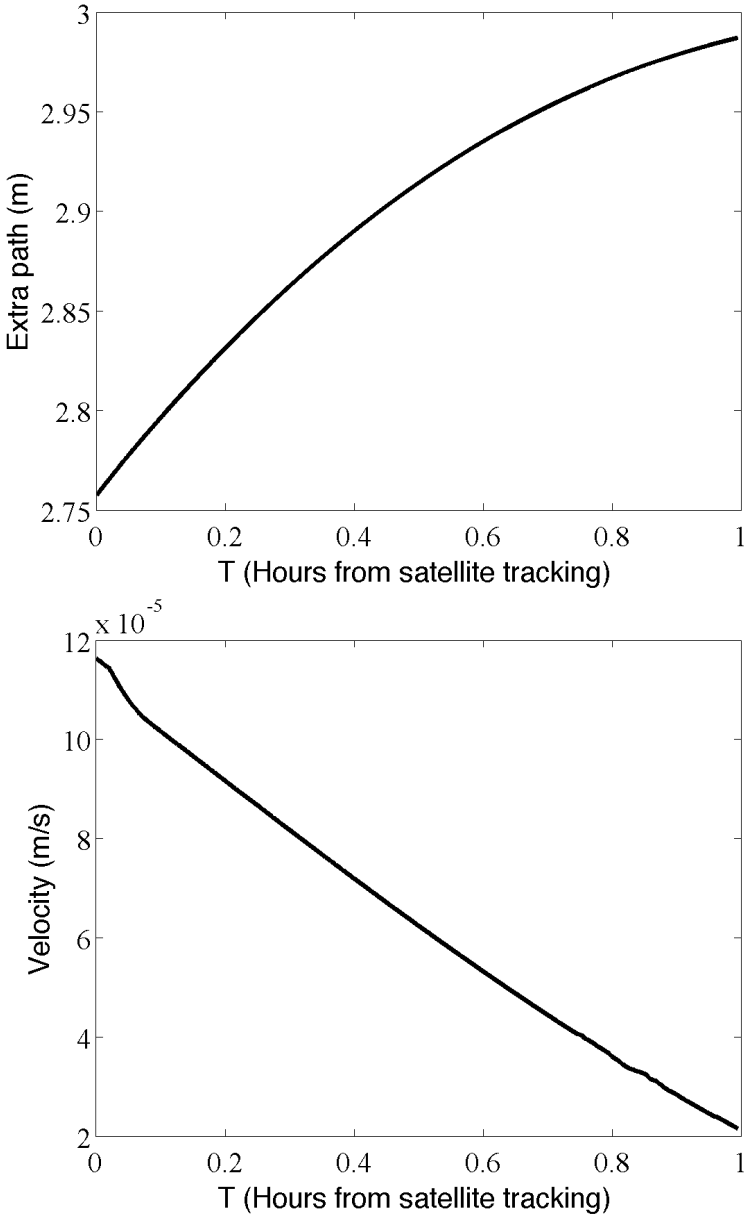

Figure C.2.: Extra path (left) and the resulting velocity (right) error for SV11 due to the multipath. The reflecting point is on the airplane's wing.

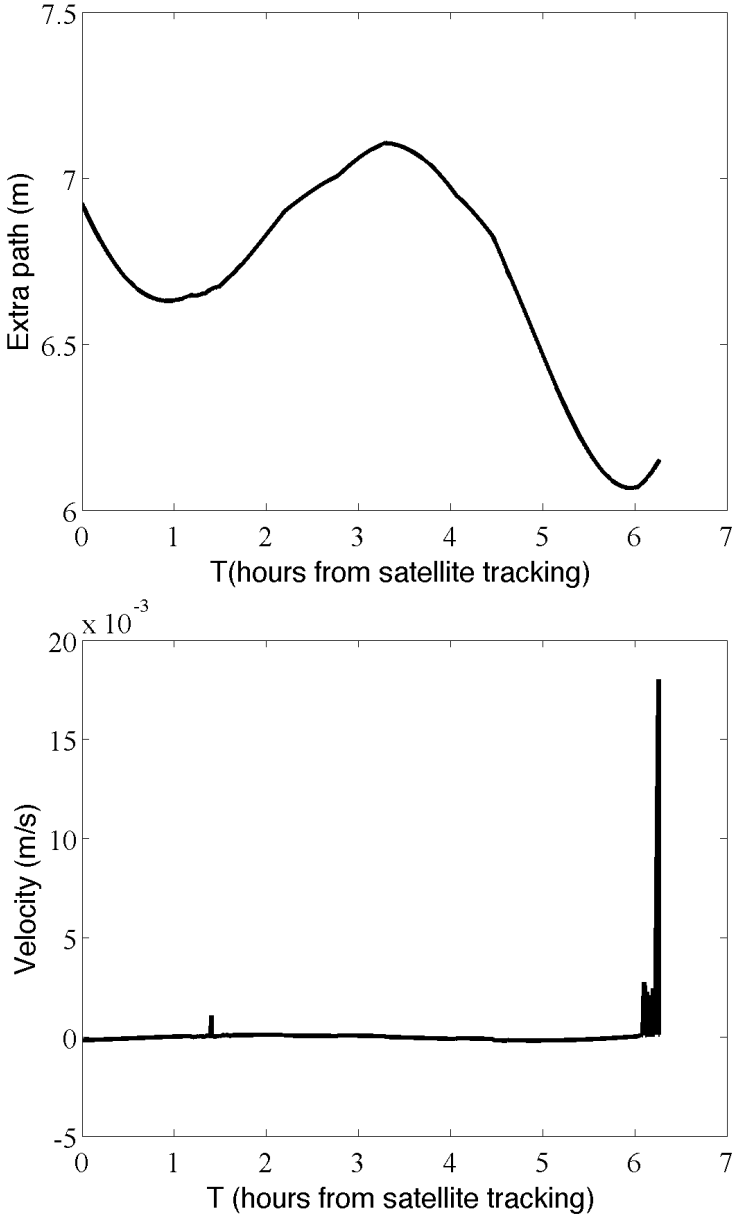

Figure C.3.: Extra path (left) and the resulting velocity (right) error for SV18 due to the multipath. The reflecting point is on the airplane's tail.

Appendix D: Full radio occultation data set depicting synoptic scale weather

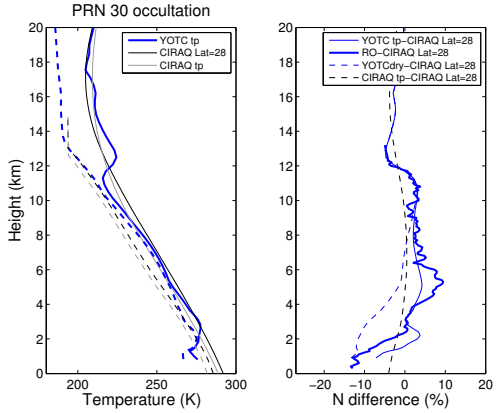

Figure D.1.: T and T_{dew} from ECMWF analysis reference profile for PRN30 occultation (left). The percent difference of retrieved (thick line) and ECMWF profiles (thin line) with respect to mean CIRA-Q climatology (right).

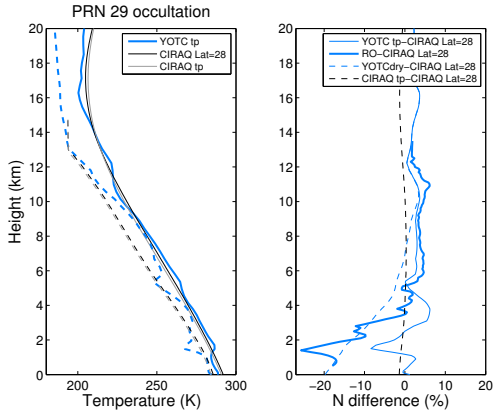

Figure D.2.: T and T_{dew} from ECMWF analysis reference profile for PRN29 occultation (left). The percent difference of retrieved (thick line) and ECMWF profiles (thin line) with respect to mean CIRA-Q climatology (right).

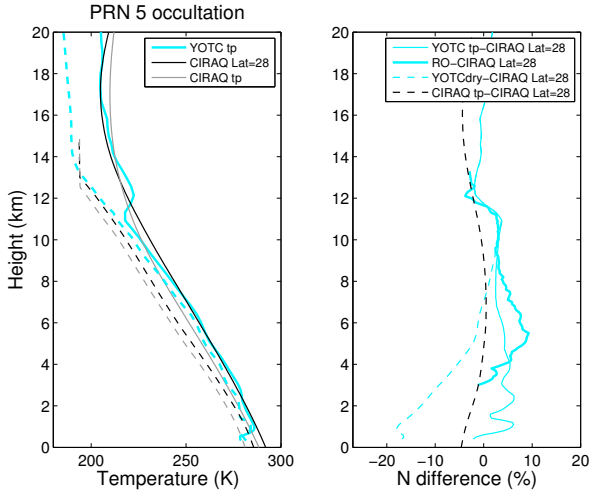

Figure D.3.: T and T_{dew} from ECMWF analysis reference profile for PRN05 occultation (left). The percent difference of retrieved (thick line) and ECMWF profiles (thin line) with respect to mean CIRA-Q climatology (right).

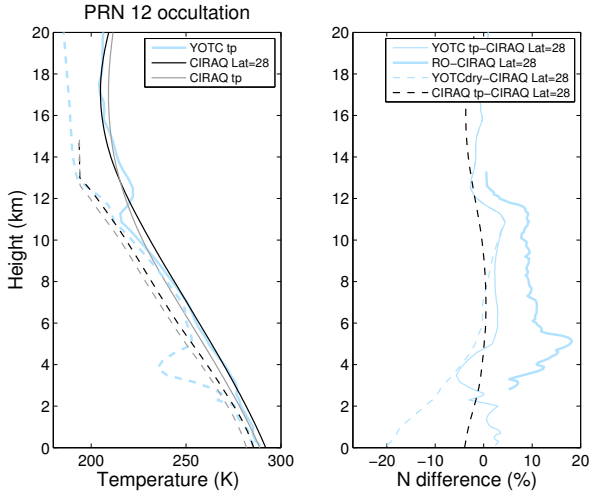

Figure D.4.: T and T_{dew} from ECMWF analysis reference profile for PRN12 occultation (left). The percent difference of retrieved (thick line) and ECMWF profiles (thin line) with respect to mean CIRA-Q climatology (right).

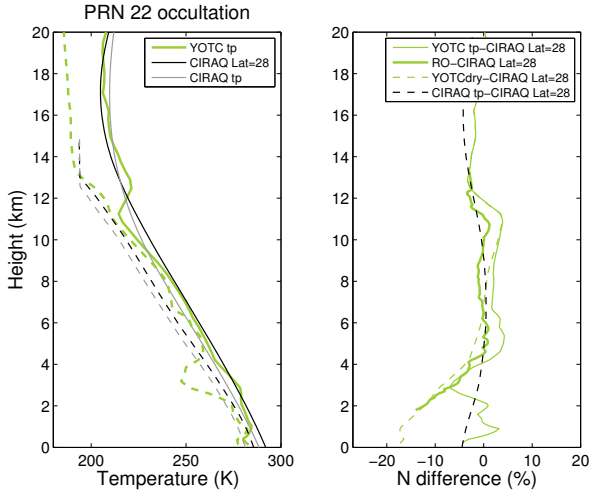

Figure D.5.: T and T_{dew} from ECMWF analysis reference profile for PRN30 occultation (left). The percent difference of retrieved (thick line) and ECMWF profiles (thin line) with respect to mean CIRA-Q climatology (right).

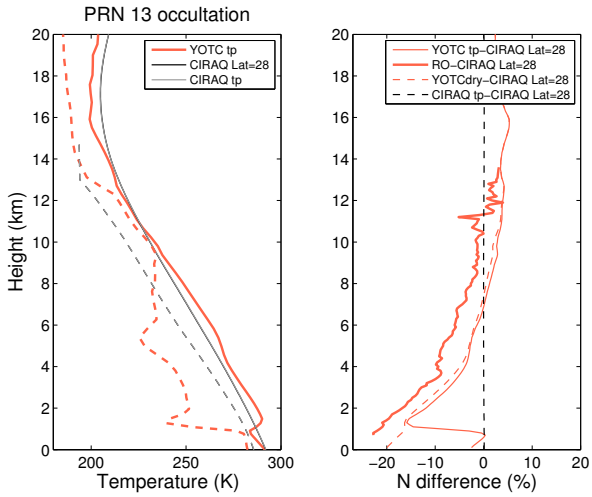

Figure D.6.: T and T_{dew} from ECMWF analysis reference profile for PRN30 occultation (left). The percent difference of retrieved (thick line) and ECMWF profiles (thin line) with respect to mean CIRA-Q climatology (right).

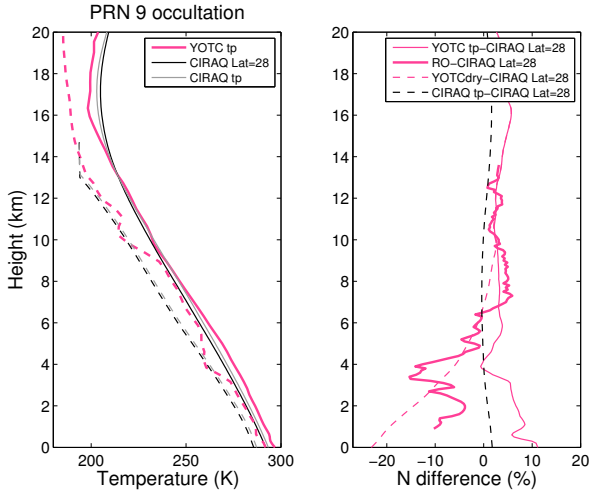

Figure D.7.: T and T_{dew} from ECMWF analysis reference profile for PRN09 occultation (left). The percent difference of retrieved (thick line) and ECMWF profiles (thin line) with respect to mean CIRA-Q climatology (right).

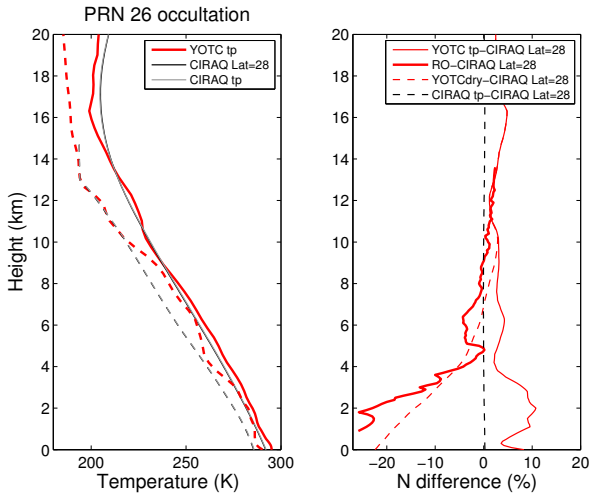

Figure D.8.: T and T_{dew} from ECMWF analysis reference profile for PRN26 occultation (left). The percent difference of retrieved (thick line) and ECMWF profiles (thin line) with respect to mean CIRA-Q climatology (right).

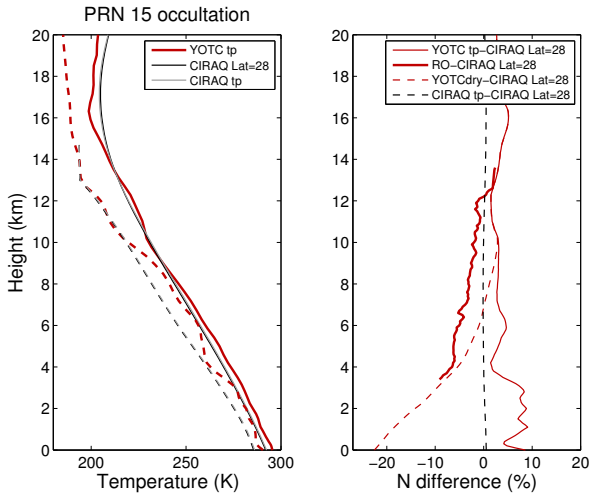

Figure D.9.: T and T_{dew} from ECMWF analysis reference profile for PRN15 occultation (left). The percent difference of retrieved (thick line) and ECMWF profiles (thin line) with respect to mean CIRA-Q climatology (right).

VITA

VITA

Paytsar Muradyan was born in Yerevan, Armenia on November 10, 1980. She completed her high school education at No. 1 school in Nor Kharberd in 1997. She attended the Yerevan State University between Fall of 1998 and Summer 2002 where she earned her B.S. in Physics.

She started her collaboration with Prof. Jennifer Haase at the Department of Earth & Atmospheric sciences at Purdue University as a visiting scholar in Spring 2006, joining the graduate program of the same department in Summer 2007. She first received her Masters degree in Spring 2009, and continued her education towards a Ph. D. degree receiving it in Summer 2012. Throughout her study at Purdue university, she was funded by the Schulmberger Foundation through the Faculty For the Future fellowship renewed based on annual competition.